

VI. Particle generations and masses on $\mathbb{C}^{\wedge 18}$, and VII. Curved space-times from $\mathbb{C}^{\wedge 18}$

Robert N. C. Pfeifer*

VI. Dunedin, Otago, New Zealand

VII. School of Mathematics and Physics, The University of Queensland, St. Lucia, QLD 4072, Australia and

VII. Perimeter Institute for Theoretical Physics, 31 Caroline St. N, Waterloo, ON, Canada

(Dated: January 4, 2022)

VI. The $\mathbb{C}^{\wedge 18}$ analogue model contains counterparts to the full particle spectrum and interactions of the Standard Model, but has only three tunable parameters. As the structure of this model is highly constrained, predictive relationships between its counterparts to the constants of the Standard Model may be obtained. In this paper, the model values for the masses of the tau, the W and Z bosons, and a Higgs-like scalar boson are calculated as functions of α , m_e , and m_μ , with no free fitting parameters. They are shown to be $1776.8715(2)$ MeV/ c^2 , $80.3784(24)$ GeV/ c^2 , $91.1875(37)$ GeV/ c^2 , and $125.2498(51)$ GeV/ c^2 respectively. All are within 0.1σ or better of the corresponding observed values of $1776.86(12)$ MeV/ c^2 , $80.379(12)$ GeV/ c^2 , $91.1876(21)$ GeV/ c^2 , and $125.25(17)$ GeV/ c^2 respectively. These results are suggestive of the existence of a unifying relationship between lepton generations and the electroweak mass scale, which is proposed to arise from preon interactions mediated by the strong nuclear force.

VII. The $\mathbb{C}^{\wedge 18}$ analogue model is a classical model of free fields on a manifold with anti-commuting co-ordinates which emulates the quantum field theory of the Standard Model. In some ways this emulation is remarkably accurate, predicting masses for the weak bosons and the tau which are in precise agreement with observation. However, the model also predicts a right-handed weak interaction which has not been observed. In this paper the final ungauged freedom of the $\mathbb{C}^{\wedge 18}$ analogue model is used to eliminate the right-handed weak interaction, while simultaneously introducing space-time curvature, and a gravitational interaction which emulates general relativity in experimentally observed regimes. The model is predictive of the value of Newton's constant, yielding $G_N = 6.67427(240) \times 10^{-11}$ m³kg⁻¹s⁻². Although the error bars on this calculated value are quite large, the central value is in agreement with the observed value of $G_N = 6.67430(15) \times 10^{-11}$ m³kg⁻¹s⁻² to a precision of better than $0.18\sigma_{\text{exp}}$.

CONTENTS

I. Introduction to Part VI	93	D. Gluon masses	110
II. Conventions	93	E. Scalar boson mass	111
III. The pseudovacuum	94	1. Boson loops	112
IV. Boson Mass Interactions	95	2. Background photon and scalar interactions	113
A. W mass	95	F. Neutral boson gravitation	114
1. Boson loops—overview	95	V. Lepton Mass Interaction	114
2. Gluon loops	98	A. Leading order	114
3. Photon, W , and Z boson loops	100	1. Action on colour sector	115
4. Scalar boson loops	102	2. Mass from photon and gluon components of the pseudovacuum	117
5. Net effect of all boson loops	104	3. Mass from scalar component of the pseudovacuum	118
6. Background photon and scalar interactions	105	4. Gluon and scalar field mass deficits	119
7. Universality of loop corrections	106	B. Foreground loop corrections	120
B. Z mass	107	1. 1-loop EM corrections	120
1. Boson loops	107	2. $O(N_0^{-1})$ corrections to 1-loop EM corrections	121
2. Background photon and scalar interactions	109	3. 1-loop gluon corrections	122
C. Weak mixing angle	110	4. 1-loop weak force corrections	123
		5. 1-loop scalar corrections	125
		6. 2-loop EM corrections	125
		C. Corrections to the lepton mass angle	125
		1. Origin of corrections	125
		2. Preamble	126

* rncpfeifer@gmail.com

3. First-order correction to K_ℓ^4 from the tau channel	126
4. Second-order correction to K_ℓ^4 from the tau channel	128
5. Reparameterisation of θ_e	129
6. Corrections to $[K_e(\theta_e)]^4$ from the muon channel	130
7. Local scaling symmetry	131
8. Corrections to $[K_e(\theta_e)]^4$ from the electron channel	132
VI. Predictions of the $\mathbb{C}^{\wedge 18}$ analogue model	132
A. Mass relationships	132
B. Results	134
C. Sources of numerical error	134
VII. Conclusion to Part VI	134
VIII. Introduction to Part VII	135
IX. Conventions	137
A. Notation and terminology	137
B. Quantum/classical correspondence	137
X. $\mathbb{C}^{\wedge 18}$ with curved space-time	138
A. Curvature and choice of gauge	138
B. Beyond-Standard-Model processes in the photon pair field	138
1. Origin of the photon pair field	138
2. Interactions of the photon pair field	139
3. Principle of equivalence	142
C. Evaluation of space-time curvature	143
1. Leading-order photon pair decay profile	143
2. Higher-order corrections	147
3. Elimination of GG^\dagger pairs	148
4. Rotating source	149
D. Beyond the dominant process	149
1. Other spin-2 processes	149
2. The right weak interaction and other spin-1 effects	149
XI. Results	149
A. Value of Newton's constant	149
B. Qualitative implications	150
XII. Conclusion to Part VII	151
Acknowledgments	151
A. Mass-related loop coefficients	151
B. Symmetry factors and photon loops	152
C. Solving the particle mass relationships	153
D. Evaluation of accessory results	155
References	156

I. INTRODUCTION TO PART VI

Introduced in Refs. [1–5], the $\mathbb{C}^{\wedge 18}$ model is a classical analogue model [6–8] which comprises free scalar fields (Fundamental Scalar Fields, FSFs) on a manifold with 18 anticommuting complex co-ordinates denoted $\mathbb{C}^{\wedge 18}$. When the FSFs are in a highly disordered and hence (from a coarse-grained perspective) a highly homogeneous state, the product of these fields on a $\mathbb{R}^{1,3}$ submanifold admits a description as a pseudovacuum state on which exist soliton waves. These soliton waves, in turn, behave as interacting quasiparticles governed by the low-energy regime of a quantum field theory with a gaugeable local symmetry. The emergent quasiparticles behave as coloured fermionic preons, and they in turn condense into fermions, quarks, and a scalar boson, with choices of gauge yielding a particle spectrum closely resembling that of the Standard Model, supplemented only by

- a ninth gluon, with mass on the electroweak scale, weakly interacting, and with action diagonal in colour,
- higher generations of electroweak bosons, with the lightest being W_2 at 17 TeV, and
- two low-mass WIMPs denoted G and G^\dagger which may be eliminated as described in Ref. [9].

Anticipating the weakness of the residual effects demonstrated in Ref. [9], the species $G^{(\dagger)}$ may be ignored in the current paper without introducing significant error.

Previous papers [4, 5] have introduced the boson and lepton mass interactions of the $\mathbb{C}^{\wedge 18}$ model at tree level, in which the emergent composite bosons and leptons acquire mass through coupling to the high-entropy pseudovacuum. At tree level, the mass ratios m_W/m_Z and m_W/m_H of the electroweak bosons have been shown to be in rough qualitative agreement with the Standard Model. A similar calculation at tree level for leptons is not possible due to vanishing of the tree-level electron mass, but order-of-magnitude estimates for higher-order corrections suggest that the electron gains mass once the 1-loop electroweak corrections are taken into account, and that the model is then not conspicuously inconsistent with the observed mass ratios m_μ/m_e and m_τ/m_e . In the present paper the boson and lepton mass calculations are performed to higher order, and relationships between the sectors are identified which permit the three input parameters of $\mathbb{C}^{\wedge 18}$ to be taken as α , m_e , and m_μ . The calculated values of m_W , m_Z , m_H , and m_τ are then seen to be in exceptional agreement with observation.

II. CONVENTIONS

This paper follows the same conventions as Refs. [1–5], henceforth Papers I–V respectively. Units are chosen

such that $c = 1$, $\hbar = 2$. When equations and lemmas from Papers I-V are referenced, they take the forms (I:1), (II:1), (II:A1), etc.

When referring to uncertainty in results, experimental uncertainties will be denoted σ_{exp} , and uncertainties in the theoretical calculation will be denoted σ_{th} .

In this paper, it is generally assumed that any particle under study is at rest or near-rest with respect to the isotropy frame of the pseudovacuum.

Regarding terminology around Feynman diagrams and symmetry factors:

- Where there exist multiple ways to connect up sources, vertices, and sinks to obtain equivalent diagrams up to interchange of non-distinguishable co-ordinates, the same term is obtained from the generator \mathcal{Z} in multiple different ways and thus the diagram acquires a multiplicative factor. This is referred to in the present paper series as a *symmetry factor*.
- Where integration over the parameters of a diagram (for example, over source/sink co-ordinates) yields the same diagram multiple times up to interchange of labels on these parameters, this represents a double- (or multiple-) counting of physical processes. It is then necessary to eliminate this multiple-counting by dividing by the appropriate symmetry factor. This is referred to in the present paper series as *diagrammatic redundancy* or *double- (multiple-) counting*.

III. THE PSEUDOVACUUM

The FSFs are defined on manifold $\mathbb{C}^{\wedge 18}$ and denoted φ_q . Defining a submanifold $M \subset \mathbb{C}^{\wedge 18}$ such that $M \cong \mathbb{R}^{1,3}$, the mapping of the FSFs to $\mathbb{R}^{1,3}$ is denoted $\varphi_q(x)$. Since $\mathbb{R}^{1,3}$ (but not M) may support fields of arbitrary power in x , the product field $\varphi(x)$ is defined on $\mathbb{R}^{1,3}$ as

$$\varphi(x) := \prod_q \varphi_q(x). \quad (\text{I:133})$$

The observed quasiparticles are then constructed from the gradients of the product field with respect to translations of the $\mathbb{R}^{1,3}$ submanifold within $\mathbb{C}^{\wedge 18}$. The pseudovacuum is characterised by an energy scale \mathcal{E}_0 , a mean expectation value

$$f^{-1} := \langle \varphi \rangle, \quad (1)$$

and a particle number N_0 being the number of FSFs having a point of inflection within a hypervolume

$$\mathcal{L}_0^4 := \mathcal{E}_0^{-4}. \quad (2)$$

Each FSF has at most one point of inflection. Introducing an energy per FSF,

$$\omega_0 := \frac{\mathcal{E}_0}{N_0}, \quad (3)$$

the macroscopic properties of the pseudovacuum may be parameterised in terms of (f, N_0, ω_0) of which f and N_0 are unitless.

On $\mathbb{R}^{1,3}$, the pseudovacuum may conveniently be described in terms of its non-vanishing expectation values. In the notation of Refs. [1–5] the non-vanishing bosonic components are

$$\langle [A^\mu(x) A_\mu(y)]_{\text{bg}} \rangle = -\mathbf{f}(x-y) \mathcal{E}_0^2 \quad (4)$$

$$\langle [c^{\tilde{\mu}}(x) c_\mu^{\tilde{d}}(y)]_{\text{bg}} \rangle = -\mathbf{f}(x-y) \mathcal{E}_0^2 \quad (5)$$

where $\mathbf{f}(x)$ is a Gaussian satisfying

$$\int d^4x \mathcal{E}_0^4 \mathbf{f}(x-y) = 1 \quad \forall \quad y. \quad (\text{I:168})$$

As noted in Sec. III C 7 of Paper III, the $\text{SU}(3) \otimes \text{GL}(1, \mathbb{R})$ invariance of the C sector implies that the background fields in Eq. (5) need not form a conjugate pair to have nonvanishing pseudovacuum expectation values.

The leptons are made up of three differently-coloured preons, generically

$$\begin{aligned} \Psi^{a\alpha}(x) &\propto (\varepsilon^{\alpha\beta} \varepsilon^{\gamma\delta} - \varepsilon^{\alpha\gamma} \varepsilon^{\beta\delta} + \varepsilon^{\alpha\delta} \varepsilon^{\beta\gamma}) \\ &\times \mathcal{C}_{c_1 c_2 c_3}^g \psi_{\beta}^{ac_1}(x_1) \psi_{\gamma}^{ac_2}(x_2) \psi_{\delta}^{ac_3}(x_3) \end{aligned} \quad (6)$$

following Eq. (III:31). In this, g is the generation index, and the coefficients $\mathcal{C}_{c_1 c_2 c_3}^g$ are constrained by requiring that particle $\Psi^{a\alpha}$ be both colourless and an eigenstate of the mass-generating interaction with the pseudovacuum. The preon expectation values satisfy

$$\begin{aligned} &\langle [\bar{\psi}^{\dot{m}}(x) \bar{\psi}^{\dot{n}}(y) \psi^m(x) \psi(y)^n]_{\text{bg}} \rangle \\ &= \langle [\bar{\psi}^{\dot{m}}(x) \bar{\psi}^{\dot{n}}(x) \psi^m(y) \psi(y)^n]_{\text{bg}} \rangle \\ &= \frac{1}{2f^2} \delta_{\dot{m}\dot{n}} \delta_{nm} \mathbf{f}(x-y) \mathcal{E}_0^2 \end{aligned} \quad (7)$$

where m (or \dot{m}) and n (or \dot{n}) range from 1 to 9 and enumerate pairs of index values a (or \dot{a}) $\in \{1, 2, 3\}$, c (or \dot{c}) $\in \{r, g, b\}$. The scalar boson is a sum over nine terms,

$$\mathbf{H} := f \psi^m \psi_m, \quad (8)$$

and thus satisfies

$$\langle [\mathbf{H}(x) \mathbf{H}^*(y)]_{\text{bg}} \rangle = \frac{9}{2} \mathbf{f}(x-y) \mathcal{E}_0^2. \quad (9)$$

The field A_μ corresponds to the photon, and $c_\mu^{\tilde{c}}$ corresponds to gluons associated with the Gell-Mann basis of $\text{SU}(3)_C$ plus an additional diagonal species, as enumerated in Eqs. (II:38–39). The construction of the pseudovacuum introduces a preferred rest frame, but this is essentially undetectable at energy scales small compared with

$$\mathcal{E}_\Omega := \mathbf{n} N_0 (N_0 - \frac{1}{2}) \omega_0 \quad | \quad \mathbf{n} = 9, \quad (\text{V:23})$$

which is seen to be approximately 6.2 TeV (153). To leading order the value of N_0 is

$$N_0 = \sqrt{\frac{m_W}{3\sqrt{2}m_e}} [1 + \mathcal{O}(N_0^{-1}) + \mathcal{O}(\alpha)] \quad (\text{V:15})$$

$$\approx 193.$$

IV. BOSON MASS INTERACTIONS

A. W mass

In Sec. III 1 of Paper V, a first-order expression for the W boson mass was obtained in terms of the free parameters of the $\mathcal{C}^{\wedge 18}$ model, f , N_0 , and ω_0 :

$$m_W^2 = 9f^2 k_1^4 \omega_0^2 N_0^{12} [1 + \mathcal{O}(N_0^{-1})] \quad (\text{V:13})$$

$$= 18m_e^2 N_0^4 [1 + \mathcal{O}(N_0^{-1})].$$

To obtain the high-precision numerical results presented in the present paper, it is necessary to evaluate some higher-order corrections to this expression.

1. Boson loops—overview

The leading contribution to the mass of the W boson arises from interactions between the W boson and the fermion components of the pseudovacuum. This interaction is corrected by numerous boson loops, with the candidate structures being illustrated in Fig. 1. Many of these diagrams may rapidly be dismissed. To contribute a loop correction to Fig. 1(i), a diagram must contain a loop which may be contracted down onto one of the vertices of Fig. 1(i). Diagram (ii) meets this criterion, but diagram (iii) does not as the loop contracts down onto an arbitrary point on the preon line. Diagram (iii) is therefore a correction to the preon propagator, so is already accounted for in the mean-field expansion of the pseudovacuum in diagram (i). Diagram (iv) also looks like it could contain a loop which could contract onto the upper vertex, but is better understood as a diagram *involving* the mass vertex rather than a *correction to* the mass vertex. This distinction is discussed further in the context of diagram (vi).

Diagram (v) requires a little more attention as it contains a loop which can be contracted onto the upper or lower vertex. It is expanded in terms of preons in Fig. 2(i). Two of the preons connecting with the loop boson must be expanded about the pseudovacuum term, and where these are both on the same vertex as in, for example, Fig. 2(ii), the average over many such interactions reduces to constant factors. The foreground momenta coupling to the loop boson then constitute a tadpole diagram which vanishes. When the pseudovacuum terms are on different vertices as in Fig. 2(iii), recognise that the mean background field term is only the first in a perturbative series describing fluctuations in the

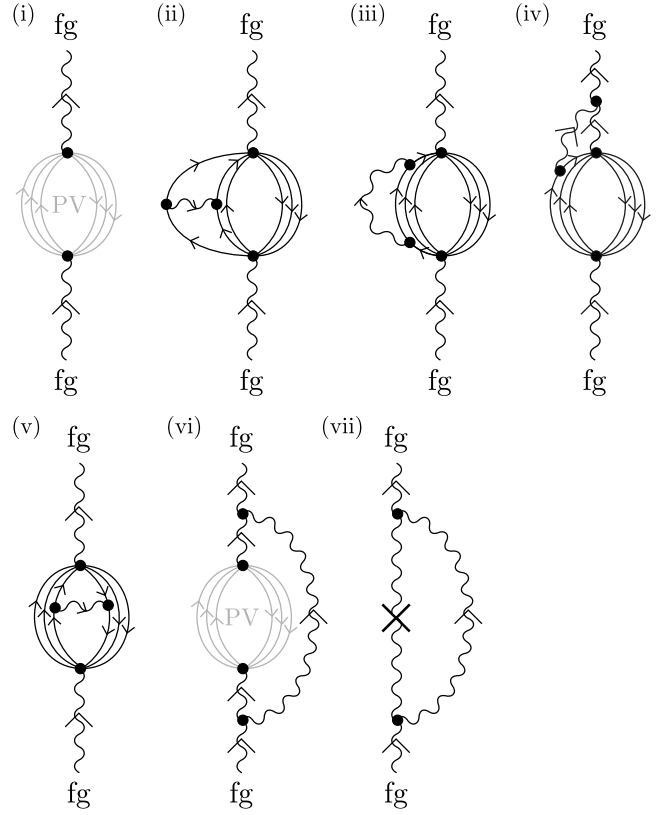


FIG. 1. (i) Leading-order contribution to the W boson mass. External legs are truncated. (ii)-(v) Candidate structures for vector boson loop corrections to diagram (i). Note that loop diagrams may (ii)-(v) modify the W boson mass-squared interaction, or (vii) merely involve it. They must continue to include six background preons, but on diagrams (ii)-(v) there are now more than six preon/antipreon lines so there are choices as to which are expanded using the mean background field approximation. These choices are not shown here, so it is not specified which preons are foreground and which are background in these diagrams. In diagrams (i) and (vi), PV indicates pseudovacuum. To consider in turn the structures shown: The loop in diagram (ii) may be contracted onto either the upper or lower vertex, and thus this constitutes a loop correction to diagram (i). The loop in diagram (iii) does not contract onto a vertex and thus constitutes part of the preon propagator. It does not contribute to loop corrections, and is already implicit in the mean-field substitution of diagram (i). Diagram (iv) looks like a correction to diagram (i) but is more properly understood as involving rather than contributing to the mass vertex. Diagram (v) looks like it could yield corrections to diagram (i) but on expanding in terms of preons as per Fig. 2(i) it may be shown to contain implicit preon tadpoles and therefore vanishes. Diagram (vi) involves but does not contribute to the vertex, and its Standard Model counterpart is shown in diagram (vii). All diagrams are discussed further in the text.

pseudovacuum. Some foreground momentum may therefore be transferred along pseudovacuum lines in the form of these fluctuations, but this transfer again constructs a tadpole so such contributions to foreground momen-

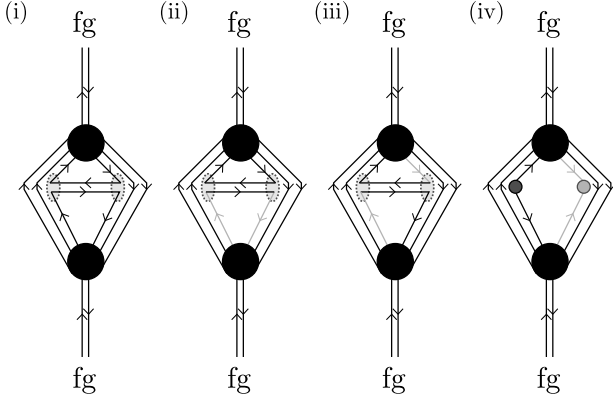


FIG. 2. (i) Preon expansion of Fig. 1(v). (ii) When both lower or both upper preon lines connecting to the loop boson are background, on averaging over many interactions the foreground field lines behave as a tadpole diagram. (iii) When one upper and one lower preon line are background, perturbations about the mean background value cannot transport foreground momentum as this would once again result in an upper or lower tadpole for the momentum transported. This implies that the momenta associated with the background preons at their vertices with the loop boson are not independent, permitting diagram (iii) to be redrawn as diagram (iv). The grey dots are orientation-reversing (and perhaps colour-changing) vertices. The colour transforms they perform are correlated, but they do not exchange momenta. They may be absorbed into the lower vertex, effectively reducing the number of background field lines by one.

tum transport necessarily vanish. The foreground and background momenta therefore propagate independently, equivalent to Fig. 2(iv). As the two vertices where the background field contacts the loop boson are not capable of independently borrowing or lending momentum to the foreground fields, the effective number of interface vertices between the foreground and background fields is reduced by two. This diagram therefore does not mediate a coupling between the W boson and the background fermion fields (which require six preon and six antipreon operators), and thus is not part of the mass series for W .

Finally, diagram (vi) again does not contribute as it requires non-truncated external legs. In fact, diagrams (iv) and (vi) are better understood as processes *involving* rather than *correcting* diagram (i). This is readily seen for diagram (vi) when the leading-order interaction of Fig. 1(i) is associated with a simple mass vertex $m_W^2 W^\dagger W$. In both the $\mathbb{C}^{\wedge 18}$ model and the Standard Model, expansion of the propagator yields higher-order corrections to the mass vertex as shown in diagram (vii). In the Standard Model a renormalisation scheme such as $\overline{\text{MS}}$ may be chosen to eliminate these terms, such that the coefficient on the simple mass vertex corresponds to the true mass of the W boson. This also holds for the $\mathbb{C}^{\wedge 18}$ model in the regime in which it is a good analogue to the QFT. The correction given in diagram (vi) is therefore a Proper Self Energy (PSE) term extraneous to the simple mass vertex in both the Standard Model and the $\mathbb{C}^{\wedge 18}$

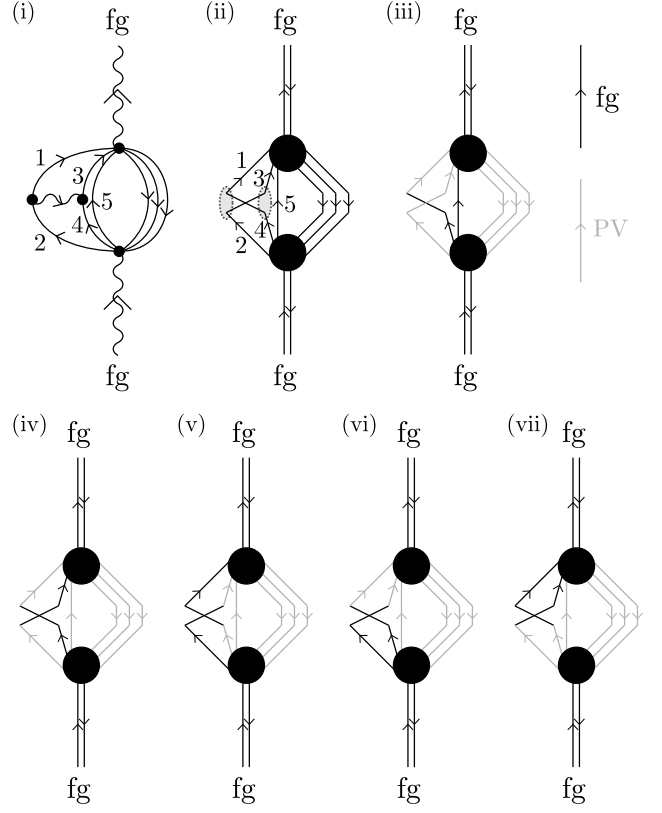


FIG. 3. (i) Taking the specific diagram shown in Fig. 1(ii), label the preon lines as shown. (ii) Preon form of diagram (i). (iii) Option 1 in Table I has an effective foreground connection between upper and lower vertices, discussed further in the text, and thus only five background preon lines. It is not a valid W boson mass term. Options 2, 4, 6, 7, and 8 may be discarded similarly. Options 3 and 10 are shown in diagrams (iv) and (v) and are seen to be equivalent up to two braids and a cycling in colour labels, so only one need be retained. The other valid diagrams are options 5 and 9, shown in diagrams (vi) and (vii) respectively. In diagrams (iii)-(vii), foreground preons are drawn in black and pseudovacuum preons in grey.

model. For diagram (iv) the situation is similar: For a gluon, the net colourlessness of the W boson causes this diagram to vanish, whereas for A -sector bosons, on summing over all possible locations for the lower vertex to couple to a preon or antipreon, conservation of charges and momenta ensures that equivalency is recovered to a situation where a loop boson couples two separate locations in the propagator of the W boson.

Having eliminated the other candidate diagrams, the only corrections remaining to be evaluated are those having the form of Fig. 1(ii). Since these diagrams constitute couplings to background fermions, they must contain couplings between the W boson, three background preon lines, and three background antipreon lines. Numbering the preon lines as per Fig. 3(i) there are ten candidate terms in the mean background field expansion, listed in Table I.

Examining option 1, in this diagram only one foreground preon (line 4) connects with the loop boson. The background fields proceeding from the loop boson to the upper vertex (lines 1 and 3) may transport foreground momentum as fluctuations around the background mean field state, but the parameter space of this connection corresponds to two preons, and is therefore over-large for transmitting the momentum of a single foreground preon. Performing a unitary mixing of these two background preons, there exists a (generally nonlocal) basis in which fluctuations about the background mean field value are transmitted along only one of the two upper left background preon lines. Also, fluctuations are on average not transmitted along the lower background field line (line 2) as this creates a tadpole as discussed for Fig. 2(ii). Consequently, as with Fig. 2(iii), the lower background preon (line 2) and the uninvolved degrees of freedom obtained from lines 1 and 3 may be mapped to a single, connected background field extending from the lower to the upper vertex as was done in Fig. 2(iv) (though this time no reversal of orientation is required). This diagram therefore also has the incorrect number of independent background preon operators to mediate an interaction between the W boson and background fermion fields. The same argument applies to options 2, 4, and 7, and a similar argument separating the foreground and background degrees of freedom applies to options 6 and 8.

Further, option 10 is equivalent to option 3 up to a cycling in colour labels. Other diagrams having the same structure as Fig. 1(ii) correspond to precisely these cyclings of the colour labels, and are included in a summation over diagrams below, so option 10 is redundant. Therefore only options 3, 5, and 9 remain. It is worth noting that interactions between preons within the loop boson of option 3 [Fig. 3(iv)] may also in theory cause construction of foreground momentum loops with both termini connected to the upper or lower vertex—however, these tadpoles vanish and thus the only admissible mix-

ing processes are those which preserve the diagrammatic form shown. These mixing processes may consequently be ignored.

Having identified the valid choices as to which preons participate in the mean background field expansion, now recognise that Fig. 1(ii) is one of six diagrams having equivalent structures. On the left of the figure there are three choices of pairs of preons which may be linked by a boson, and on the right side of the figure there are three choices of pairs of antipreons which may similarly be pairwise linked to yield equivalent factors. It suffices to evaluate one of these diagrams, and multiply by six.

In evaluating these corrections, note that the preons which are evaluated using the pseudovacuum mean field values no longer have all field operators on the same vertices. For these preons to remain correlated with their counterparts, such that the diagram's contribution to m_W^2 does not vanish, the pseudovacuum sources and sinks must continue to be within $O(\mathcal{L}_0)$ of one another, and the loop correction must not introduce any correlations with particles outside the local region (both spatial and temporal) within which the pseudovacuum is self-correlated. This region has dimensions of order \mathcal{L}_0 , and is termed the autocorrelation region, or local correlation region. This is similar to the treatment of the scalar boson mass diagram having four preon and two antipreon lines [Fig. 3(ii) in Paper V].

Further recognise that in Fig. 1(ii) the loop spans between two components of a composite fermion. These are necessarily separated, on average, by a distance of $O(\mathcal{L}_\psi)$ in the rest frame of the fermion, which is the maximum separation of the preon components of a fermion triplet. As this length scale is much smaller than \mathcal{L}_0 , which is the characteristic length scale of mass interactions, the loop boson may propagate on-shell across this distance as a massless particle. It may also engage in lengthier excursions characterised by scales such as $O(\mathcal{L}_0)$, on which it will acquire a nonzero mass, but over a net distance of $O(\mathcal{L}_\psi)$ from one preon to another, such excursions will inevitably be far off shell and may be disregarded. As noted in Sec. III 1 of Paper V, the underlying vertex diagram is restricted to a region characterised by \mathcal{L}_ψ and thus the added vertices on any loop corrections must also lie within such a region. By the same argument as for Fig. 1(ii), the particles participating in these loops are likewise massless. (This argument also applies to corrections arising from the complex scalar boson.)

Having thus established

- the diagrams which need to be evaluated to compute vector boson loop corrections to Fig. 1(i), and
- that all bosons in these loops are effectively massless over the length scales involved,

these loop corrections may be evaluated as follows.

TABLE I. List of labellings of preon lines in Fig. 3(i). Labellings which connect the upper and lower vertices with a foreground preon are described as “connected” and may be discounted.

Option	Background	Foreground	Status
1	1,2,3	4,5	Connected
2	1,2,4	3,5	Connected
3	1,2,5	3,4	Valid
4	1,3,4	2,5	Connected
5	1,3,5	2,4	Valid
6	1,4,5	2,3	Connected
7	2,3,4	1,5	Connected
8	2,3,5	1,4	Connected
9	2,4,5	1,3	Valid
10	3,4,5	1,2	Equivalent to option 3

2. Gluon loops

It is convenient to work in the e_{ij} basis of $\text{gl}(3, \mathbb{R})$, noting the caveat of Sec. III C 7 of Paper III regarding counting of FSF symmetry factors. As noted above, there are six topologically distinct diagrams having the general form of Fig. 1(ii) where a gluon propagates either from one preon to another, or from one antipreon to another. Each of these six diagrams admits multiple colour labellings. By $\text{SU}(3)_C$ symmetry, all six choices as to which preons engage in gluon exchange, and all valid choices of colour labels, make equal contributions to m_W^2 . Interaction with the pseudovacuum is with randomly chosen background fermion fields compatible with a given diagram, granting colour neutrality to the preon triplet and to the antipreon triplet, and the colour symmetry of the pseudovacuum implies a summing over possible colour configurations. Since the colours of the three members of the triplet are unique, the factor associated with this sum may be equivalently represented either by explicitly summing over all colour labellings, or by suppressing these labellings and instead counting the exchange symmetry of the preon lines. (This works even when the A -charges are not homogeneous, as a sum is then also made over the position of the mismatched A -charge.)

Given one specific choice of diagram with one specific colour labelling, the gluon vertices are each associated with a factor of f , and FSF symmetries yield a factor of $N_0^3 [1 + \frac{33}{8} N_0^{-1} + O(N_0^{-2})]$ with counting being the same as for the photon (III:82) (recalling that for the purpose of counting FSF symmetry factors, the W boson and gluons must be written in terms of their real hermitian components). Comparing with Eq. (III:83) the product of the gluon vertex factors is therefore equal to

$$2\alpha[1 + O(\alpha)]. \quad (10)$$

Further, taking an approach similar to Sec. III E 8 of Paper III, consider a specific one of the six topologically distinct diagrams [e.g. gluon links preon 1 to preon 2, as shown in Fig. 1(ii)] but let this diagram be averaged over all colour labellings. For conciseness, include FSF symmetry factors in the vertex coefficients ($f \rightarrow \tilde{f}_A$). Choosing one gluon vertex to nominally be the emission vertex, it attracts factors as follows:

- One (spatial) choice of which preon to interact with.
- Three choices of colour on that preon prior to interaction.
- Interaction strength \tilde{f}_A .

Similarly, for the nominal absorption vertex:

- One (spatial) choice of which preon to interact with.
- Two choices of colour on that preon prior to interaction (which must differ to the preon at the emission vertex prior to interaction).

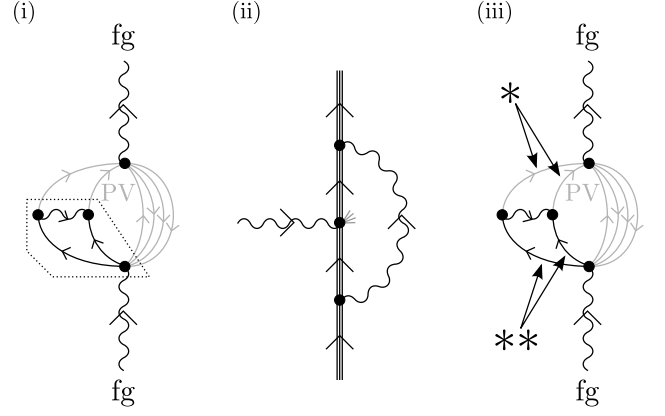


FIG. 4. Applying diagrammatic isotopy permits (i) gluon exchange to be rewritten as (ii) a gluon-mediated loop correction to W boson emission via either of the processes illustrated in Fig. 5. [The other four preons at the vertex are uninvolved, and are shown as truncated stubs in diagram (ii).] This gives numerical equivalence between the vertex loop correction of diagram (ii) and the correction generated by the indicated region of diagram (i), up to a sign due to the crossing in Figs. 5(ii) and (vi) and a factor of 2 for the symmetry which interchanges the two different ways this reduction can be achieved. This symmetry is illustrated in diagram (iii), where simultaneous exchange of the two preon lines marked $*$ and the two preon lines marked $**$ leaves the figure unchanged up to a permutation of colour indices, and interchanges Figs. 5(i) and (v).

- Interaction strength \tilde{f}_A .

For the gluon:

- There are nine different species of gluons.
- However, only one in three is compatible with the preon colour at the emission vertex.
- Similarly, only one in three of those remaining is compatible with the preon colour at the absorption vertex.

Finally, to go from a sum to an average over colour labellings on the preon lines, introduce a further factor of $\frac{1}{6}$. After evaluating all colour labellings in this way, the net product of vertex factors for a given position of the loop is $\tilde{f}_A^2 = 2\alpha[1 + O(\alpha)]$.

Next, recognise that each interaction between a preon and a gluon takes place in the presence of two other preons, with the three preons arising from a background fermion. This is a single-boson-species interaction so K matrices are not required (Sec. III C of Paper IV). For purposes of evaluation it is useful next to consider the choice of diagram and pseudovacuum expansion shown in Fig. 4(i) and map the indicated subdiagram into a loop diagram involving fermions. To do so, recognise that a subset of the preon lines in Fig. 3(i)-(ii) may be identified with a boson loop correction to $W^{(\dagger)}$ emission, up to an additional crossing. A suitable subset is shown

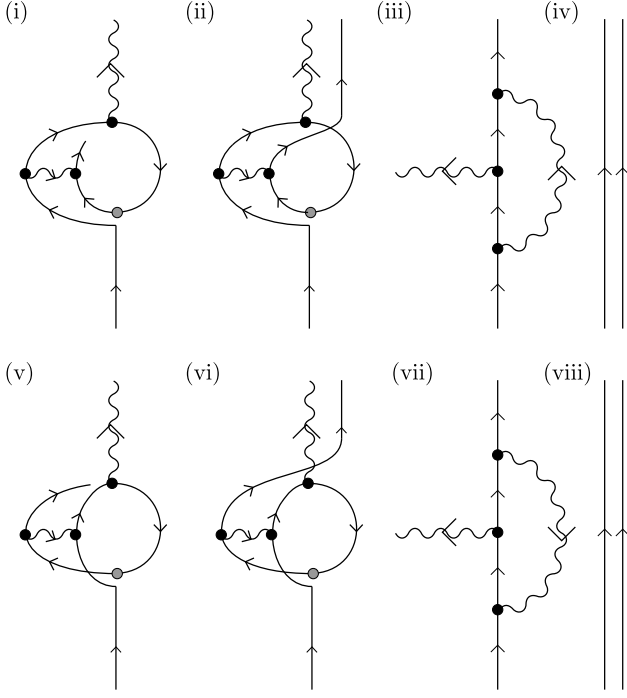


FIG. 5. (i) A subset of the preon lines in Fig. 3(i)-(ii), chosen for consistency of colour, construct an off-diagonal boson loop correction to W boson emission at the upper vertex. The grey dot denotes a change in A -sector charge with no consequence for the colour interaction. If the free preon is taken to the far field as shown in diagram (ii), this is then equivalent to the loop correction shown in diagram (iii) up to a crossing, which yields a factor of -1 . Adding further preons (iv) to diagram (iii) permits the emitting particle to be converted to a fermion. Internal symmetrisation within the fermion then allows the loop boson to couple to any member of the triplet at each vertex as discussed in Sec. VB, but the resulting factors of 3 cancel with factors of $1/\sqrt{3}$ in the definitions of the fermions in Sec. IIIB 1 of Paper III. An alternate and equivalent construction, which may also be obtained from Fig. 3(i)-(ii), is shown in diagrams (v)-(viii). Note that the other preons from Fig. 3(i)-(ii) may also optionally be reintroduced into diagrams (i)-(ii) or (v)-(vi), where they comprise one free preon with arrow oriented downwards, and either two more free preons (one up, one down) or a closed loop which is eliminated by vacuum normalisation. Their reintroduction introduces no further factors into the multiplicative constant associated with the loop correction.

in Fig. 5(i)-(ii), with an alternative choice being shown in Fig. 5(v)-(vi). An isotopy transformation on either set yields diagram (iii) up to a sign corresponding to the preon crossing. It is then convenient to introduce a further two preon lines which have the same A -charge as the interacting preon, and with colours chosen to yield overall colour neutrality. If these are balanced by a numerical factor of $\mathcal{N}^{-1} = (N_0 + 1)^{-2}$ then this leaves the value of the diagram unchanged. The resulting diagram has definite colour on each preon, and a specific pair of preons of definite colour engage in the gluon interaction. However, if the diagram is averaged over the locations of

the preons [10], and these are assumed subject to random redistribution as they propagate, for independence of arrangement at upper and lower vertices, then this gives three configurations at each loop vertex, each accompanied by a factor of $1/3$. This has no effect on the vertex factors (see Sec. IIIE 8 e of Paper III), but completes the mapping of the preon diagram in Fig. 4(i) to the fermion diagram of Fig. 4(ii). The loops in the two diagrams are numerically equivalent up to a factor of -1 for the crossing in Fig. 3(ii) or (vi), and a factor of 2 for the symmetry present in Fig. 4(i) [and made explicit in Fig. 4(iii)] which gives rise to the two choices of Figs. 3(i) and (v).

It is convenient to have a systematic means of presenting the factors associated with the many loop diagrams encountered in this paper. Therefore let the overall correction to the original vertex be written in terms of the following factors:

- A combined vertex and structural factor,
- A mass-related factor, and
- A common factor of $(4\pi)^{-1}$ written separately for clarity.

For reference, in this notation the factors associated with the one-photon-loop correction to lepton magnetic moment would be

$$2\alpha \cdot \mathbf{f}\left(\frac{m_\ell^2}{m_A^2}\right) \cdot \frac{1}{4\pi} \quad (11)$$

and those for the one- W -loop correction to lepton magnetic moment would be [11]

$$-\frac{10\alpha}{3} [1 + \mathcal{O}(\alpha)] \cdot \mathbf{f}\left(\frac{m_\ell^2}{m_W^2}\right) \cdot \frac{1}{4\pi}. \quad (12)$$

Where the loop boson is a foreground field, the mass dependency $\mathbf{f}(\cdot)$ evaluates as

$$\mathbf{f}\left(\frac{m_\ell^2}{m_b^2}\right) \longrightarrow \begin{cases} 1 & \text{if } m_b^2 = 0 \\ \frac{m_\ell^2}{4\pi m_b^2} & \text{if } m_b^2 \gg m_\ell^2. \end{cases} \quad (13)$$

(Note that this expression attracts a modification for background fields, discussed in Appendix A.)

From the above breakdown of factors associated with vector boson loop corrections to vector boson emission, it is readily seen that the off-diagonal gluon attracts a structure factor of $-10\alpha/3$, supplemented by a factor of 2 from the two ways which Fig. 4(i) may be mapped to Fig. 4(ii), and a factor of -1 for the crossing in Figs. 5(ii) and (vi) respectively. The mass factor vanishes because the gluon is massless over scale \mathcal{L}_ψ . Finally, multiplying by three for the three different pseudovacuum expansions and six for the six numerically equivalent diagrams yields

$$3 \cdot 6 \cdot \frac{20\alpha}{3} [1 + \mathcal{O}(\alpha)] \cdot 1 \cdot \frac{1}{4\pi} = \frac{60\alpha}{2\pi} [1 + \mathcal{O}(\alpha)]. \quad (14)$$

These loop corrections apply identically to the diagrams in which the W boson interacts with background lepton fields (“ W /lepton diagrams”) and the diagrams in which the W boson interacts with background quark fields (“ W /quark diagrams”) as the colour structure of both diagrams is the same, and the gluons are agnostic of A -charge.

3. Photon, W , and Z boson loops

Calculation of the contribution of gluon loops is relatively straightforward because the W boson is colour-agnostic, having trivial representation on the C sector. However, more caution is required on the A sector, as the W boson is not agnostic of A -charges.

For the photon, proceed as with the gluons by enumerating all the interactions at the preon level. Begin with the W /lepton diagrams. In contrast with the preceding calculation there are only three such interactions, as the photon may only couple to the charged preons in the e_L side of the loop. However, there are still three pseudovacuum expansions per diagram. Next, as per Sec. IIIE8 of Paper III, note that lepton couplings to photons arise in equal measure from all three preons. *Within a fermion*, the coupling of a single preon to a photon carries an effective coefficient of $\sqrt{\alpha}/3$ due to the normalisation factor in Eq. (III:28). This may be contrasted with gluon couplings which are always mediated by the single preon carrying the appropriate charge to participate in the interaction—but for which there is then a sum over three different positions for that colour of preon. For the photon the net EM vertex factor per preon is therefore $\sqrt{\alpha}/3$, in contrast with $\sqrt{2\alpha}[1 + O(\alpha)]$ for gluons. Equivalently, emission by a fermion of a specific gluon is a single-preon process, whereas emission by a fermion of a photon is a collective process.

For the rest of the structure factor, the diagram this time is a simple photon loop correction to a boson emission vertex, for a factor of $1/(2\pi)$, and has no hidden crossings. Mapping to a standard photon loop correction to an emission vertex (Fig. 6) involves reversing the time orientation of one of the preon limbs, but also reversal of charge and parity at its source and sink operators, for a sign of $+1$. Both diagrams have equivalent symmetry factors from vertex exchange. The boson is diagonal, so the total structure factor is $2\alpha/9$. The net correction is therefore

$$3 \cdot 3 \cdot \frac{2\alpha}{9} \cdot 1 \cdot \frac{1}{4\pi} = \frac{\alpha}{2\pi}. \quad (15)$$

Next, the photon loop corrections to the W /quark diagrams of Eq. (V:6). For these it is helpful to compare the photon/preon interactions involved with those encountered in the photon loop correction to the W /lepton vertex just completed. There are numerous ways to count the interactions; one of the simplest is as follows: First, recognise that to host a diagram having the form of

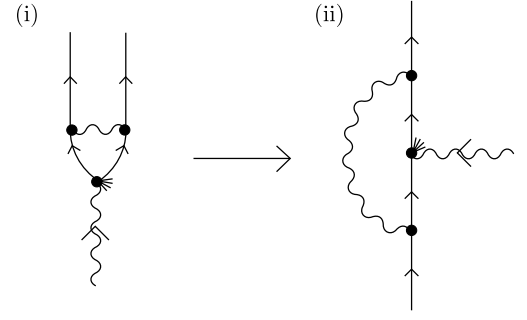


FIG. 6. Mapping of (i) a photon-mediated preon-preon interaction in Fig. 1(ii) to (ii) an emission vertex interaction exploits colour agnosticism, and involves both time reversal and charge and parity inversion for no net change of sign. The other four preons at the vertex are uninvolved, and are shown as truncated stubs.

Fig. 1(ii), a group of three preons or antipreons must include two charged constituents. This restricts such diagrams to the up quark limb, and for a given configuration of preons there is only one such pair, in contrast with three choices in the W /lepton diagram. However, even while remaining colour-agnostic, there are now three different configurations of preons available, corresponding to the choice of which preon is uncharged. Overall, the photon loop may therefore once again be in any of three different positions (one for each of the three configurations). The remainder of the calculation proceeds identically, and the electromagnetic loop factor for the W /quark mass vertex is therefore equivalent to that for the W /lepton mass vertex.

For Z boson loop corrections, a little more caution is needed. When computing photon loop corrections, all photon emission processes are additive. However, when emitting the bosons for Z loops, some destructive interference takes place. Recognise that there are two vertices which may contribute to the sign of Z emission—the coupling between the W boson and the background preon fields, which gives rise to different preon and antipreon triplets with varying weights, and the coupling between these triplets and the emitted Z field which goes on to form the loop correction. When looking for cancellations it is convenient to treat the preon triplet collectively as a fermion, and the same with the antipreon triplet. However, once cancellations have been identified, it is then necessary to return to a preon picture to evaluate the surviving loops. In the present context the W boson couples to $e_L \bar{\nu}_e$ and $d_L \bar{u}_L$ with equal vertex weight, and these constituents then couple to the Z field with the strengths shown in Table II. Comparison of coefficients reveals that the different Z emission processes on the preon lines cancel, as do the couplings of the individual preons within u_L , and only emission from the antineutrino sector of the antipreon line persists.

The Z loops on the antineutrino preon triplet may then be mapped to an effective overall vertex correction exactly as was done for the photon loops. To evaluate

this loop correction by reduction to a previously solved problem, recognise that the relative strengths of the one-photon and one- Z boson loop corrections to lepton magnetic moment are

$$2\alpha \cdot 1 \cdot \frac{1}{4\pi} \quad \text{and} \quad -f_Z \alpha \cdot \mathbf{f} \left(\frac{m_\ell^2}{m_W^2} \right) \cdot \frac{1}{4\pi} \quad (16)$$

where f_Z is the Z boson loop structural factor

$$f_Z := \frac{1}{3} \left[(4 \sin^2 \theta_W - 1)^2 - 5 \right] \\ = \frac{1}{3} \left(4 - 24 \frac{m_W^2}{m_Z^2} + 16 \frac{m_W^4}{m_Z^4} \right) \quad (17)$$

$$\sin^2 \theta_W = 1 - \frac{m_W^2}{m_Z^2}. \quad (18)$$

In the present context

1. the W boson is effectively massless, eliminating $\mathbf{f}(\cdot)$, and
2. the average vertex factors are -1 (for neutrinos) instead of $1/2$ (for electrons), for a relative factor of 4.

The one- Z -loop correction term arising from the $e_L \bar{e}_L$ base diagram after eliminating cancelled terms may thus be obtained by taking the one-photon-loop correction to the lepton magnetic moment, multiplying by the above two factors, and then further multiplying by the ratio of the structure coefficients for the one- Z -loop and one-photon-loop corrections to the lepton magnetic moment. This gives

$$\frac{\alpha}{2\pi} \cdot 4 \cdot -\frac{f_Z \alpha}{2\alpha} = -\frac{f_Z \alpha}{\pi} \quad (19)$$

TABLE II. When a W boson couples to the background fields, it does so to multiple particle species. This table summarises the weights of the W /preon couplings (vertex weight), the coefficients of these species' couplings to the Z boson field, and the relative contributions of each choice of fermion species to diagram Fig. 1(i) as a whole (loop weight). FSF factors are omitted for brevity. Species e_L and d_L are seen to occur with equal vertex weights, and have opposite coupling coefficients to the Z field, indicating that their contributions to Z emission cancel. There is no residual Z emission on the preon lines, only the antipreon lines.

Preon lines			
Species	Vertex weight	Z coefficient	Loop weight
e_L	f	$\frac{2f}{\sqrt{6}} \cdot \frac{1}{2}$	$\frac{1}{2}$
d_L	f	$\frac{2f}{\sqrt{6}} \cdot -\frac{1}{2}$	$\frac{1}{2}$
Antipreon lines			
Species	Vertex weight	Z coefficient	Loop weight
$\bar{\nu}_e$	f	$\frac{2f}{\sqrt{6}} \cdot -1$	$\frac{1}{2}$
\bar{u}_L	f	0	$\frac{1}{2}$

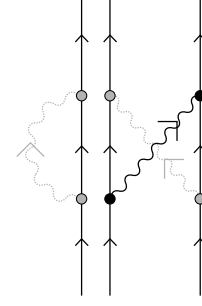


FIG. 7. Prototype of the boson exchange process involved in a W loop correction to Fig. 1(i), with co-ordinate transformations represented as pale dotted bosons carrying off-diagonal A -sector representations but zero momentum.

which is positive as $f_Z < 0$.

This is the correction term arising from the $e_L \bar{e}_L$ loop after eliminating cancelled terms, whereas the correction term arising from the $d_L \bar{u}_L$ loop after eliminating cancellations is zero. The relative contributions of each type of loop to the overall mass process are given by squaring the vertex weights and normalising so that they sum to 1, to obtain the loop weights. In this instance these correspond to equal contributions, and the average correction factor is thus

$$-\frac{f_Z \alpha}{\pi} \cdot \frac{1}{2} + 0 \cdot \frac{1}{2} = -\frac{f_Z \alpha}{2\pi}. \quad (20)$$

Finally, for W boson loop corrections, recognise that for fermions, $W^{(\dagger)}$ emission is a species-changing activity accompanied by a change of co-ordinates on the A sector (see Sec. III E 4 of Paper III). Collectively the preon limb may convert from e_L to ν_e or from d_L to u_L with emission of W , followed shortly by reabsorption of the same, with conjugate processes on the antipreon limb.

However, now consider the accompanying co-ordinate changes which maintain the fermion as a valid species in accordance with the gauge choices of Sec. III C 6 of Paper III and their implications for supported fermions (Sec. III D 1 of Paper III). These changes are conjugate, and may be represented as exchange of a boson in the e_{ij}^A basis with zero momentum but appropriate A -charges. The W boson must be emitted and absorbed on different preons, and thus the prototype for such diagrams is as per Fig. 7. This diagram is the same for leptons and quarks:

- For leptons, the interaction may be with any preon, but diagrams yielding preon PSE terms do not contribute to the vertex correction.
- For quarks, the interaction must be with the unique preon, but that preon may do so from one of three different positions:
 - On average, as noted in Sec. III B 2 of Paper IV, each A -sector interaction is accompanied by one C -sector interaction. Over

the course of a loop correction involving two preons, labelled 1 and 2, and not involving preon 3, the two associated C -sector interactions may realise any two of the following with equal likelihood:

- * preon 1 may interact with preon 3,
 - * preon 2 may interact with preon 3, and
 - * preon 1 may interact with preon 2.
- Any of these interactions may freely transfer any amount of the foreground momentum being carried as fluctuations by the preons involved, and any colour rearrangement over the three preons may be realised. In a context where position is integrated over, this arbitrary rearrangement of all properties except A -charge is equivalent to an arbitrary repositioning of the unique A -charge between the two vertices. Thus the position of the interacting preon is independent at source and sink.

Now recognise that as per Appendix A, the massless foreground W correction reduces to an interaction at a spatial point. Similarly, the co-ordinate change boson connecting the participating preons is a W boson exchange which is restricted to an interaction at a single point in momentum space. The resulting correction factors are equivalent under fourier transform, implying equivalent boson emission strengths, and the bosons have opposed orientations. The result is net zero W field at the point of emission, indicating that the contribution from the W loop must vanish.

4. Scalar boson loops

For scalar bosons the overall approach is similar to that taken for vector bosons, though the diagrams are different, being shown in Fig. 8. The preons within a scalar boson may be crossed or uncrossed.

Considering first Fig. 8(i), for a given set of preons in the fermion fields this diagram yields one of nine terms in the sum making up the scalar boson. Recalling the factor of $O(N_0^{-2})$ attracted by any scalar boson propagating to the far field, this term is dominated by the contribution when the two vertices coincide as shown in Fig. 9(i). As per Sec. III E 5 of Paper III, terms where the source and sink are separate then correct this diagram by at most $O(N_0^{-4})$. Further, now consider colour consistency and recognise that at either of the loop vertices in Fig. 8(i), both preons in the fermion must be of different colour while both preons in the scalar boson must be the same. This can only be reconciled if the two vertices are collocated, and thus may be rewritten as a single colour-conserving vertex. Any diagrams where the termini of the scalar boson loop do not coincide—written as $O(N_0^{-4})$ above—must therefore vanish. (This collocation is relaxed very slightly on noting that colour may be borrowed from the background field, but only

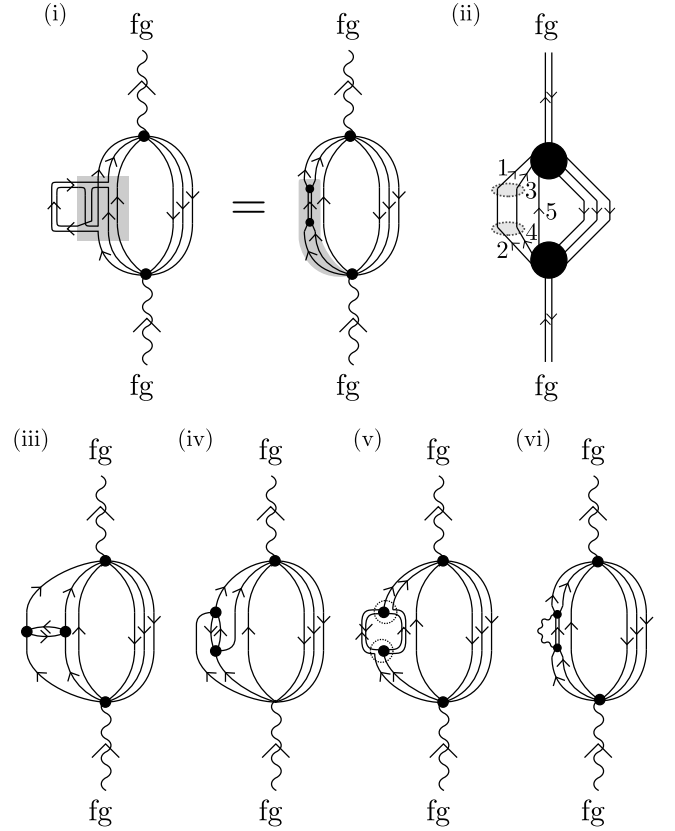


FIG. 8. Structures of loop corrections to W /fermion vertices involving scalar bosons. Diagram (i) shows the simplest scalar boson loop correction—in the first form, the shaded area corresponds to scalar boson emission as per Fig. 6 of Paper III. In the second form this is simplified by diagrammatic isotopy. The shaded region of the second form comprises the correction loop, which may be contracted into a numerical correction to the lower vertex (or into the upper vertex if preferred, though this represents two ways to evaluate the same diagram, not a twofold degeneracy). Within the scalar boson, the preons may be crossed or uncrossed, though only uncrossed is shown. Colour inconsistency within the scalar boson is addressed in the main text, by reduction to Fig. 9. Diagram (ii) shows the preon expansion for the uncrossed configuration, and labels the preons which may participate in the pseudovacuum expansion. The different labellings are enumerated in Table III. Diagrams (iii)-(vi) construct a further scalar boson loop correction: Begin with Fig. 1(ii) and first (iii) redraw the vector boson as a pair of preons. Then (iv) use diagrammatic isotopy to rotate the resulting loop. (v) Group the preons as shown, and introduce effective vertices at the top and bottom of the loop which encompass both the existing vertices (factor of f apiece) and the preon redistribution operations (factor of 1 apiece). The end result is diagram (vi), which is equivalent to diagram (i) supplemented by a further massless vector boson loop with effective vertex factors of 1. This must be considered in addition to Fig. 1(ii) as the mass shell of the resultant foreground scalar boson is distinct from that of the vector boson in Fig. 1(ii) so it is treated as a separate effective excitation.

over \mathcal{L}_ψ , assumed to be the smallest scale of the model.

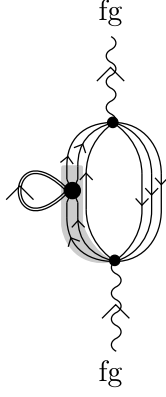


FIG. 9. The contribution of Fig. 8(i) to W boson mass is dominated by contributions made when the two interaction vertices coincide, as shown here. However, given the underlying structure of Fig. 8(i) this should not be mistaken for a loop correction to the propagator. As a loop correction to Fig. 1(i), the resulting factor is still absorbed into either the upper or the lower vertex, with the latter being indicated by the shading.

Similar considerations are applicable to all fermion/ H interactions of the sort shown in Fig. 6 of Paper III.) Note that the factor associated with the effective colour-conserving vertex is determined by its construction from two disparate vertices (and integrating out their accessory degrees of freedom)—there is no need to assign an additional factor of two due to on-vertex symmetries.

It is now useful to compare this scenario with the vector boson loop correction of Fig. 1(ii):

- For the vector boson loop, the contribution is determined by the contribution when the loop vertices coincide, as discussed in the Appendix A.
- For the scalar boson loop, the contribution is determined by the contribution when the loop vertices coincide, as discussed for Fig. 9 above.
- For the vector boson loop, this is equivalent to contracting the boson loop into either the upper or the lower vertex.
- For the scalar boson loop, writing the correction as a numerical multiplier on the original diagram is likewise equivalent to contracting the boson loop into either the upper or the lower vertex.
- In both cases, the choice of contracting into the upper or lower vertex is a descriptive one. Although it represents a symmetry in the calculation such that there are two equivalent ways of *evaluating* the associated Feynman diagrams, these do not correspond to different diagrams, and hence there is no factor of 2 associated with this.

To evaluate Fig. 8(i), first recognise that with the preons crossed, the resulting preon diagram has the same

preon structure as Fig. 3(ii)—the colour sector is summed (corresponding to the sum over terms in the scalar boson) rather than averaged, but the net result is the same up to an overall multiplier. Further, both of these diagrams are dominated by contributions in which the separation of the boson vertices approaches zero. This diagram will consequently evaluate equivalent to the photon loop of Fig. 3(i) up to an overall multiplier to be determined explicitly now. Whereas the photon loop accrues an overall factor of $2 \cdot (4\pi)^{-1}$, for the scalar boson take note of the following:

- For coupling coefficients,
 - the raw vertex coefficient is f in place of $f/\sqrt{2}$,
 - Each preon/scalar boson coupling should be understood in the context of a fermion/scalar boson coupling and thus attracts a factor of $\frac{1}{3}$ per vertex from the definition of the fermion (III:28). As with the photon, the total net coupling is averaged across the three preons by this factor.

The coupling coefficient is consequently $(2\alpha/9)[1 + O(\alpha)]$.

- Also contributing to the structure factor,
 - there is no symmetry under exchange of boson source/sink (factor 1), and
 - unlike the photon the complex scalar boson is not written in terms of $\sigma^\mu \sigma_\mu$ (factor $-\frac{1}{2}$).

The structure factor, incorporating the vertex coefficient, is consequently $-(\alpha/9)[1 + O(\alpha)]$ compared with the photon's $2\alpha/9$.

- Regarding the pseudovacuum expansion and crossed and uncrossed preon lines,
 - the crossed preon configuration admits three pseudovacuum expansions, directly equivalent to those of Fig. 1(ii), while
 - the uncrossed preon configuration admits four pseudovacuum expansions, elaborated below. These have one less crossing and are therefore of opposite sign.

The net factor arising from pseudovacuum expansions and preon crossings in combination is therefore -1 .

- For other factors:
 - Three choices of preon pairs in the ascending limb, three choices in the descending limb, yield six diagrams.
 - The above evaluates the contribution of one of nine terms in the scalar boson sum. All terms contribute, as excitation of any one leads to excitation of all by unbroken $SU(3)_C \otimes GL(1, \mathbb{R})_N$ symmetry, for a further factor of 9.

To evaluate pseudovacuum expansions for Fig. 8(i) with the preon lines in the scalar boson uncrossed, label as per Fig. 8(ii) and expand as per Table III. Following the same arguments employed to identify connected diagrams in Sec. IV A 1 above, only one option out of each pair (1,3) and (4,6) need be retained, and this should be the one in which there is no foreground connection between upper and lower vertices.

It is also worth noting the caution required around the sign of scalar boson contributions to pseudovacuum expansions. In identifying the crossed preon configuration with the preon expansion of Fig. 1(ii), these diagrams are seen to have equivalent sign, and the uncrossed configurations to have the opposite sign. However, without making the pseudovacuum expansion explicit, it would have been easy to assume that all scalar boson loop terms had a minus sign relative to the vector boson terms due to the presence of an additional fermion loop in Fig. 1(i). It is always advisable to perform explicit preon expansions to check signs of terms in diagrams involving both scalar bosons and loops.

Putting together the above, the net factor associated with Fig. 8(i) [with terms ordered as per Eq. (14), and the extra factor from the nine terms in the scalar boson at the end] is

$$-1 \cdot 6 \cdot -\frac{\alpha}{9}[1 + O(\alpha)] \cdot 1 \cdot \frac{1}{4\pi} \cdot 9 = \frac{3\alpha}{2\pi}[1 + O(\alpha)]. \quad (21)$$

Next, consider Fig. 8(vi). This diagram is obtained by transforming the photon loop correction of Fig. 1(ii), but must be considered a separate figure as it involves the scalar boson, which propagates as a distinct entity under the Lagrangian on $\mathbb{R}^{1,3}$. The pair of loops may be decomposed into two independent multiplicative factors, one corresponding to a scalar boson and directly equivalent to Fig. 8(i), and another arising from the massless vector boson with interaction vertices of value 1. Note that as with Fig. 8(i) reducing to Fig. 9, the vertices of the scalar boson in Fig. 8(vi) must likewise be brought to coincide. The resulting scenario is very similar to that encountered in Sec. III 3 of Paper V—compared with a photon loop, relative factors are as follows:

TABLE III. List of labellings of preon lines in Fig. 8(ii). For brevity, labellings in which preon 5 is foreground have been omitted as these are always “connected” so never contribute to the mass correction.

Option	Background	Foreground	Status
1	1,2,5	3,4	Connected
2	1,3,5	2,4	Valid
3	1,4,5	2,3	Valid
4	2,3,5	1,4	Valid
5	2,4,5	1,3	Valid
6	3,4,5	1,2	Connected

- The boson loop contains only the appropriate preons, so there is no factor of $1/\sqrt{2}$ associated with the vertex. The coupling would consequently be $2\alpha[1 + O(\alpha)]$ in place of α . However, this is then replaced with 1 as there are no factors of f associated with the vector boson loop. Net relative factor: α^{-1} .
- No extra symmetry factor for on-vertex interchange of boson ends where compatible, as the effective vertex has been synthesised from two subvertices and not drawn down from the generator \mathcal{Z} .

The vector boson loop on diagram (iv) therefore contributes an additional multiplier of $2 \cdot (4\pi)^{-1}$ for a total factor from Fig. 8(vi) of

$$\frac{3\alpha}{2\pi} \cdot \frac{1}{2\pi}. \quad (22)$$

Combining with Fig. 8(i) yields a net scalar boson loop correction factor of

$$\frac{3\alpha}{2\pi} \left(1 + \frac{1}{2\pi}\right). \quad (23)$$

5. Net effect of all boson loops

The net effect of the boson loop corrections is therefore to amend the W boson mass equation to

$$m_W^2 = 9f^2 \left[k_1^{(e)}\right]^4 \omega_0^2 N_0^{12} S_{6,13} \times \left[1 + \left(64 + \frac{3}{2\pi} - f_Z\right) \frac{\alpha}{2\pi} + O(N_0^{-4}) + O(\alpha^2)\right] \quad (24)$$

$$S_{6,13} := N_0^{-4}(N_0 + 2)^2(N_0 + 1)^2 = 1 + 6N_0^{-1} + 13N_0^{-2} + \dots \quad (25)$$

$$f_Z = \frac{1}{3} \left(4 - 24 \frac{m_W^2}{m_Z^2} + 16 \frac{m_W^4}{m_Z^4}\right) \quad (26)$$

where $S_{6,13}$ was previously introduced in Eqs. (III:79), (IV:10) and (V:7), and the next-most-relevant members of the correction series are those due to the coupling of the W boson to the background photon and scalar fields {which are smaller by a factor of $[k_1^{(e)} N_0]^{-4}$ }, the second-order electromagnetic corrections [with leading contribution being of $O(\alpha^2)$], and the various factors of $[1 + O(\alpha)]$ in the above calculations which correct terms already containing α and thus are also of $O(\alpha^2)$.

Later evaluation of $k_1^{(e)}$ (152) shows the term in $[k_1^{(e)} N_0]^{-4}$ to be between $\alpha/(4\pi)$ and $\alpha^2/(4\pi)^2$ in magnitude, so this is evaluated shortly.

Regarding the notation $k_1^{(e)}$ in the above:

- When particle masses are evaluated beyond tree level, the mass matrices incorporate higher-order

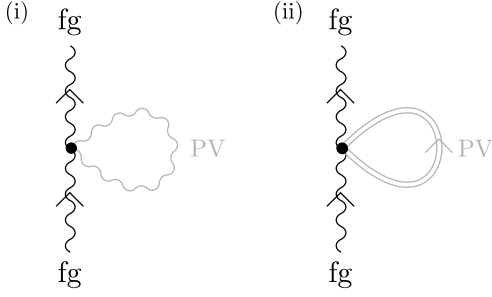


FIG. 10. (i) Coupling between W boson and background photon field. (ii) Coupling between W boson and background scalar field. For the scalar boson there is no need to separately consider crossed and uncrossed configurations or FSF exchange in the absence of foreground fields, as all such symmetry factors are incorporated into the mean-squared background field value.

corrections which are themselves dependent on the particle masses and thus vary between fermion species.

- It is seen in Sec. V C that many of these corrections admit a natural description as corrections to the Koide angle θ_f in Eq. (IV:27), which then exhibits dependency on particle species and energy scale.
- As the eigenvalues of the colour-mixing K matrix are dependent on the value of θ_f , these also become dependent on particle species and energy scale.

Thus the parameter k_g of Paper IV is replaced by $k_g^{(f)}$, which is defined in Sec. V A 1. It carries labels f and g where f indicates the family of fermions for which k is calculated, and g is the particle generation; $k_g^{(f)}$ is then eigenvalue g of the energy-dependent colour mixing matrix $K_f(\mathcal{E})$ which is associated with the fermion family containing species f , evaluated at the energy scale m_{f_g} where f_g denotes generation g of the family containing f . As a matter of notation, f will generally be taken as the lightest member of the family, and thus (for example) $k_2^{(e)}$ represents the second eigenvalue of $K_e(\mathcal{E})$, evaluated at energy scale $\mathcal{E} = m_\mu c^2$.

6. Background photon and scalar interactions

Another potentially relevant correction is the W /background photon coupling, Fig. 10(i). At tree level this readily evaluates to

$$\frac{f^2}{2} N_0^8 S_{6,13} \quad (27)$$

where a symmetry factor of 2 arises from the presence of two identical photon operators on the interaction vertex, but is cancelled by the diagrammatic equivalence of exchanging the connected photon lines/sources/sinks. This

gives a net expression

$$m_W^2 = 9f^2 \left[k_1^{(e)} \right]^4 \omega_0^2 N_0^{12} S_{6,13} \times \left\{ 1 + \left(64 + \frac{3}{2\pi} - f_Z \right) \frac{\alpha}{2\pi} + \frac{1}{18 \left[k_1^{(e)} N_0 \right]^4} [1 + O(\alpha)] + \dots + O(\alpha^2) \right\}. \quad (28)$$

The composite pseudovacuum scalar boson field yields a similar contribution, represented by “...” in the above. In comparison with the photon term:

- In contrast with $A^\mu A_\mu$, the complex scalar boson operators \mathbf{H} and \mathbf{H}^* are no longer interchangeable. However, each vertex may be either an \mathbf{H} vertex or an \mathbf{H}^* vertex. The resulting factors of 2 and $\frac{1}{2}$ cancel, for no net change in on-vertex symmetry.
- Because scalar boson source and sink are located on the same vertex, the loop may be contracted to a point and as discussed in Sec. III E 5 of Paper III there is therefore no factor of $2N_0^{-4}$ for taking the scalar bosons to the far field.
- The vertex coupling factor is obtained from the Lagrangian. It includes evaluation of $(i/2)^2 \Upsilon^\mu \Upsilon_\mu$, and recognition that the pair may be constructed either as $\mathbf{H}\mathbf{H}^*$ or $\mathbf{H}^*\mathbf{H}$. It evaluates as $-2f^2$. This is compared with $f^2/2$ for the photon, for a relative factor of -4 . (It is interesting to compare this with the approach taken for the scalar boson loops of Sec. IV A 4, in which loops were evaluated by reduction to a previously solved problem rather than direct construction from the Lagrangian. The minus sign seen here corresponds to the one obtained in Sec. IV A 4 from sigma matrices, which was included in the loop structure factor.)
- Comparing Eqs. (4) and (9), the mean field value for $[\mathbf{H}\mathbf{H}^*]_{\text{bg}}$ attracts a factor of $-9/2$ relative to that for $[A^\mu A_\mu]_{\text{bg}}$.

The scalar boson term is consequently larger than the photon term by a factor of

$$1 \cdot -4 \cdot -\frac{9}{2} = 18. \quad (29)$$

Incorporating the background scalar boson contribution to m_W^2 therefore yields

$$m_W^2 = 9f^2 \left[k_1^{(e)} \right]^4 \omega_0^2 N_0^{12} S_{6,13} \times \left\{ 1 + \left(64 + \frac{3}{2\pi} - f_Z \right) \frac{\alpha}{2\pi} + \frac{19}{18 \left[k_1^{(e)} N_0 \right]^4} [1 + O(\alpha)] + O(\alpha^2) \right\}. \quad (30)$$

There is no equivalent gluon coupling as the W boson is colourless. Any attempts to construct a coupling to the C sector background will vanish on summation over emission coefficients, similar to the cancellation seen while evaluating the Z coupling in Sec. IV A 3 above.

7. Universality of loop corrections

Up to now, the photon in Fig. 10 has been treated as a fundamental particle. However, in principle any occurrence of a fundamental boson may be re-expressed as a pair of preons using the identity

$$\varphi_\mu^{\dot{a}\dot{c}ac} = \bar{\partial}^{\dot{a}\dot{c}} \bar{\sigma}_\mu \partial^{ac} \varphi \approx f \bar{\partial}^{\dot{a}\dot{c}} \varphi \bar{\sigma}_\mu \partial^{ac} \varphi = f \bar{\psi}^{\dot{a}\dot{c}} \bar{\sigma}_\mu \psi^{ac} \quad (31)$$

derived from Eqs. (I:134) and (I:196). Such pairs are bound by the colour interaction with a characteristic separation of $O(\mathcal{L}_\psi)$, but this is also the preon separation observed at the vertices of the W /lepton diagrams such as Fig. 1(i).

With this in mind, consider again the preon-mediated boson mass vertex of Fig. 1(i). In Sec. III 1 of Paper V the interaction between the vector boson and the preon fields was taken to involve all three preons, collected as a composite fermion, leading to the introduction of K matrices on two of the preon lines at each vertex. Although integration reduced two preon lines and two antipreon lines to a numerical factor using Eq. (7), these lines still interacted with the foreground field, permitting them to acquire FSF symmetry factors (which may be understood as corresponding to a choice over which preon lines the K matrices are applied to).

An alternative approach to the evaluation of Fig. 1(i) is to interpret the six preons as three vector bosons. This construction has no K matrices, and corresponds to the diagrams without K matrices discussed in Sec. III 1 e of Paper V. After integrating out four of the lines, the remaining lines are collected as emission and absorption of vector bosons from the background field. This requires that each boson constructed involves a preon from one vertex and an antipreon from the other vertex. (Choosing both from the same vertex just yields a propagator of the foreground boson over the intervening space.) In contrast with the background fermion diagrams, since there are no K matrices associated with boson-boson interactions, the normalisation convention of Sec. III H 6 of Paper I requires that the eliminated lines yield a net factor of 1.

If the residual background bosons are conjugate, then this constitutes a reduction of Fig. 1(i) to a diagram having the general form of Fig. 10(i). However, the species involved may be unexpected, and this may represent an additional channel of interaction between the foreground boson and the background boson fields which must also be taken into account. For the W boson this contribution vanishes, however, as the resulting background bosons are associated with orthogonal representation matrices

on the A sector (e_{22}^A and e_{33}^A) and therefore have a vanishing mean product on the pseudovacuum.

Now consider diagrams having the form of Fig. 1(ii) which contain loop corrections. The preons persisting after integration no longer necessarily arise from the same vertices, but this is unimportant as they are still within \mathcal{L}_ψ of one another and can therefore once again be considered to make up composite vector bosons, again yielding a coupling to the boson sector of the pseudovacuum. (Again these vanish for the W boson.)

Crucially, however, the converse process may be applied to any boson loop diagram such as Fig. 10(i), recruiting an additional two bosons (two preon lines and two antipreon lines) from the pseudovacuum. Choice of gauge ensuring that this recruitment yields triplets consistent with fermions. The recruited preons permit reconstruction of a diagram having the form of Fig. 1(i), without K matrices. Such a reconstructed six-preon-line diagram then admits all of the loop corrections identified for Fig. 1 above. This mapping therefore identifies a set of nontrivial higher-order correction to the boson loop diagram of Fig. 10(i) which can *only* be obtained by mapping the interacting bosons into preon constituents and recruiting additional preons from the pseudovacuum to make up preon vertices before integrating them out again. [Note that this recruitment (i) is always possible due to the homogeneity of the pseudovacuum and the large number of background particles within auto-correlation length \mathcal{L}_0 , and (ii) is obligatory as it provides additional channels for interaction between a propagating boson and the background fields.] Further recalling that the scalar boson loop in Sec. IV A 4 was evaluated by mapping to a vector boson loop, equivalent corrections also apply to the scalar boson loop diagram of Fig. 10(ii).

The net outcome is that every term in Eq. (24) has a counterpart on the boson loops of Fig. 10. The W boson mass may then concisely be written as

$$\begin{aligned} m_W^2 = & 9f^2 \left[k_1^{(e)} \right]^4 \omega_0^2 N_0^{12} S_{6,13} \\ & \times \left[1 + \left(64 + \frac{3}{2\pi} - f_Z \right) \frac{\alpha}{2\pi} + O(\alpha^2) \right] \\ & \times \left\{ 1 + \frac{19}{18 \left[k_1^{(e)} N_0 \right]^4} [1 + O(\alpha)] \right\}. \end{aligned} \quad (32)$$

Later evaluation of $k_1^{(e)}$ (152) shows the term in $\left[k_1^{(e)} N_0 \right]^{-4}$ to be between $\alpha/(4\pi)$ and $\alpha^2/(4\pi^2)$ in magnitude, and the factor $[1 + O(\alpha)]$ on this term therefore introduces corrections which are small compared with $O(\alpha^2)$. However, pending demonstration of this, Eq. (32)

may be written

$$m_W^2 = 9f^2 \left[k_1^{(e)} \right]^4 \omega_0^2 N_0^{12} S_{6,13} \left[1 + \left(64 + \frac{3}{2\pi} - f_Z \right) \frac{\alpha}{2\pi} \right] \\ \times \left\{ 1 + \frac{19}{18 \left[k_1^{(e)} N_0 \right]^4} \right\} \\ \times \left(1 + \mathcal{O} \left\{ \alpha \left[k_1^{(e)} N_0 \right]^{-4} \right\} + \mathcal{O}(\alpha^2) \right). \quad (33)$$

This universality of the preon-level loop corrections to all interactions—boson and fermion—and the involvement of both boson and fermion terms in the calculation of boson masses—even where, as for the W boson, these disappear—has the important implication that corrections to the Weinberg angle θ_W are likewise universally applied, regardless of whether θ_W is expressed in terms of boson masses or interaction strengths. Thus the mass ratio expression for θ_W in the definition of f_Z (17) is consistent with the interaction ratio expression $\tan \theta_W = g'_{\text{eff}}/g_{\text{eff}}$ once all corrections to interaction strengths with no counterparts in the Standard Model have been taken into account.

This completes calculation of W boson mass to the level of precision employed in this paper.

B. Z mass

Higher order corrections to the Z boson mass are also required, and their calculation is similar to that for the W boson.

1. Boson loops

a. Gluon loops: The calculation is analogous to that performed for the W boson. However, introduction of an off-diagonal gluon coupling rearranges colour and so eliminates the end-to-end symmetry of the Z boson mass-squared interaction, resulting in the loss of a symmetry factor of 2 relative to the original diagram. There are no diagonal gluon couplings consistent with Fig. 1(ii), so this reduction applies to all gluon loop corrections. The net gluon contribution is therefore

$$\frac{30\alpha}{2\pi}. \quad (34)$$

An alternative explanation of this reduction in factors is given by noting that the original background fields are summed over connection to the source and sink in two different orientations (corresponding to the symmetry factor of two). When the same exchange is applied to a diagram with a loop correction in the preon limb, this maps to a loop correction in the antipreon limb. Counting all six positions for loop corrections is therefore dou-

ble counting, and again the contribution must be reduced by a factor of two.

b. Photon, W , and Z boson loops: These calculations follow the approach described in Sec. IV A 3. The photon and W boson are readily dismissed:

- The Z boson has no electromagnetic charge, so on constructing a photon-loop coupling table all terms are immediately seen to vanish.
- The W boson loop correction vanishes by the same argument as Sec. IV A 3 above.

For Z loops, however, the coupling table does not sum to zero and so is computed here. Consider the relative contributions of the different fermions which contribute to the leading order diagram [analogous to Fig. 1(i)]. At tree level the Z boson couples only to electrons, neutrinos, and the down quarks. The relative contribution of each line to the Z field of the loop boson is the product of the vertex weights and the Z coefficients, given for the preon limb in Table IV. All such terms are of identical sign so no cancellation takes place.

Each choice of fermions in the loop then acquires corrections from all uncanceled terms (i.e. all terms, in this context). These must be evaluated at the preon level, but a shortcut is possible on recognising that:

- In the leptons,
 - the three preons are identical, and after incorporating the fermion normalisation, each contributes an effective Z coupling $\frac{1}{3}$ that of the corresponding fermion as per Sec. III E 8 of Paper III.
 - The sum over three loop positions and three pseudovacuum expansions per loop cancels with resulting the factor of $\frac{1}{9}$.

TABLE IV. List of channels contributing to the preon limb of the leading order Z boson mass diagram, the Z /preon couplings (vertex weights), coefficients of coupling to the (loop) Z boson field, and the relative contributions of each choice of fermion species to the leading-order mass as a whole (loop weight). Terms for the antipreon limb are identical up to a sign on both vertex weight and Z coefficient representing the selection of the CP -conjugate at the boson/fermion vertex, and the opposite sign of interaction of this conjugate with the Z boson.

Preon lines			
Species	Vertex weight	Z coefficient	Loop weight
e_L	$\frac{2f}{\sqrt{6}} \cdot \frac{1}{2}$	$\frac{2f}{\sqrt{6}} \cdot \frac{1}{2}$	$\frac{1}{8}$
\bar{e}_R	$\frac{2f}{\sqrt{6}} \cdot \frac{1}{2}$	$\frac{2f}{\sqrt{6}} \cdot \frac{1}{2}$	$\frac{1}{8}$
ν_e	$\frac{2f}{\sqrt{6}} \cdot -1$	$\frac{2f}{\sqrt{6}} \cdot -1$	$\frac{1}{2}$
d_L	$\frac{2f}{\sqrt{6}} \cdot -\frac{1}{2}$	$-\frac{2f}{\sqrt{6}} \cdot -\frac{1}{2}$	$\frac{1}{8}$
\bar{d}_R	$\frac{2f}{\sqrt{6}} \cdot -\frac{1}{2}$	$-\frac{2f}{\sqrt{6}} \cdot -\frac{1}{2}$	$\frac{1}{8}$

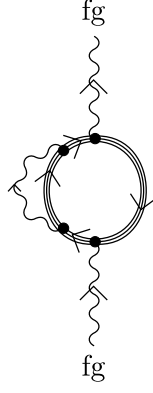


FIG. 11. A boson loop coupling a fermion to itself as shown may be expanded to yield preon proper self-energy terms and three preon-preon couplings between members of the fermion triplet.

- In the quarks,
 - as discussed in Sec. IV A 3, each A -sector interaction is accompanied by one C -sector interaction. Collectively these interactions have the effect of arbitrarily rearranging the preons between the two vertices, so the sum over position of the interacting preon proceeds independently at source and sink.
 - If source and sink are time-ordered this yields six loop diagrams; they are not time-ordered, so this reduces to three.
 - Again, each diagram has three different pseudovacuum expansions.
 - Again this cancels a factor of $\frac{1}{9}$ from fermion normalisation.

The net result is that for both leptons and quarks, the numerical factor associated with all preon/ Z /preon loops within a given fermion is precisely the same as the factor associated with a Z loop coupled at each end to that fermion, as shown in Fig. 11, if one ignores that such a term would normally be absorbed in to the fermion PSE. Indeed, expanding each vertex in terms of the three possible preon couplings yields nine diagrams, of which three couple a preon to itself so are not loop corrections to the vertex, but the other six are precisely those diagrams which provide the loop corrections. (More generally, Fig. 11 is used to describe both a PSE correction to the fermion propagator *and* the loop corrections to a boson/fermion vertex, being normalised away in the former, and yielding a numerical factor in the latter.)

In light of the above, the mean Z loop coefficient on the preon limb, after summing over preon diagrams and pseudovacuum expansions, may be calculated as the square of the $Z/\text{fermion}$ coefficient (the vertex factor in Table IV) multiplied by the loop weight. This evaluates as $5f^2/12$. The calculation is the same on the antipreon limb, so the mean value is the same across all species and diagrams.

It will be corrected to $O(\alpha)$ by higher-order terms not explicitly evaluated.

Compare this with the photon loop correction to the W boson mass, where the equivalent mean factor across all species and diagrams is $f^2/2$, corrected by higher-order terms corresponding to $(1 + a_e)$. For the photon, the loop correction factor is $\alpha/(2\pi)$. On naïve inspection the Z boson loop correction to Z mass has twice as many loop diagrams as the photon correction to W mass (as the former includes both preon and antipreon terms, but the latter acquires loops only on the preon limb). Recalling that the Z boson is also effectively massless in this context, this would yield a net factor of

$$2 \cdot \frac{5f^2}{12} \cdot \left(\frac{f^2}{2}\right)^{-1} \cdot \frac{\alpha}{2\pi} \cdot \frac{1 + O(\alpha)}{1 + a_e} = \frac{5}{3} \cdot \frac{\alpha}{2\pi} [1 + O(\alpha)]. \quad (35)$$

However, this calculation overlooks additional symmetries present in the Z boson diagrams:

- For the photon loop corrections to the W mass:
 - With the exception of interchange of the loop vertices, which is accounted for in the structure factor, there are no other vertex interchange symmetries.
- For the Z loop corrections to the Z mass:
 - There are four identical $Z/\text{fermion}$ vertices, which admit 24 permutations. One such permutation suffices to generate all preon diagrams associated with a given position of the fermion vertices, so this appears to be a 24-fold overcounting.
 - However, symmetry under exchange of the two inner loop vertices is also present in the $W/\text{fermion}$ reference diagram and its associated factor of $\alpha/(2\pi)$, so factor this out and divide the count by two.
 - Similarly, symmetry under exchange of the two external loop vertices is included in the leading-order diagram of Fig. 1(i) which these figures correct, so again divide the overcount by a factor of two.
 - Now consider a nonvanishing loop correction diagram.
 - * To yield a nonvanishing correction the inner loop must have the form shown in Fig. 1(ii), and not that of Fig. 1(iii) which is instead a preon PSE diagram. However, the positions of the outer loop vertices are not similarly constrained.
 - * All remaining vertex exchange operations swap at least one vertex from the inner loop with a vertex from the outer loop.
 - * There is therefore a one-in-three chance that the diagram resulting from a vertex

exchange will have vanishing contribution to the loop correction.

This reduces the count by a factor of $\frac{2}{3}$, for a final net overcount by a factor of 4.

To compensate for this overcount on mapping to fermions, introduce a complementary factor of $\frac{1}{4}$. The factor associated with the Z loop corrections to Z boson mass therefore becomes

$$\frac{1}{4} \cdot 2 \cdot \frac{5f^2}{12} \cdot \left(\frac{f^2}{2}\right)^{-1} \cdot \frac{\alpha}{2\pi} \cdot \frac{1 + \mathcal{O}(\alpha)}{1 + a_e} = \frac{5}{12} \cdot \frac{\alpha}{2\pi} [1 + \mathcal{O}(\alpha)]. \quad (36)$$

c. Scalar boson loop: The scalar boson loop calculation is identical to that for the W boson, yielding a correction of

$$\frac{3\alpha}{2\pi} \left(1 + \frac{1}{2\pi}\right). \quad (37)$$

d. Net effect of all boson loops: The net effect of the boson loop corrections is therefore to amend the Z boson mass equation to

$$m_Z^2 = 12f^2 \left[k_1^{(e)}\right]^4 \omega_0^2 N_0^{12} S_{6,13} \times \left[1 + \left(\frac{401}{12} + \frac{3}{2\pi}\right) \frac{\alpha}{2\pi} + \mathcal{O}(N_0^{-4}) + \mathcal{O}(\alpha^2)\right] \quad (38)$$

where the next-most-relevant corrections are those due to the coupling of the Z boson to the pseudovacuum scalar field, and the second-order electromagnetic corrections.

2. Background photon and scalar interactions

a. Direct coupling: As the Z boson is uncharged, it acquires no mass through direct coupling to the background photon field. However, it still interacts with the background scalar boson field. Following a similar calculation to Sec. IV A 6 and separating the series as per Sec. IV A 7 yields

$$m_Z^2 = 12f^2 \left[k_1^{(e)}\right]^4 \omega_0^2 N_0^{12} S_{6,13} \left[1 + \left(\frac{401}{12} + \frac{3}{2\pi}\right) \frac{\alpha}{2\pi}\right] \times \left\{1 + \frac{1}{\left[k_1^{(e)} N_0\right]^4}\right\} \times \left(1 + \mathcal{O}\left\{\alpha \left[k_1^{(e)} N_0\right]^{-4}\right\} + \mathcal{O}(\alpha^2)\right). \quad (39)$$

b. Indirect (universality) coupling: Rather surprisingly, however, there does exist a mechanism whereby the Z boson may acquire mass from the background photon field. Consider again the mechanism behind the universal applicability of boson mass-squared vertex loop corrections described in Sec. IV A 7. When the Z boson is

interacting with the preons of the pseudovacuum, this attracts the obvious leading-order term associated with the fermion interpretation of Fig. 1(i). However, for the Z boson it is also possible to construct nonvanishing diagrams from the three-boson interpretation discussed in Sec. IV A 7. Since the A -sector representation matrix associated with the Z boson is diagonal, the background bosons constructed from the residual preons are identical and self-conjugate, generating a diagram having the form of Fig. 10(ii).

A basis of diagonal bosons may be chosen consisting of the photon, Z boson, and N boson from which it is possible to construct any given composite vector boson with representation matrix e_{ii} . However, given the gauge choices of Sec. III C 6 of Paper III, any mass arising from this sector must always be attributed to the contributions of the background photon field. Consequently it is only necessary to consider triplets involving charged preons.

First, consider the lepton channels. When the preons are electron-type preons ($a \in \{1, 2\}$) there are three choices of charged preon and three choices of charged antipreon, and freedom to choose which preons to integrate out gives nine ways to make a composite vector boson whose a -charges indicate it relates to the photon. When the preons are neutrino-type preons ($a = 3$), these have no overlap with the photon and so can be ignored. The lepton sector thus offers a total of 18 channels (nine from e_L and nine from \bar{e}_R).

Next, consider the quark channels. Again, only diagonal contributions from electron-type preons are nonvanishing and thus each down quark contributes only one channel. The up quark does not couple to the Z boson.

For these twenty channels (nine each from the e_L and \bar{e}_R channels and two from d_L), now determine the weight of each channel when compared with the $WW^\dagger AA$ vertex of Fig. 10(i):

- On the electron diagrams:

- The background preon line retained at the upper vertex may be any one of three available.
- To construct a photon, the preon line at the lower vertex must be of matching colour. However, this may be in any of the three positions for a further factor of three (either from a sum over positions of an explicit label, or if colour labelling is suppressed, then from freedom to choose among three identical preons).
- After integrating out the eliminated preons, the upper and lower vertex act as a single composite vertex which exhibits two photon couplings. In scenarios where the preons *become* photons, as opposed to *emit* photons, there is consequently no cancellation between photon interactions arising from the e_L and \bar{e}_R sectors of the pseudovacuum.

Preon configurations consistent with background

fermions e_L and \bar{e}_R therefore contribute nine figures apiece.

- On the down quark diagrams:
 - The upper preon must be the unique preon. Its colour is whatever it is.
 - The lower preon must likewise be the unique preon. Its colour matches.

Preon configurations consistent with background quarks d_L and \bar{d}_R therefore contribute one figure apiece.

- In each of these twenty figures, there are three choices for colour of the retained preons, for a factor of 3.
- Vertex factors yield $f^2/6 = (\alpha/3)[1 + O(\alpha)]$.
- Symmetry under interchange of the Z boson source and sink is also present in the diagram which this figure corrects, so must be factored out—multiply by $\frac{1}{2}$.

Compared with the factor of $\frac{1}{2}f^2N_0^8S_{6,13}$ for the W/A coupling (27), this yields $\frac{5}{2}f^2N_0^8S_{6,13}$ for a net correction weight of

$$\frac{5}{18[k_1^{(e)}N_0]^4}[1 + O(\alpha)], \quad (40)$$

increasing the Z boson mass to

$$\begin{aligned} m_Z^2 = & 12f^2[k_1^{(e)}]^4\omega_0^2N_0^{12}S_{6,13}\left[1 + \left(\frac{401}{12} + \frac{3}{2\pi}\right)\frac{\alpha}{2\pi}\right] \\ & \times \left\{1 + \frac{23}{18[k_1^{(e)}N_0]^4}\right\} \\ & \times \left(1 + O\left\{\alpha[k_1^{(e)}N_0]^{-4}\right\} + O(\alpha^2)\right). \end{aligned} \quad (41)$$

It should be noted that when evaluating universality couplings, a choice must be made to work on either the $SU(3)_A$ or the $SU(3)_C$ sector. As the Z boson is associated with a nontrivial representation on $SU(3)_A$ but a trivial representation on $SU(3)_C$, it is necessary to work in the $SU(3)_A$ sector. Construction of colour-agnostic composite bosons then implicitly spans all valid preon pairs and hence colour choices, making it unnecessary to independently consider the gluon sector.

c. Gluon sector: There is no gluon coupling equivalent to the scalar coupling of Sec. IV B 2 a, as the Z boson is colourless. Any attempts to construct a coupling to the C sector background will vanish on summation over emission coefficients. The universality coupling also cannot contribute a coupling to the gluon sector, as already discussed.

This completes calculation of Z boson mass to the level of precision employed in this paper.

C. Weak mixing angle

If the weak mixing angle is defined in terms of W and Z boson mass, the above results for m_W^2 and m_Z^2 imply a weak mixing angle

$$\begin{aligned} \sin^2\theta_W = & 1 - \frac{m_W^2}{m_Z^2} \\ = & 1 - \frac{3\left[1 + \left(64 + \frac{3}{2\pi} - f_Z\right)\frac{\alpha}{2\pi}\right]\left\{1 + \frac{19}{18[k_1^{(e)}]^4N_0^4}\right\}}{4\left[1 + \left(\frac{401}{12} + \frac{3}{2\pi}\right)\frac{\alpha}{2\pi}\right]\left\{1 + \frac{23}{18[k_1^{(e)}]^4N_0^4}\right\}} \\ & \times \left(1 + O\left\{\alpha[k_1^{(e)}N_0]^{-4}\right\} + O(\alpha^2)\right) \end{aligned} \quad (42)$$

where f_Z in turn depends on $\sin^2\theta_W$ (17) and it is necessary to solve for consistency. It is worth noting that the corrections described above for the W and Z boson mass diagrams also apply to foreground fermion/weak boson interaction vertices. However, note that for the Z boson, the magnitude of the corrections show some variation between different species, with (for example) the electrons attracting EM loop corrections which are not present for the neutrino. The value obtained for the weak mixing angle will consequently depend on the different weightings given to the various species which may be involved, and thus on the details of individual experiments to measure this parameter. For this reason, the present paper concentrates on particle mass rather than seeking to reproduce experimentally determined values of $\sin^2\theta_W$.

D. Gluon masses

By the unbroken $GL(3, \mathbb{R})$ symmetry of the colour sector, in the e_{ij} basis all gluons have identical mass, and it suffices to calculate the mass of one off-diagonal gluon [though remaining aware that FSF symmetry factors must be computed using a basis of $SU(3)_C \otimes GL(1, \mathbb{R})_N$]. Evaluation of the gluon mass is therefore similar to evaluation of W boson mass, and indeed the lepton/fermion contribution of the leading order diagram and the preon-to-preon gluon loop corrections to this diagram proceed equivalently. Where the W and gluon mass calculations diverge is in the contribution from interactions with the pseudovacuum boson fields. For the W boson this contribution arose from the pseudovacuum photon and scalar boson fields. For the gluons, there are couplings to the pseudovacuum gluon and scalar boson fields.

To evaluate the gluon contribution to the $O(N_0^{-4})$ term, recognise that the preservation of colour cycle invariance across the entirety of the $\mathbb{C}^{\wedge 18}$ analogue model guarantees that all gluons always appear in the context of a superposition of all nine possible species. Interactions with the pseudovacuum need not therefore con-

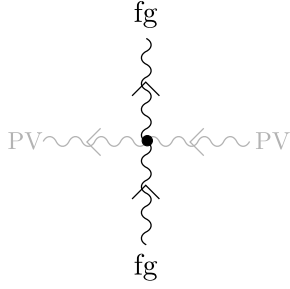


FIG. 12. As the gluon interaction with the background gluon field need not conserve colour on a per-interaction basis, foreground gluons may interact with a pair of background gluons having non-complementary charges.

serve colour charge on an individual gluon on a term-by-term basis provided colour charge is collectively conserved across the superposition. (Individual gluon colour will, however, be preserved on average over length or time scales sufficiently large compared with \mathcal{L}_0 as the pseudovacuum has net trivial colour.) For mass interactions, the consequence of this is that rather than interacting with a single looped boson as per Fig. 10(i), a gluon can interact with a pair of different gluons from the pseudovacuum as per Fig. 12. Furthermore, as noted in Sec. III C 7 of Paper III, unbroken $GL(3, \mathbb{R})$ symmetry implies that background gluon correlators are on average nonvanishing even when different gluons are involved: The gluon field interacts collectively as a single, $GL(3, \mathbb{R})$ -valued species of boson.

To evaluate the background gluon contribution, note:

- This interaction has coefficient f^2 , compared with $f^2/2$ for the photon.
- A diagram in which the two background gluons have different field operators on the vertex, $\varphi^{c_1\dot{c}_1}\varphi^{c_2\dot{c}_2}$, receives a factor of $\frac{1}{2}$ relative to the photon term due to loss of vertex symmetry, but a factor of two as these fields may be pulled down from the generator \mathcal{Z} in either order. A diagram in which the two background gluons have the same field operator attracts neither of these factors.
- Regardless of how the vertex operators are pulled from \mathcal{Z} , each background boson independently ranges over all nine possible species for a factor of 81.

The net contribution to gluon mass from the background gluon field is therefore 81 times larger than the contribution to W boson mass from the background photon field, while the scalar contribution is unchanged. To the same order as used in Eq. (33) above, the gluon mass is

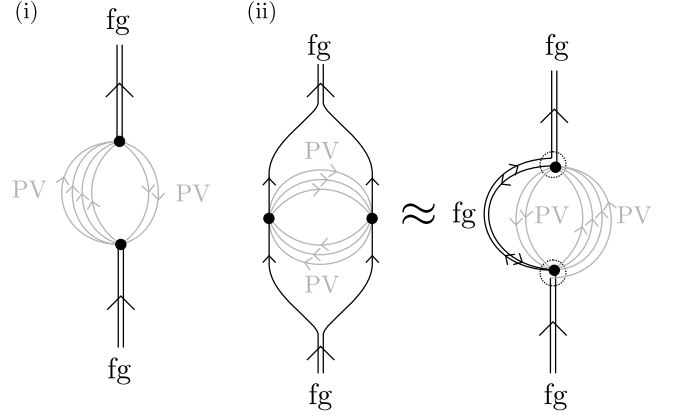


FIG. 13. (i) Leading diagram contributing to scalar boson mass. (ii) First correction.

therefore given by

$$m_c^2 = 9f^2 \left[k_1^{(e)} \right]^4 \omega_0^2 N_0^{12} S_{6,13} \left[1 + \left(64 + \frac{3}{2\pi} - f_Z \right) \frac{\alpha}{2\pi} \right] \times \left\{ 1 + \frac{99}{18 \left[k_1^{(e)} N_0 \right]^4} \right\} \times \left(1 + O \left\{ \alpha \left[k_1^{(e)} N_0 \right]^{-4} \right\} + O(\alpha^2) \right). \quad (44)$$

As noted in Ref. [5], this is a bare mass and will be corrected by self-interaction terms at energy scales small compared with the strong nuclear force, and may anyway be unobservable under normal circumstances as the gluon is confined on a length scale which is small compared with the scale of the mass interaction, $\mathcal{L}_\psi \ll \mathcal{L}_0$.

With regards to additional interaction channels acquired through the universality coupling of Sec. IV A 7, the gluons have nontrivial representation on $SU(3)_C$ and thus this coupling must also be evaluated in the $SU(3)_C$ sector. However, all gluons already couple to all background boson members of this sector, and thus there are no missing couplings to be recovered using this technique. Any attempt to do so would result in double counting, so no further terms are acquired.

This completes calculation of bare gluon mass to the level of precision employed in this paper.

E. Scalar boson mass

As with the W and Z bosons and the gluon, some higher-order corrections to gluon mass are computed here. Recall from Ref. [5] that there are two leading terms in the scalar boson mass interaction, as shown in Fig. 13(i) and (ii), and that these carry relative weights of $[1 - 1/(9N_0)]^2$ and $1/(2\pi)$ respectively.

1. Boson loops

a. Gluon loops: Begin with evaluation of gluon loop corrections to Fig. 13(ii). Recognise that the vertex configuration is identical to that of the Z boson, up to some A -sector labelling. Evaluation of loop corrections proceeds equivalently, including a factor of $\frac{1}{2}$ because interchangeability of boson/pseudovacuum vertices exchanging the preon and antipreon limb of the diagram. The resulting factor is

$$\frac{30\alpha}{2\pi}. \quad (45)$$

For Fig. 13(i), recognise that as discussed in Sec. III 3 of Paper V the pseudovacuum elements being interacted with are still fermions, even though the correlation of background fields over ranges of $O(\mathcal{L}_0)$ permit some of these interactions to take place remotely, creating the appearance of a redistribution of the fermion components. It is the scalar bosons which interact at a distance, as the components of each fermion continue to be bound by colour interactions, and so are separated by at most \mathcal{L}_ψ . (Although the normalisation of Sec. III H 6 of Paper I eliminates these interactions from numerical results, to the extent that the background fields may be represented as particles within their local correlation region it happens that the emergent Lagrangian favours configurations consistent with the same processes as observed in the foreground fields. The constituents of background fermions are consequently still represented as bound species. It is only on leaving the local correlation region that this illusion breaks down due to non-normalisation of the background fields, but can be ignored as this is also the regime in which these uncorrelated fields are cancelled out both among themselves and by other fields also in their far field regime.)

Since the loop corrections take place over distances of $O(\mathcal{L}_\psi)$, at which the loop bosons are massless, these continue to see the preons as being grouped 3+3 rather than 4+2. However, the gluon correction factor is reduced somewhat from $30\alpha/(2\pi)$ because the colour agnosticism of Fig. 13(ii), in which any preon can carry any colour label, is reduced. Two preons in the group of four must necessarily be of the same colour, and as seen in Fig. 5 of Paper V, looking inside the scalar boson/background preons interaction vertex reveals which two preons this is. While the specific colour of the pair is not fixed, the fact that the colours of these two preons are required to be the same reduces the number of degrees of freedom by a factor of 3 per outer vertex compared with Fig. 13(ii). (Or equivalently, only one colour labelling in nine is compatible with the interaction diagram under evaluation.) Diagram (i) therefore only attracts a correction of

$$\frac{30\alpha}{9 \cdot 2\pi}. \quad (46)$$

b. Photon, W , and Z boson loops: Since the scalar boson field couples identically with \bar{e}_R , e_L , and ν_e , the

preon limb of the loop couples to the photon and Z boson fields as per the trace of their representation matrices, which vanish. The contribution of the W boson loop also vanishes as per Sec. IV A 3 above.

c. Scalar boson loops: This time, begin with Fig. 13(i). As in Figs. 8 and 9, scalar boson loops may be constructed on any pair of preons within either the preon limb or the antipreon limb of the fermion loop. Let the scalar boson loop corrections having the form of Fig. 8(i) and Fig. 8(iii)-(vi) be termed scalar boson loops of the first and second kind respectively. Also let the leading-order scalar boson mass diagrams of Figs. 13(i)-(ii) be described as scalar boson mass term 1 and 2. Let the approximate form of term 2 given in Fig. 13(iii) be referred to as term 2'.

1. When a loop of the first kind is applied to term 1, this yields a correction to the mass vertex term obtained from Fig. 13(i). Let this correction be referred to as “item 1”.
2. When a loop of the first kind is applied to term 2, this yields a correction to the mass vertex term obtained from Fig. 13(ii). Let this correction be referred to as “item 2”.
3. When a loop of the second kind is applied to term 1, the result is equivalent to a loop of the first kind applied to term 2'. In particular, note that through the use of preon decomposition, Fierz identities, and F moves [12, 13] the accessory vector boson's vertices (associated with factors of 1) may be taken out to the vertices of Fig. 13(i) permitting transformation from the form of term 2' to that of term 2. There are nine possibilities for the accessory boson, fully offsetting the factor of $\frac{1}{9}$ from loss of colour agnosticism. This diagram is therefore largely equivalent to item 2 (above), though not quite all terms are duplicated due to the factor of $[1 - 1/(9N_0)]^2$ on term 1 from the regrouping of preon lines. Thus this diagram multiplies item 2 by $2[1 - 1/(9N_0)]^2$.
4. When a loop of the second kind is applied to term 2, if the sense of the rotation applied to the loop gluon is chosen counter to that applied in going from term 2 to term 2' then it follows immediately that the induced vector bosons cancel (on appropriate summing across colour labels on both internal and external lines) to yield a loop of the first kind applied to term 1, up to a factor of $2[1 - 1/(9N_0)]^{-2}$ which arises because term 2 has a higher FSF symmetry factor than term 1. Alternatively, if the rotation is chosen such that the rotations do not directly cancel then the same result still follows, essentially from the same isotopy properties as Fig. 16 of Ref. [12].

It therefore suffices to consider only loops of the first kind applied to both diagrams and then multiply by the requisite factors. These loops act on preons in the form of

background fermions, and thus it is simplest to evaluate first for Fig. 13(ii) and then apply the same factor to Fig. 13(i) modulo a factor of $\frac{1}{9}$ for colour knowledge on preon lines as before.

Next, note that the vertices between scalar bosons and fermions, and the vertices between scalar bosons and preons, are all interchangeable (because a coupling with a preon may be written as an average over three couplings with the constituent preons). Not all resulting diagrams yield colour consistency when the scalar boson vertices are combined as per Fig. 9, but for those which do, the resulting symmetry factors are in 1:1 correspondence with the induced overcounting. To obtain the vertex correction factor, it is either necessary to exploit that all diagrams make equal contributions, and offset the average per-diagram overcounting by dividing by the effective vertex interchange symmetry factor, or more simply just to recognise that the resulting cancellation makes it possible to ignore the symmetry factor altogether.

Now proceed to evaluate the scalar boson loop correction to Fig. 13(ii). Apply a loop correction of the first kind as per Fig. 8(i) and combine the vertices as per Fig. 9. Now recognise that at the cost of a braiding factor of -1 , diagrammatic isotopy permits reversal of the inner line of the loop. The resulting vector loop is summed over all A - and C -charges. The nine-element C -sector admits a basis with diagonal elements e_{ii}^C , each of which is averaged over A -charge, so the sum over terms arising from the scalar boson diagram may be rewritten as a sum over gluons.

Evaluating this rewriting:

- Braid factor: -1
- Synthesis of $\sigma^\mu \sigma_\mu$: $-\frac{1}{2}$
- One \mathbf{HH}^* loop yields 81 vector boson terms:

$$\overline{\partial\partial}\varphi\partial\partial\varphi \rightarrow -\frac{1}{2} \sum_{\dot{a}, \dot{c}, a, c} \overline{\partial}^{\dot{a}\dot{c}} \overline{\sigma}_\mu \partial^{ac} \varphi \overline{\partial}^{\dot{a}\dot{c}} \overline{\sigma}^\mu \partial^{ac} \varphi. \quad (47)$$

- However, the scalar boson acts on a single diagram corresponding to an average over colour labelling. A given boson acts on a specific colour labelling, of which there are nine. Thus there is a one in nine chance of any generated gluon being compatible in any given term: $\frac{1}{9}$.
- The gluon correction in Sec. IV E 1 a was evaluated on preons-in-fermions. To raise the current calculation to the fermion level introduces a factor of $\frac{1}{9}$ as each preon/boson vertex is acknowledged to occur only one third of the time in any given fermion vertex, by normalisation of the fermion field (III:28).
- Despite the appearance of Fig. 9, the scalar boson loop does not attract a factor of two for on-vertex symmetry as the underlying construction is as per Fig. 8(i) and coincidence of the vertices only occurs through emergent constraints. It is not a

natural single vertex pulled down as one piece from the generator \mathcal{Z} .

- Note that neither the scalar boson in Fig. 8(i) nor the off-diagonal gluon in Fig. 1(ii) have end-to-end symmetry so there is no need to consider factors of 2 associated with vertex exchange.

Each scalar boson loop correction of the first type therefore maps (numerically) to a gluon loop correction on the same preon pair. It remains a separate correction, as the foreground boson making the loop exists relative to a distinct mass shell solution [14]. The numerical coefficient associated with this mapping is

$$-1 \cdot -\frac{1}{2} \cdot 81 \cdot \frac{1}{9} \cdot \frac{1}{9} = \frac{1}{2}. \quad (48)$$

Then there is the factor of $2[1 - 1/(9N_0)]^2$ from also considering loops of the second kind applied to Fig. 13(i). This yields

$$\frac{30\alpha}{2\pi} \left(1 - \frac{1}{9N_0}\right)^2. \quad (49)$$

Proceeding similarly for loops of the first kind on Fig. 13(i) and loops of the second kind on Fig. 13(ii) yields

$$\frac{30\alpha}{9 \cdot 2\pi} \left(1 - \frac{1}{9N_0}\right)^{-2}. \quad (50)$$

d. Net effect of all boson loops: Incorporating all of the above corrections yields a net mass

$$\begin{aligned} m_{\mathbf{H}}^2 &= 20f^2 \left[k_1^{(e)}\right]^4 \omega_0^2 N_0^{12} S_{6,13} \\ &\times \left\{ \left(1 - \frac{1}{9N_0}\right)^2 \left[1 + \frac{30\alpha}{9\pi} \left(1 + \frac{1}{9N_0}\right)\right] \right. \\ &\quad \left. + \frac{1}{2\pi} \left[1 + \frac{30\alpha}{\pi} \left(1 - \frac{1}{9N_0}\right)\right] \right\} \\ &\times [1 + \mathcal{O}(N_0^{-4}) + \mathcal{O}(\alpha N_0^{-2}) + \mathcal{O}(\alpha^2)]. \end{aligned} \quad (51)$$

By Eq. (V:15) the term in $\mathcal{O}(\alpha N_0^{-2})$ is small compared with $\mathcal{O}(\alpha^2)$ and so may be dropped.

2. Background photon and scalar interactions

a. Direct coupling: All direct boson/boson couplings require nonvanishing matrix commutators on evaluating the boson term of Lagrangian (III:20). However, the scalar boson is associated with the identity matrix on all sectors, and thus any such term must vanish. There are therefore no direct couplings between the complex scalar boson and the background vector or scalar boson fields.

b. Indirect (universality) coupling: Evaluation of this contribution proceeds as in Sec. IV B 2 b. The contributions from e_L and \bar{e}_R have weight 3×3 , those from u_L and \bar{u}_R have weight 2×2 , and those from d_L and \bar{d}_R have weight 1×1 , for a total count of twenty-eight channels. As before, each channel is associated with a relative factor of $[72k_1^{(e)}N_0]^{-4}$ for a net factor of

$$\left\{ 1 + \frac{7}{18 [k_1^{(e)}N_0]^4} \right\} [1 + O(\alpha)] \quad (52)$$

correcting the complex scalar boson mass to

$$\begin{aligned} m_{\mathbf{H}}^2 &= 20f^2 [k_1^{(e)}]^4 \omega_0^2 N_0^{12} S_{6,13} \\ &\times \left\{ \left(1 - \frac{1}{9N_0} \right)^2 \left[1 + \frac{30\alpha}{9\pi} \left(1 + \frac{1}{9N_0} \right) \right] \right. \\ &\quad \left. + \frac{1}{2\pi} \left[1 + \frac{30\alpha}{\pi} \left(1 - \frac{1}{9N_0} \right) \right] \right\} \\ &\times \left\{ 1 + \frac{7}{18 [k_1^{(e)}N_0]^4} \right\} \\ &\times \left(1 + O \left\{ \alpha [k_1^{(e)}N_0]^{-4} \right\} + O(\alpha^2) \right). \end{aligned} \quad (53)$$

This completes calculation of \mathbf{H} boson mass to the level of precision employed in this paper.

F. Neutral boson gravitation

One final note regarding the universality coupling described in Secs. IV B 2 b and IV B 2 b which anticipates the mechanism for $G^{(\dagger)}$ boson elimination in Ref. [9]. Although the Z boson is uncharged, through this process it acquires a means of coupling to the photon *pair* field. This gives the Z boson a means of influencing space-time curvature when the target manifold is made non-flat in Ref. [9], and thus an emergent gravitational mass (though not necessarily one equal to its inertial mass).

The foreground gluons (including the N boson) couple to the colour charges on both the pseudovacuum preon and gluon fields, and application of the universality coupling allows the pseudovacuum preon fields to be reduced to composite vector bosons in 1:1 correspondence with the gluons, so integrating down from background fermions to background bosons does not reveal any new couplings. However, the inclusion of all possible colour couplings implies that a subset of the composite vector boson fields may also be rewritten to correspond to the two-photon coupling (carrying the photon \tilde{a} -charge, and being summed over all possible neutral colour combinations). As this coupling is constructed from the same composite vector boson fields already accounted for, it

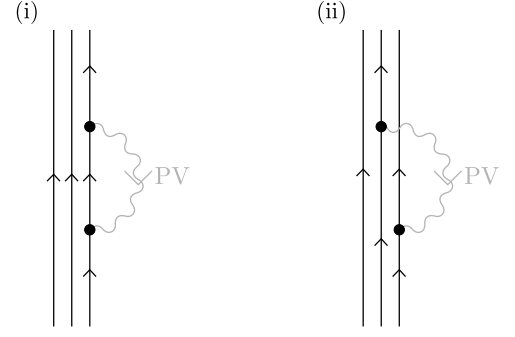


FIG. 14. The fundamental interaction giving rise to lepton mass: The triplet of preons scatters twice off the bosonic component of the background quantum liquid. Either (i) the same, or (ii) different preons may be involved on each occasion, with the upper and lower vertices independently each connecting to any of the three preons. This results in a total of nine diagrams, three having the form of diagram (i) and six having the form of diagram (ii). These nine diagrams are then summed.

makes no additional contribution to inertial mass. However, as it is a coupling to the photon pair field it does also grant gravitational mass to the nine gluon fields. Most notably, this interaction imparts gravitational mass to the N boson, which behaves as a colourless neutral gluon with inertial mass on the electroweak scale. This is therefore a potential dark matter candidate.

V. LEPTON MASS INTERACTION

A. Leading order

The fundamental interaction giving rise to lepton mass is a double scattering of the preon triplet off the vector boson component of the pseudovacuum (Fig. 14). Both of these diagrams may be considered mean field theory expansions of a loop correction to the fermion propagator in the presence of the pseudovacuum, but it is more convenient to refer to these as “leading order” diagrams, and to count the number of (foreground) loop corrections to these leading order diagrams, e.g. 1-loop corrections to the leading order diagram, etc. Henceforth such corrections will be termed simply “1-loop corrections”.

Figure 14 yields a nonvanishing pseudovacuum contribution to fermion mass only when these boson fields are both the boson field or both gluons, as per Eqs. (4–5), and the resulting interactions may each involve any of the three preons making up the lepton. By Eq. (I:169), for the mass contribution to be nonvanishing, the separation of the two boson source/sinks is of order \mathcal{L}_0 .

To evaluate the contribution of the pseudovacuum fields to lepton mass, it is helpful to separate the consequences of these boson interactions into two parts as previously discussed in Paper IV. First, there is the action of the representation matrices of $SU(3)_C$ on the preon

fields, and second, there is the numerical mass term arising from the mean square value of the pseudovacuum boson field.

1. Action on colour sector

To begin with the action of the colour sector, note that over the course of a propagator of length $\mathcal{L} \gg \mathcal{L}_0$, a lepton will engage in a near-arbitrarily large number of interactions with the background fields. Each interaction will apply a $\text{gl}(3, \mathbb{R})_C$ representation matrix from $\{\lambda_i | i \in 1, \dots, 9\}$ depending on the boson species with which the lepton interacts. In the absence of foreground W or Z bosons, the pseudovacuum is made up entirely of photons and gluons.

Given a preon of colour c_1 , this may have nonvanishing interaction with the photon or any of three gluons in the elementary basis e_{ij} . For example, if $c_1 = r$ then admissible gluons are c^{rr} , c^{gr} , and c^{br} . Heuristically, their action on the colour space may be represented as

$$c^{rr}|r\rangle \rightarrow |r\rangle \quad c^{gr}|r\rangle \rightarrow |g\rangle \quad c^{br}|r\rangle \rightarrow |b\rangle \quad (54)$$

where all associated numerical factors have been ignored for illustrative purposes.

More generally, the family of gluons acts on a vector of preon colours as indicated by

$$\begin{pmatrix} c^{rr} & c^{rg} & c^{rb} \\ c^{gr} & c^{gg} & c^{gb} \\ c^{br} & c^{bg} & c^{bb} \end{pmatrix} \begin{pmatrix} |r\rangle \\ |g\rangle \\ |b\rangle \end{pmatrix}. \quad (55)$$

It is worth noting that there is no fixed reference point on the colour sector as the $\text{GL}(3, \mathbb{R})_C$ symmetry is unbroken, so there exists a freedom of basis corresponding to an arbitrary global transformation in $\text{SU}(3)_C$. Any coloured fundamental or composite particle may be put into an arbitrary superposition of colours using such a transformation, though relative colour charges of different particles remain unchanged, as does the magnitude of the overall colour charge of a composite particle.

Recognise now that Fig. 14 contains contributions to two mass vertices. Although their contributions to fermion mass are nonvanishing only when they appear pairwise, there is no requirement for this pair to be consecutive. It suffices that each vertex be paired with a conjugate vertex separated by distance and time no greater than \mathcal{L}_0 in the isotropy frame of the pseudovacuum. Indeed, these vertices are connected by a foreground fermion propagator which in general also undergoes further interactions with the pseudovacuum, represented by using a massive propagator for this fermion and requiring consistency with the outcome of the mass vertex calculation. In general a foreground fermion exhibiting a net propagation over distance or time of $\mathcal{O}(\mathcal{L}_0)$ in the isotropy frame of the pseudovacuum will scatter back and forth multiple times in this process such that

the number of unpaired vertices is assumed negligible. Furthermore, where unpaired vertices do exist, their net effect vanishes on average over probe length or time scales larger than \mathcal{L}_0 . It is therefore reasonable to assume during evaluation that each vertex belongs to a pair.

Counting vertices arising from Fig. 14, for every photon vertex there is also on average one vertex for each of the nine gluons. Across macroscopic length scales, deviations from this average relative frequency will be negligible.

Consider now the specific case of interactions between a propagating lepton and the bosons of the pseudovacuum. Each preon may interact either with a photon or with any of the nine gluons, and the action of the photon on the space of preon colours is trivial, so it is convenient to ignore the photon for now and reintroduce it later.

As already noted, paired interactions with the pseudovacuum gluon field conserve the net colour-neutrality of a leptonic preon triplet. However, overlapping and intercalation of multiple interaction pairs implies that this property only holds on average, as any colour measurement will interrupt a finite number of mass interactions and thus summation to yield no net colour charge on the preon triplet cannot be assured. It is desirable that any measurement of lepton colour should be null, not just the average, and thus a local change of co-ordinates on $\text{SU}(3)_C$ must be performed on a co-ordinate patch encompassing the non-interacting preons such that changes in their colours track those of the interacting preon. This change of co-ordinates is not part of the choice of gauge on $\text{SU}(3)_C$, and thus is in principle associated with construction of some synthetic boson interactions where it intersects with particle worldlines. As described in Sec. III of Paper IV, the vertex factors associated with these interactions arise from the representation matrices of $\text{SU}(3)_C$ given as λ_i in Eqs. (II:38–39). By construction these bosons are constrained to have no effect beyond the colour shifts associated with the boundary of the patch, and to leading order this effect is parameterless. In the leading order diagram these bosons consequently have no degrees of freedom, carry no momentum, and are associated with a numeric factor of 1. Consequently they are not drawn. Only the factors arising from the representation matrices persist, acting on the colour vector of an individual preon as the matrix

$$K_\ell = \begin{pmatrix} 1 & A & A^\dagger \\ A^\dagger & 1 & A \\ A & A^\dagger & 1 \end{pmatrix}, \quad A = \pm \frac{1 \pm i}{2}. \quad (56)$$

The sign on i is free to be chosen by convention, while the overall sign on A is fixed by noting that cyclic permutation of colours, which is in $(K_\ell)^3$, is required to leave the sign of an eigenstate of K_ℓ unchanged. The eigenvalues of K_ℓ must therefore be non-negative, setting

$$A = -\frac{1 \pm i}{2}. \quad (57)$$

Choosing a sign for i , the mixing matrix K_ℓ may then be

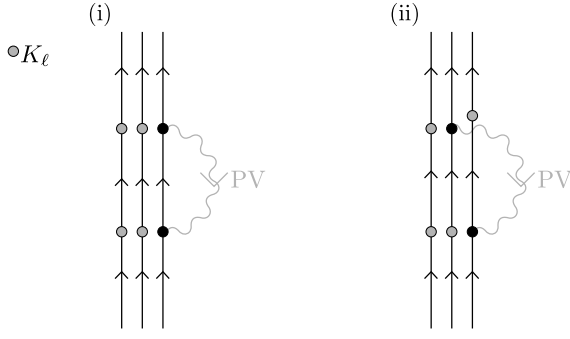


FIG. 15. When a composite fermion interacts with the gluons from the pseudovacuum, represented as a single $\text{gl}(3, \mathbb{R})$ -valued boson, the colour mixing process represented by matrix K_ℓ acts on all preons not coupling to the boson at any given vertex. Diagrams (i) and (ii) correspond to Figs. 14(i)-(ii) respectively. Once again these are just two representative diagrams from a family of nine, as the upper and lower vertices may independently each be connected to any of the three preons. This results in a total of nine diagrams, three having the form of diagram (i) and six having the form of diagram (ii).

written

$$K_\ell(\theta_\ell) = \begin{pmatrix} 1 & \frac{e^{i\theta_\ell}}{\sqrt{2}} & \frac{e^{-i\theta_\ell}}{\sqrt{2}} \\ \frac{e^{-i\theta_\ell}}{\sqrt{2}} & 1 & \frac{e^{i\theta_\ell}}{\sqrt{2}} \\ \frac{e^{i\theta_\ell}}{\sqrt{2}} & \frac{e^{-i\theta_\ell}}{\sqrt{2}} & 1 \end{pmatrix} \quad \theta_\ell = -\frac{3\pi}{4}. \quad (58)$$

As noted in Sec. III of Paper IV, this matrix bears a strong resemblance to Koide's K matrix for leptons [15]. The minus sign on Koide's off-diagonal component $S(\theta_f)$ has been absorbed into the phase θ_ℓ , and the free parameters a_f , b_f , and θ_f are fixed by the geometry of the model, in keeping with the predictive capacity of the $\mathbb{C}^{\wedge 18}$ dust gravity.

Recognising that on average all pseudovacuum gluons act identically and with equal frequency, it is convenient to collect these together into a single $\text{gl}(3, \mathbb{R})$ -valued gluon associated with two applications of matrix K_ℓ to the non-interacting preons, as shown in Fig. 15.

Now recognise that since the gluons of the $\mathbb{C}^{\wedge 18}$ model are massive, and since the fundamental mass interactions take the form of loop diagrams with respect to the lepton propagator (Fig. 14), these will be suppressed by a factor of $O(m_\ell^2/m_c^2)$ relative to the photon contribution. [In practice no single gluon will propagate a distance of $O(\mathcal{L}_0)$ due to confinement binding it tightly to the emitting lepton, but it is also unnecessary that any single gluon should do so—instead, for gluons the line in Fig. 14 represents the propagation of momentum carried in a distributed fashion within the gluon cloud accompanying the lepton. This propagating momentum carried in the gluon sector then necessarily displays an effective mass shell behaviour consistent with m_c^2 .] With each gluon interacting, on average, once for every photon interaction, it is convenient to write the direct contributions of the gluon terms to particle mass as corrections to the larger

photon term and to associate copies of the matrix K_ℓ with the photon vertices in a manner equivalent to that shown in Fig. 15 and discussed in Sec. III B 2 of Paper IV.

Next, consider that the preons on which matrix K_ℓ are acting are just two of three preons in a colour-neutral triplet. For leptons, all three a -charges are identical and thus over macroscopic scales, where chance fluctuations become negligible, matrix K_ℓ will act identically on each member of the triplet. This symmetry is convenient, as it allows the study of an individual preon prior to the reconstruction of the triplet as a whole.

As per Eq. (6), the preons making up observable leptons are now eigenstates of this matrix K_ℓ , corresponding to the eigenvectors

$$v_1 = \frac{1}{\sqrt{3}} \begin{pmatrix} 1 \\ 1 \\ 1 \end{pmatrix} \quad (59)$$

$$v_2 = \frac{1}{\sqrt{3}} \begin{pmatrix} e^{\frac{\pi i}{3}} \\ e^{-\frac{\pi i}{3}} \\ -1 \end{pmatrix} \quad (60)$$

$$v_3 = \frac{1}{\sqrt{3}} \begin{pmatrix} e^{\frac{2\pi i}{3}} \\ e^{-\frac{2\pi i}{3}} \\ 1 \end{pmatrix} \quad (61)$$

which are independent of θ_ℓ and have eigenvalues $\{k_i^{(\ell)} | i \in \{1, 2, 3\}\}$ given by

$$k_n^{(\ell)} = 1 + \sqrt{2} \cos \left[\theta_\ell - \frac{2\pi(n-1)}{3} \right]. \quad (62)$$

To reconstruct the lepton as a whole, recognise that for three preons at $\{x_i | i \in \{1, 2, 3\}\}$, with corresponding colours c_i , and with the preon at x_1 having a well-defined color, say $c_1 = r$, colour neutrality and colour cycle invariance imply that a choice $c_2 = g$, $c_3 = b$ is equal up to a sign to the alternative choice $c_2 = b$, $c_3 = g$ (as this exchange corresponds to spatial exchange of two fermions), and thus it suffices to consider only one such colour assignment (say $c_2 = g$, $c_3 = b$) along with spatial permutations. Putting preon 1 into a superposition of colour states then corresponds to a superposition of cyclic spatial rearrangements of the members of the triplet, with colours $c_1 = r$, $c_1 = g$, and $c_1 = b$ corresponding to colour assignments *with respect to spatial co-ordinate* x of rgb , gbr , and brg respectively. It follows that for leptons, the different spatial configurations of colours on the preon triplet are eigenvectors of a matrix $K_\ell^{(3)}$ with eigenvalues identical to those of K_ℓ .

Having established through colour cycle invariance that the matrix K_ℓ acts identically on all constituents of a lepton, and through Fig. 15 that two copies of K_ℓ act per pseudovacuum photon interaction, it follows that the effect of matrix K_ℓ is to contribute a factor of $[k_i^{(\ell)}]^2$ to the mass of a lepton of generation i . It might seem

problematic that for $\theta_\ell = -3\pi/4$, $k_1^{(\ell)} = 0$, but it will be seen in Sec. V C that θ_ℓ acquires corrections from higher-order diagrams, resulting in $k_i > 0 \forall i$, so $k_1^{(\ell)}$ may be assumed real and positive, and this concern may be disregarded.

2. Mass from photon and gluon components of the pseudovacuum

The zeroth-order electromagnetic term is readily evaluated by making a mean-field substitution (4) for $[A^\mu(x)A_\mu(y)]_{\text{bg}}$. For a charged lepton ℓ_i of generation i , this initial approximation may be written

$$m_{\ell_i}^2 = \frac{f^2}{2} [k_i^{(\ell)}]^4 \omega_0^2 N_0^8 S_{18,147} [1 + \mathcal{O}(\alpha)] \quad (63)$$

as seen in Paper IV. Note that this expression incorporates a symmetry factor of two corresponding to exchange of the two pseudovacuum interactions. This may be understood by recognising that each term corresponds to a mass vertex and has its external legs truncated independently. These two vertices are then interchangeable for a symmetry factor of 2. Alternatively, for any diagram, including ones which do not separate, recognise that the mass-squared is always applied in the context of an untruncated fermion propagator, say from x to y . In this context, all fermion connections to the interaction vertices are again untruncated. (Optionally, the full expression for propagation from x to y is then used to infer an equivalent mass term, and the diagram may then be replaced by one in which this mass term is inserted into the propagator twice.) Applying either form of this approach to Fig. 14, the diagram for propagation between two points is again seen to attract a symmetry factor of 2.

Now consider interactions between a foreground fermion and the pseudovacuum gluon fields. As with the photon, these interactions take the form of loop diagrams evaluated in the mean-field regime for the pseudovacuum, and as noted in Sec. III B 1 of Paper IV, the fermion may transiently surrender momentum to or borrow momentum from the background fields. However, in contrast with the photon loop evaluated to obtain Eq. (63), the gluon field is massive, and when a foreground particle transfers momentum to a gluon field, this results in a massive excitation of that gluon field. Consequently both limbs of the loop must be considered massive. For a general boson b this gives rise to a loop-associated factor of $\mathbf{f}(m_{\ell_i}^2/m_b^2)$. This factor vanishes for the photon, as it is massless, but not for interactions with the background gluon field.

For both the photon loop and the gluon loop, evaluation of momentum flux around the loop may be taken to yield a factor of

$$\frac{\Xi}{4\pi} \mathbf{f}\left(\frac{m_{\ell_i}^2}{m_b^2}\right), \quad b \in \{A, c\} \quad (64)$$

for some structure factor Ξ , where $\mathbf{f}(n)$ behaves as described in Appendix A. For the photon $\Xi = 2\alpha$ and the factor $\mathbf{f}(\cdot)$ reduces to 1, and the resulting coefficient of $\alpha/(2\pi)$ is absorbed into the pseudovacuum mean-field term by choice of definition. For gluons, dependence on the same energy scale \mathcal{E}_0 indicates that an identical factor of $\alpha/(2\pi)$ is absorbed into the mean field term, while the mass dependence of $\mathbf{f}(\cdot)$ reveals that the gluon terms are suppressed by a factor of $m_{\ell_i}^2/m_c^2$ relative to the photon term. [Although the transmission of the foreground momentum around the gluon loop is massive, the factor arising from $\mathbf{f}(\cdot)$ is $m_{\ell_i}^2/m_c^2$ and not $m_{\ell_i}^2/(4\pi m_c^2)$ as the value of the gluon loop diagram is dominated by the background terms. This is discussed further in Appendix A.]

To determine the structure factor of the gluon diagram, work in the e_{ij}^C basis, and consider first a specific off-diagonal gluon. As discussed in Sec. III E 8 of Paper III and Sec. IV A 2 above, mapping to the one- W -loop correction to lepton magnetic moment (12) permits the magnitude of the structure factor to be evaluated as $\frac{10\alpha}{3} [1 + \mathcal{O}(\alpha)]$. In comparison with the reference process, however, there is no emitted boson in Fig. 15. The sign of the structure factor may then be easily determined by recognising that on mapping Fig. 15 to a tensor network [16–18] the resulting network is a perfect square and thus the structure factor must be real and positive. For a diagonal gluon e_{ii}^C the calculation is modified as there is only one possible colour, not two, on the target preon (it is the same as the source preon) but this is offset by a factor of two for vertex interchange symmetry so the result is the same.

There is, however, a further correction to the above. In Sec. IV A 2, gluon exchange was restricted by the requirement of colour neutrality on the inbound and outbound triplets. In the present situation the gluon at each vertex represents the c_{μ}^{ij} component of the colour mixing operator \hat{K}_{μ} (IV:25), and overall colour neutrality is conserved by the requirement that free fermions be colour-neutral eigenstates of the matrix $K_e(\mathcal{E})$. Further, since the gluons at the vertices arise from the background fields, by Eq. (5) they need not be conjugate to yield a non-vanishing diagram. Momentum transfer through the background field channel may still take place, due to the on-average independent separate conservation of foreground and background momenta, and may be assumed to do so through implicit scattering processes in the background fields. (As noted previously, although the normalisation of Sec. III H 6 of Paper I eliminates contributions of these interactions to numerical results, they may still be considered to occur within the local correlation region.) This lack of conjugacy corresponds to reopening the loop of Fig. 15 to recover a diagram more akin to Fig. 1 of Paper IV, much as Fig. 12 is an opening of the loop on Fig. 10(i), and increases the number of admissible gluon colours by a factor of 3. Overall, the

resulting structure factor is

$$\frac{10\alpha}{3} [1 + O(\alpha)] \cdot 3 \cdot \mathbf{f}\left(\frac{m_{\ell_i}^2}{m_c^2}\right) \cdot \frac{1}{4\pi}, \quad (65)$$

and for background gluon fields

$$\mathbf{f}\left(\frac{m_{\ell_i}^2}{m_c^2}\right) \rightarrow \frac{m_{\ell_i}^2}{m_c^2}, \quad (66)$$

giving a net relative factor of

$$\frac{5m_{\ell_i}^2}{m_c^2} [1 + O(\alpha)]. \quad (67)$$

The terms denoted $O(\alpha)$ reflect potential discrepancies in the one-photon-loop corrections to the photon and gluon leading-order diagrams. However, with these corrections not yet having been calculated for either diagram it is convenient to write just the leading global correction to $m_{\ell_i}^2$ as a whole. Taking both photon and gluon terms into account (but not yet including the scalar boson contribution, denoted \dots), the leading-order expression for lepton mass is therefore given by

$$m_{\ell_i}^2 = \frac{f^2}{2} [k_i^{(\ell)}]^4 \omega_0^2 N_0^8 S_{18,147} \times \left\{ \frac{q_\ell^2}{e^2} + \frac{5m_{\ell_i}^2}{m_c^2} + \dots \right\} [1 + O(\alpha)] \quad (68)$$

where q_ℓ is the charge of lepton ℓ_i .

As an aside, note that for the fermions there is no equivalent to the bosonic universality coupling explored in Sec. IV B 2 b. For the Z boson, this coupling arises as the basic Z mass diagram [equivalent to Fig. 1(i)] intrinsically incorporates six background preon lines, and two co-ordinates to integrate over, permitting reduction to two preon lines when one of these integrals is performed. In contrast, the basic fermion mass diagram (Fig. 15) contains no intrinsic mechanism for adding extra preon lines. Although extra preons may be recruited from the pseudovacuum, consistent normalisation (Sec. III H 6 of Paper I) requires that integrating over the additional co-ordinate thus introduced will inevitably eliminate them again.

3. Mass from scalar component of the pseudovacuum

Next to be considered is the interaction between the composite lepton and the pseudovacuum complex scalar boson field shown in Fig. 16. Again it is desirable to write this term as a correction to the photon term. As per Eq. (7) the pseudovacuum expectation value of the complex scalar boson field is nonvanishing, and evaluation of the associated loop factor is most readily performed by determining its weight relative to the photon diagram.

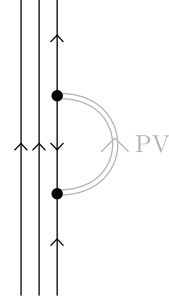


FIG. 16. Leading-order contribution to fermion mass from the background scalar field.

To achieve this, let the $SU(3)_A$ sector be supplemented by the N boson to obtain the Lie algebra $\mathfrak{gl}(3, \mathbb{R})_A$ of an effective symmetry group $GL(3, \mathbb{R})_A$. Adopt a basis e_{ij}^A . Decomposing the scalar boson into its terms, the loop associated with each term will now be mapped to an equivalent loop involving a vector boson e_{ij}^A . Note, however, that this is just a numerical equivalence used to determine relative loop weights. The actual evaluation of the pseudovacuum term is performed on the complex scalar boson itself, which has trivial C -sector and A -sector representation and as discussed in Sec. III C 7 of Paper III this is consequently unaffected by the $SU(3)_A$ and $SU(3)_C$ gauge choices presented in Sec. III C 6 of Paper III.

To determine the loop weight, first recognise that each basis element in e_{ij}^A is averaged over colour. The terms in $\mathbf{H}\mathbf{H}^*$ are summed over A -charge and colour, with the result that the terms are equivalent (up to factors to be determined) to a sum over the diagonal bosons e_{ii}^A , each multiplied by three to go from an average over colour to a sum.

Now exploit the $GL(3, \mathbb{R})$ -invariance of the e_{ij}^A representation of $\mathfrak{gl}(3, \mathbb{R})_A$ by noting that the structure factor associated with an diagonal element e_{ii}^A will be the same as that associated with an off-diagonal element $e_{ij}^A|_{i \neq j}$. Therefore begin from the structure factor for the W boson, and multiply by appropriate coefficients to construct the relevant factor for the complex scalar boson. Relevant factors are as follows:

- Structure factor: $-\frac{10}{3} [1 + O(\alpha)]$ for W , 2 for photon. Relative factor: $-\frac{5}{3} [1 + O(\alpha)]$.
- Elimination of sigma matrices from W diagram when mapping to a scalar boson term: -2 .
- The W boson diagram maps to $\frac{1}{9}$ of the \mathbf{H} diagram: $\frac{1}{9}$.
- There are nine such terms: 9
- As described in Sec. III E 5 of Paper III the \mathbf{H} and \mathbf{H}^* vertices are constructed in the “far field” and thus their emission from the fermion attracts a factor of $2N_0^{-2} [1 + O(N_0^{-1})]$ apiece.

- As per the caption of Fig. 6 of Paper III, there are two different ways to assemble the complex scalar boson and conjugate from constituent preons, but these are subsumed into a definition of the complex scalar boson field and thus do not introduce any factors.
- The complex scalar boson is massive, for a factor of $\mathbf{f}(m_{\ell_i}^2/m_{\mathbf{H}}^2)$.
- It is not associated with K_ℓ matrices, for a factor of $[k_i^{(\ell)}]^{-4}$.

On comparing the scalar boson diagram with the vector boson diagram, the net relative factor is thus

$$\begin{aligned}
 & -\frac{5}{3} [1 + \mathcal{O}(\alpha)] \cdot -2 \cdot \frac{1}{9} \cdot 9 \cdot \left[\frac{2}{N_0^2} \right]^2 [1 + \mathcal{O}(N_0^{-1})] \\
 & \times \mathbf{f} \left(\frac{m_{\ell_i}^2}{m_{\mathbf{H}}^2} \right) \cdot [k_1^{(\ell)}]^{-4} \\
 & = \frac{40m_{\ell_i}^2}{3m_{\mathbf{H}}^2 [k_1^{(\ell)} N_0]^4} [1 + \mathcal{O}(N_0^{-1}) + \mathcal{O}(\alpha)]
 \end{aligned} \tag{69}$$

for a total lepton mass

$$\begin{aligned}
 m_{\ell_i}^2 &= \frac{f^2}{2} [k_i^{(\ell)}]^4 \omega_0^2 N_0^8 S_{18,147} \\
 & \times \left\{ \frac{q_\ell^2}{e^2} + \frac{5m_{\ell_i}^2}{m_c^2} + \frac{40m_{\ell_i}^2}{3m_{\mathbf{H}}^2 [k_i^{(\ell)} N_0]^4} [1 + \mathcal{O}(N_0^{-1})] \right\} \\
 & \times [1 + \mathcal{O}(\alpha)].
 \end{aligned} \tag{70}$$

4. Gluon and scalar field mass deficits

Conservation of energy/momentum implies that the rest mass imparted to the fermion must be compensated by a reduction in the zeroth component of 4-momentum of some of the pseudovacuum fields. Likelihood of contribution from any given pseudovacuum sector will be governed by availability of zeroth-component energy within that sector, i.e. the rest mass of the associated species, and the strength of coupling to that sector. It therefore follows that this borrowing of rest mass occurs with equal likelihood from each of the nine gluon channels of the pseudovacuum, with much lower likelihood from the scalar boson channel (due to a much weaker coupling), and not at all from the photon channel (due to zero rest mass). For a first approximation, consider only the gluon channel. Borrowing a mass of m_*^2 from a background gluon field takes place at the first of the existing gluon/fermion interaction vertices of Fig. 14, and corresponds to deletion of a gluon of mass m_* from the pseudovacuum. This hole then propagates as a quasiparticle, and is filled by the conjugate interaction at the second vertex.

More generally, with multiple overlapping pairs of background gluon field interactions occurring along a fermion propagator, there is a consistent propagating hole in the pseudovacuum gluon sector corresponding to an energy deficit of m_*c^2 , and individual vertices may cause transient fluctuations and may change which specific gluon fields (with respect to some arbitrary choice of colour basis) are involved in propagating this hole, but in general it may be in any of the nine gluon channels at any time. This hole is in addition to the effect discussed in Sec. V A 2 where fermions may surrender momentum to or borrow momentum from the pseudovacuum, and thus gives an additional correction factor not yet discussed.

This hole propagates as a quasiparticle accompanying the lepton. Any time that a fermion interacts with the pseudovacuum gluon sector this hole is necessarily also present, and may occupy any of nine channels.

For simplicity, further consider the case when the hole occupies an off-diagonal channel. It would be convenient to write the effect of this hole as a correction to the mass of gluon,

$$m_c^2 \longrightarrow m_c^2 - km_*^2 =: (m_c^*)^2 \tag{71}$$

for some factor k . Recognising that the co-propagating hole's interaction with the fermion is trivial (it is only required to be present), with any local energy/momentum transfer to or from the pseudovacuum being mediated by the fermion/gluon coupling of Fig. 14(i), the hole's interactions attract no structural vertex factor and thus where the direct gluon interactions of Fig. 14(i) acquire a factor of 5/3 apiece, the hole does not, for an effective relative factor of 3/5 on the hole's interactions. Further, the presence of the hole breaks the time reversal symmetry of a portion of the pseudovacuum and this gives rise to a symmetry factor of $\frac{1}{2}$ relative to the original gluon interaction in which the pseudovacuum was assumed time-reversal-invariant. Finally, there are nine gluons, and by $\text{GL}(3, \mathbb{R})$ symmetry the mass deficit may propagate via any of them with equal likelihood and equivalent consequence. The multiplicative factor obtained assuming a single channel of propagation for the mass deficit is therefore increased ninefold. The net outcome is to correct the gluon mass to an effective mass of

$$\begin{aligned}
 (m_c^*)^2 &= m_c^2 - \frac{3}{5} \cdot \frac{1}{2} \cdot 9 \cdot m_*^2 \\
 &= m_c^2 \left(1 - \frac{27}{10} \frac{m_*^2}{m_c^2} \right).
 \end{aligned} \tag{72}$$

Note that m_c^* is a function of m_* , but for a lepton ℓ_i which is on-shell and at (or close to) rest in the isotropy frame of the pseudovacuum this admits the convenient replacement $m_*^2 \rightarrow m_{\ell_i}^2$. Also note that the gluon mass deficit effect is a whole-field effect, acting on both the foreground and background gluon fields. The corrected gluon mass m_c^* should be used anywhere a particle interacts with a gluon field in the presence of a lepton.

Similarly, the foreground lepton may also borrow its mass from the scalar boson field. However, coupling

between leptons and scalar bosons is weaker than that between leptons and gluons. Much as the gluon deficit corrects m_c^2 by $O(m_{\ell_i}^2/m_c^2)$ in expressions for particle rest mass, the scalar mass deficit corrects m_H^2 by $O(m_{\ell_i}^2/m_H^2)$. Including this as an unevaluated higher-order term, the lepton mass equation is amended to

$$m_{\ell_i}^2 = \frac{f^2}{2} [k_i^{(\ell)}]^4 \omega_0^2 N_0^8 S_{18,147} \quad (73)$$

$$\times \left\{ \frac{q_\ell^2}{e^2} + \frac{5m_{\ell_i}^2}{(m_c^*)^2} + \frac{40m_{\ell_i}^2}{3m_H^2 [k_i^{(\ell)} N_0]^4} \right. \\ \left. \times \left[1 + O(N_0^{-1}) + O\left(\frac{m_{\ell_i}^2}{m_H^2}\right) \right] \right\} [1 + O(\alpha)] \\ (m_c^*)^2 = m_c^2 \left(1 - \frac{27m_{\ell_i}^2}{10m_c^2} \right). \quad (74)$$

B. Foreground loop corrections

Now consider the effects of foreground loop corrections on the leading-order diagrams of Figs. 14 and 16. Note that since momentum is continually redistributed among the constituent preons by means of gluon-mediated interactions even over length scale \mathcal{L}_ψ , a boson need not start and finish its trajectory on the same preon in order to be considered a loop correction to an emission vertex. Further note that the massive nature of the loop boson does not disrupt the pseudovacuum correlators in these diagrams, as these are brought together through the use of spinor identities at the vertices making these diagrams more robust against interference from intermediate particles propagating outside the autocorrelation region than the boson mass diagrams of Sec. IV.

1. 1-loop EM corrections

The $O(\alpha)$ EM loop corrections to the lepton mass interaction are shown in Fig. 17. These should be compared with their Standard Model counterparts in Fig. 18.

As in Sec. IV A 1, the only corrections which need to be incorporated into the electron mass vertex are those which do not also appear in the Standard Model. Further, as per Sec. III A of Paper IV all PSE terms may be absorbed into the fundamental vertex prior to applying non-PSE corrections. Begin with the diagrams of Fig. 17(i), which have the Standard Model counterparts shown in Fig. 18. Evaluation of symmetry factors is described in Appendix B and reveals these to be directly equivalent. The diagrams of Fig. 17(i) therefore correspond to PSE vertex corrections in the Standard Model. Provided the mass vertex after all non-PSE corrections is identified with the observable mass, in keeping with emulation of the $\overline{\text{MS}}$ renormalisation scheme, the diagrams of Fig. 17(i) therefore make no contribution to $m_{\ell_i}^2$.

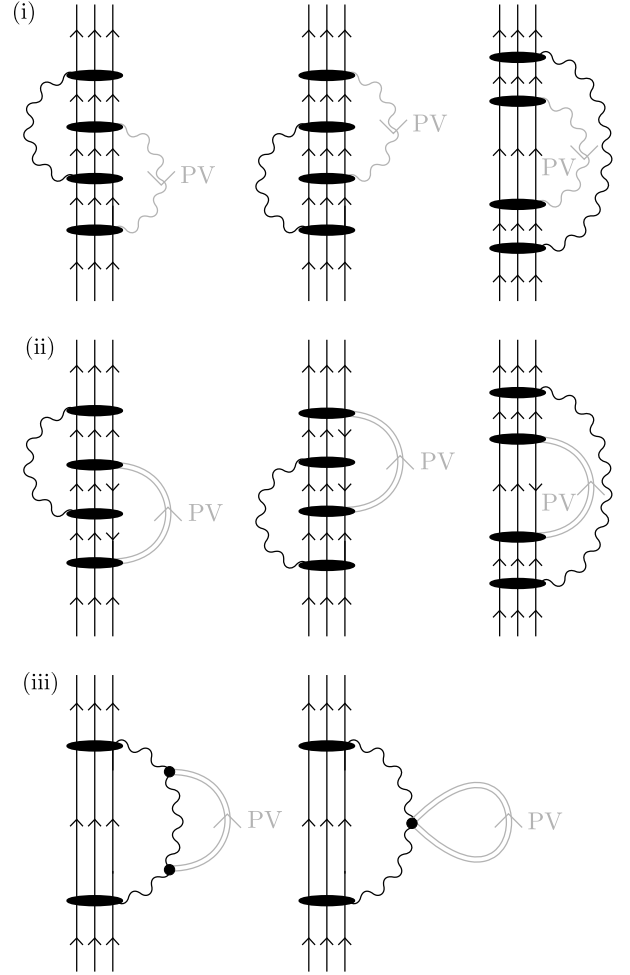


FIG. 17. One-foreground-loop EM corrections to (i) vector boson and (ii)-(iii) scalar boson lepton mass interactions. The broad oval interaction vertices indicate that the boson may interact with any of the three preons, and all configurations should be summed over.

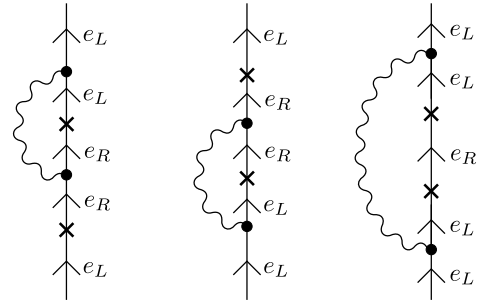


FIG. 18. Standard Model one-foreground-loop EM corrections to the electron mass vertex. The example shown is for the left-helicity electron Weyl spinor; equivalent diagrams for the right-helicity spinor exchange L and R .

It is complementary to note that when multiple photon loops exist, the summation over different pseudovacuum expansions of a diagram is equivalent to treating the background photon loop as being of a unique species distinguishable from any foreground photon loops, then summing over the contributions of the resulting effectively topologically distinct diagrams. Since the background loop thus behaves as a distinct species, the EM loop corrections to the background photon interaction are identical to the EM corrections to the background gluon interaction and do not attract additional symmetry factors on account of the foreground and background interactions both being photon interactions. Thus there are no relative terms of $O(\alpha)$ on $5m_{\ell_i}^2/(m_c^*)^2$.

Next, consider the scalar boson loops of Fig. 17(ii). In these diagrams the intermediate lepton has one preon reversed, inverting its electromagnetic charge, and the first two diagrams therefore yield factors of $\alpha/(6\pi)$ rather than $\alpha/(2\pi)$. In conjunction with negation of the Standard Model corrections, they therefore yield a net correction to the background scalar term with weight

$$-\frac{2\alpha q_\ell^2}{3\pi e^2}. \quad (75)$$

The third diagram is consistent with the Standard Model equivalent and so once again does not contribute to m_{ℓ_i} .

Finally, there are two more diagrams from the scalar boson sector to consider. Moving a single scalar boson vertex onto the photon loop is prohibited as the diagram as a whole does not then leave the preon triplet unchanged (one preon gets replaced by an antipreon), but moving both vertices onto the loop is admissible. This results in the diagrams shown in Fig. 17(iii). However, these loops contribute to the mass of the loop photon (which vanishes by gauge), and thus will necessarily cancel with other terms in which the loop photon couples to the background fields. They may therefore be disregarded. The net expression for lepton mass thus far derived is therefore

$$\begin{aligned} m_{\ell_i}^2 = & \frac{f^2}{2} \left[k_i^{(\ell)} \right]^4 \omega_0^2 N_0^8 S_{18,147} \\ & \times \left\{ \frac{q_\ell^2}{e^2} + \frac{5m_{\ell_i}^2}{(m_c^*)^2} + \frac{40m_{\ell_i}^2}{3m_{\mathbf{H}}^2 \left[k_i^{(\ell)} N_0 \right]^4} \left(1 - \frac{2\alpha q_\ell^2}{3\pi e^2} \right) \right. \\ & \times \left[1 + O(N_0^{-1}) + O\left(\frac{m_{\ell_i}^2}{m_{\mathbf{H}}^2} \right) + O(\alpha^2) \right] \left. \right\} \\ & \times (1 + \dots) \end{aligned} \quad (76)$$

where “...” represents massive loop corrections of order α which are derived next.

For a further amendment to this expression, also note that the extra photon making up the loop may potentially comprise some of the same preons as are involved in interactions elsewhere within the local correlation region, with effect on the FSF symmetry factors associated with the loop photon vertices. The resulting

corrections comprise both massless and massive terms. All relevant boson masses are of comparable magnitude, $m_c^2 \sim m_W^2 \sim m_Z^2 \sim m_{\mathbf{H}}^2$, and gluon terms will be seen to outweigh weak sector terms, therefore write the leading elements of each term correcting m_{e_i} as $O(\alpha N_0^{-1})$ and $O[\alpha N_0^{-1} m_{e_i}^2/(m_c^*)^2]$ respectively. Neither of these corrections have counterparts in the Standard Model. It is convenient to insert them into the final bracket of the above expression,

$$(1 + \dots) \longrightarrow \left\{ 1 + O\left(\frac{\alpha}{N_0} \right) + O\left[\frac{\alpha m_{e_i}^2}{N_0 (m_c^*)^2} \right] + \dots \right\} \quad (77)$$

2. $O(N_0^{-1})$ corrections to 1-loop EM corrections

It is relatively straightforward to calculate the $O(N_0^{-1})$ corrections to the 1-loop EM corrections, as presented here. First, recognise that these corrections only apply when a loop vertex is within the same correlation region as another vertex. If not, then only the usual EM symmetry factor of S_α applies, which is incorporated within the coefficient α associated with the loop vertices.

However, consider the first diagram of Fig. 17(i), in which the lower vertex on the foreground photon is bracketed by two correlated couplings to the pseudovacuum. Assuming the window approximation (I:169), in the isotropy frame of the pseudovacuum these bracketing vertices must lie within the autocorrelation distance and time of one another. In the dominant (on-shell) contribution, propagation from one vertex to the other is linear and hence the lower vertex of the foreground photon also lies within the same correlation region.

To evaluate the mean contribution of the associated symmetry factors, first recognise that within a given foreground vertex there are two inbound preon lines and two outbound preon lines. It suffices to consider each separately.

Recognising that all preon lines undergo interactions with the background fields which may cause them to change colour, and that colour is only conserved separately within the foreground and background fields on average over scales large compared with \mathcal{L}_0 , the colour of each inbound or outbound line both in this vertex and in the background field interaction vertices may be considered independently random. Thus there is a chance of $\frac{1}{3}$ that the colour of a given line at the foreground vertex will match the equivalent line at a given background field vertex.

In contrast, A -charge is guaranteed to match as all photons arise from the same fermion, which contains only one type of preon carrying a well-defined A -charge. However, these fermions emit bosons associated with representations containing both $\delta_{\bar{c}c} \bar{\psi}^{1\bar{c}} \bar{\sigma}^\mu \psi^{1c} - \delta_{\bar{c}'c'} \bar{\psi}^{2\bar{c}'} \bar{\sigma}^\mu \psi^{2c'}$ and $\delta_{\bar{c}c} \bar{\psi}^{1\bar{c}} \bar{\sigma}^\mu \psi^{1c} + \delta_{\bar{c}'c'} \bar{\psi}^{2\bar{c}'} \bar{\sigma}^\mu \psi^{2c'}$, with the former corresponding to photons and the latter to Z and N bosons.

By conservation of charge at vertices, and the requirement that the fermion line carries a well-defined A -charge, these two groups are emitted with equal weight. Consequently, when there is a match of A -charges at two vertices, there is only a 50% chance that the line being matched in the e_{ij} basis corresponds to a photon. Thus the A sector provides a further factor of $\frac{1}{2}$.

There are four lines at the foreground vertex which is in the correlated region, and there are two background vertices with which to seek symmetry matches. The odds per line per vertex are $\frac{1}{3} \cdot \frac{1}{2}$, with each match increasing a symmetry factor of $O(N_0)$ by 1, for a net relative factor from all lines and vertices of

$$\left(1 + \frac{4}{3N_0}\right). \quad (78)$$

A similar analysis applies to the second diagram of Fig. 17(i) but not to the third, yielding an overall loop correction factor to the tree level vertex, accurate to $O(\alpha N_0^{-1})$, of

$$\begin{aligned} & \left[1 + \frac{\alpha}{2\pi} \left(1 + \frac{4}{3N_0}\right) + \frac{\alpha}{2\pi} \left(1 + \frac{4}{3N_0}\right) + \frac{\alpha}{2\pi} \right. \\ & \quad \left. + O\left(\frac{\alpha}{N_0^2}\right) + O(\alpha^2)\right] \\ & = \left[1 + \frac{3\alpha}{2\pi} \left(1 + \frac{8}{9N_0}\right) + O\left(\frac{\alpha}{N_0^2}\right) + O(\alpha^2)\right]. \end{aligned} \quad (79)$$

This is compared with the Standard Model factor of $3\alpha/(2\pi) + O(\alpha^2)$ to yield a correction factor accurate to $O(N_0^{-1})$ and $O(\alpha)$ of

$$C_{\alpha, N_0} := \frac{1 + \frac{3\alpha}{2\pi} \left(1 + \frac{8}{9N_0}\right)}{1 + \frac{3\alpha}{2\pi}}, \quad (80)$$

and a net expression for electron mass

$$\begin{aligned} m_{\ell_i}^2 &= \frac{f^2}{2} \left[k_i^{(\ell)}\right]^4 \omega_0^2 N_0^8 S_{18,147} C_{\alpha, N_0} \\ & \times \left\{ \frac{q_\ell^2}{e^2} + \frac{5m_{\ell_i}^2}{(m_c^*)^2} + \frac{40m_{\ell_i}^2}{3m_{\mathbf{H}}^2 \left[k_i^{(\ell)} N_0\right]^4} \left(1 - \frac{2\alpha q_\ell^2}{3\pi e^2}\right) \right. \\ & \quad \times \left[1 + O(N_0^{-1}) + O\left(\frac{m_{\ell_i}^2}{m_{\mathbf{H}}^2}\right) + O(\alpha^2)\right] \Big\} \\ & \times \left\{1 + O\left(\frac{\alpha}{N_0^2}\right) + O\left(\frac{\alpha^2}{N_0}\right) + O\left[\frac{\alpha m_{e_i}^2}{N_0(m_c^*)^2}\right] + \dots \right\} \end{aligned} \quad (81)$$

where the correction of $O(\alpha/N_0)$ in Eq. (77) has been evaluated to yield C_{α, N_0} , and the next-highest unevaluated contributions are $O(\alpha/N_0^2) + O(\alpha^2/N_0)$. [As with corrections of $O(\alpha)$, corrections of $O(\alpha^2)$ are common to both the $\mathbb{C}^{\wedge 18}$ model and the Standard Model and thus do not need to be incorporated into the expression for the mass vertex.]

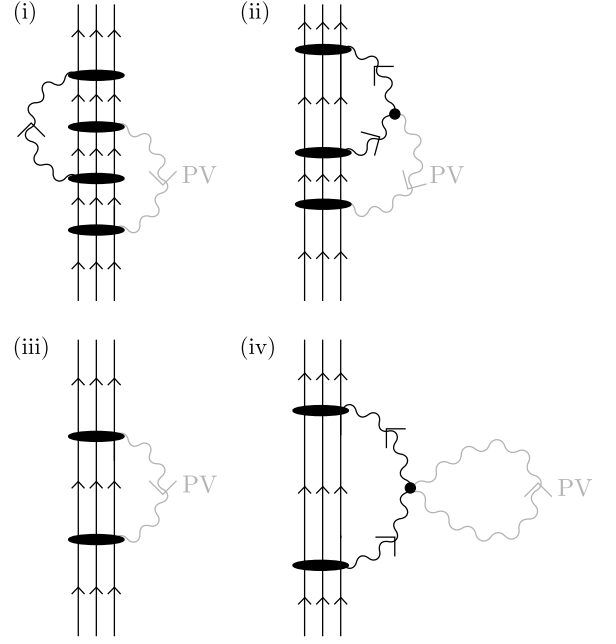


FIG. 19. (i)-(ii) Gluon loop equivalents to the first diagram of Fig. 17(i). When the fermion couples to the background photon field, only diagram (i) may be constructed as the gluon does not carry an electromagnetic charge. When the fermion couples to the background gluon field, both diagram (i) and diagram (ii) may be constructed. Conservation of colour charge indicates that on summing the coupling of the background gluon to the fermion and the background gluon to the loop gluon, this is equal to the coupling of the background gluon to the fermion in the original leading-order diagram (iii). Similarly, diagram (iv) is the counterpart to the third diagram of Fig. 17(i). This diagram is especially interesting as it contributes both to the fermion mass and to the mass of the loop gluon. Note that the two background gluons must couple with the loop gluon at a single vertex, as discussed in Sec. III 1 of Paper V.

3. 1-loop gluon corrections

The next loop corrections to consider are those arising from gluon loops, analogous to the diagrams of Fig. 17. These gluons are foreground particles capable of making excursions outside of the local autocorrelation zone, and hence are massive, but they are also confined, so the length scale involved is of order \mathcal{L}_ψ . Over these scales the gluon loops exhibit at most only the bare gluon mass (including the gluon deficit correction). Only loop corrections to the background photon and background gluon interactions need be considered in the present paper; corrections to the background scalar boson interaction are of $O[\alpha m_{\ell_i}^2/(m_c^*)^2]$ and thus are smaller than the terms of $O(m_{\ell_i}^2/m_{\mathbf{H}}^2)$ in Eq. (76).

Consider the gluon loop counterparts to Fig. 17(i). Where the fermion interacts with the background photon field, these corrections take on the form of Fig. 19(i). For interactions between the fermion and the background

gluon fields they may take on the form of either Fig. 19(i) or (ii), and conservation of colour charge indicates that when these couplings are summed, this is equal to the coupling of the background gluon to the fermion in the original leading-order diagram [Fig. 19(iii)]. Further, when the loop correction is evaluated, this collapses to a numerical multiplier on the original background interaction vertex and the customary application of spinor identities (IV:6–7) yields a non-vanishing contribution to $m_{\ell_i}^2$. It then suffices to consider an example where the coupling of the background gluon and loop gluon vanishes, making it equivalent to the background photon case, evaluate the correction to the interaction vertex, and extrapolate this across all gluon colour combinations by $GL(3, \mathbb{R})$ symmetry.

Figure 19(iv) shows a further diagram which may be constructed using gluon loop corrections. This is a counterpart to the gluon version of the third diagram of Fig. 17(i), again with vertices moved onto the loop boson, and also contributes to the mass of the loop gluon.

Note that in contrast to the photon terms, where the third diagram of Fig. 17(i) was accounted for in the Standard Model, for preon/gluon interactions all loop corrections must be evaluated as there are no corresponding Standard Model terms.

To evaluate these corrections begin with Fig. 19(i), which is the gluon loop counterpart to Fig. 17(i). Start with the fermion coupling to the background photon field, and a specific choice of off-diagonal gluon. Compare with the equivalent EM loop figure and note the following changes:

- The vertex factors increase from $f^2/2$ to f^2 , for a relative factor of 2.
- The boson is off-diagonal, for a relative structural factor of $\frac{5}{3}$.
- The photon source may be any of three charged preons, but the gluon may only be emitted by a preon of appropriate colour. However, any of the three preons may be the preon of that colour, for a net factor of one.
- Emission of the off-diagonal gluon changes the colour of the emitting preon. There are then two preons of that colour which are capable of absorbing the loop gluon, and both of the resulting diagrams count as loop corrections due to the implicit exchange (not shown) of further gluons as a binding interaction sharing momentum between all members of the preon triplet. The choice of absorbing preons gives a factor of 2.
- The loop gluon is massive, and is in the presence of a foreground fermion so experiences a gluon field mass deficit giving a loop factor of $m_{\ell_i}^2/(m_c^*)^2$.
- These factors multiply the equivalent photon loop factor, which is $\alpha/(2\pi)$.

The per-gluon correction weight from this diagram is therefore

$$\frac{10\alpha}{3\pi} \frac{m_{\ell_i}^2}{(m_c^*)^2}. \quad (82)$$

This calculation is repeated for the gluon counterparts to the other two figures of Fig. 17(i), and each of these figures may involve any of nine gluons, for a total weight of

$$\frac{90\alpha}{\pi} \frac{m_{\ell_i}^2}{(m_c^*)^2}. \quad (83)$$

Correction of the background gluon interactions proceeds equivalently, and as noted above the correction to the scalar boson may be ignored at current precision, for a net lepton mass so far of

$$\begin{aligned} m_{\ell_i}^2 = & \frac{f^2}{2} \left[k_i^{(\ell)} \right]^4 \omega_0^2 N_0^8 S_{18,147} C_{\alpha, N_0} \\ & \times \left\{ \frac{q_\ell^2}{e^2} \left[1 + \frac{90\alpha m_{\ell_i}^2}{\pi(m_c^*)^2} \right] + \frac{5m_{\ell_i}^2}{(m_c^*)^2} \left[1 + \frac{90\alpha m_{\ell_i}^2}{\pi(m_c^*)^2} \right] \right. \\ & + \frac{40m_{\ell_i}^2}{3m_{\mathbf{H}}^2 \left[k_i^{(\ell)} N_0 \right]^4} \left(1 - \frac{2\alpha q_\ell^2}{3\pi e^2} \right) \\ & \times \left[1 + O(N_0^{-1}) + O\left(\frac{m_{\ell_i}^2}{m_{\mathbf{H}}^2}\right) + O(\alpha^2) \right] \left. \right\} \\ & \times \left\{ 1 + O\left(\frac{\alpha}{N_0^2}\right) + O\left(\frac{\alpha^2}{N_0}\right) + O\left[\frac{\alpha m_{e_i}^2}{N_0(m_c^*)^2}\right] + \dots \right\} \end{aligned} \quad (84)$$

where the next terms to be determined are the one-loop weak boson corrections.

4. 1-loop weak force corrections

In the interest of brevity, this Section and those which follow specialise to the charged leptons only.

a. Background photon interaction: When the fermion interacts with the background photon field, W boson loops may correct this interaction as shown in Fig. 20. As with the gluon loops in Sec. VB3, the boson loops may be collapsed to numerical factors on the vertices of the corresponding leading-order diagram, and the background field terms contracted using spinor/sigma matrix identities.

Some caution is required with sign—first consider diagram (iii). Evaluating this diagram as a tensor network in the manner of Ref. [16–18], it is readily seen to be an absolute square and therefore yields a contribution to $m_{\ell_i}^2$ which is additive to the leading order term. Diagrams (i) and (ii) contain as a subdiagram a correction to the EM emission process which is usually associated with the opposite sign to direct emission by the fermion; however, compared with diagram (iii) they have also acquired an additional fermion propagator segment which

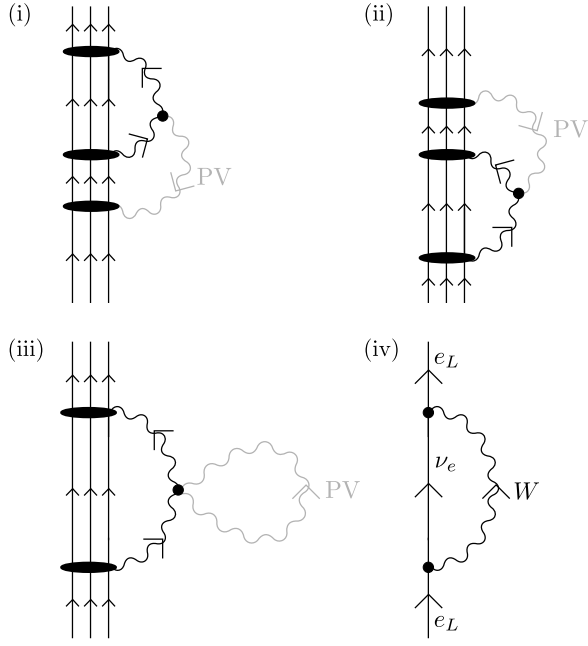


FIG. 20. (i)-(iii) W boson loop corrections to the background vector boson interactions (background photon or background gluon). For background photon terms, ignore the orientation arrows on the background boson lines. (iv) Loop involving a W boson and a neutrino, appearing in the proper self-energy corrections of the Standard Model.

offsets this, so they are also additive. Relative to the leading-order diagram, Figs. 20(i)-(ii) acquire factors

- $(10/3)(m_{\ell_i}^2/m_W^2)$, being the usual (absolute) factor for a W loop correction to an EM vertex,
- $1/2$ due to loss of exchange symmetry for the two background photon/composite fermion interactions. (Even with a composite fermion, an effective vertex is defined on summing over all possible preon/photon pairings and when identical, these effective vertices may still be exchanged for a symmetry factor of 2.)

Diagram (iii) retains the exchange symmetry, this time on the two copies of the photon operator at the vertex, so attracts the factor of $(10/3)(m_{\ell_i}^2/m_W^2)$ only.

Finally, consider the Standard Model counterpart: The charged lepton Proper Self-Energy (PSE) terms in the Standard Model give rise to the W /neutrino loop shown in Fig. 20(iv). This gives rise to a term analogous to Fig. 20(iii), but has no counterpart to the symmetry factor associated with the pair of identical photon operators on the pseudovacuum interaction vertex. Its associated factor is therefore $(5/3)(m_{\ell_i}^2/m_W^2)$, which must be deducted. The net weight of the W boson loop corrections is thus

$$\frac{5\alpha m_{\ell_i}^2}{2\pi m_W^2}. \quad (85)$$

Next considering the Z boson loops, these take form directly analogous to Fig. 17, and by arguments similar to the above are also seen to all be additive. Noting that the Z boson couples with opposite sign to e_L and e_R , and that mass vertices in the Standard Model reverse electron spin whereas the pseudovacuum couplings do not, the Z boson equivalents to the first two diagrams of Fig. 17(i) are therefore of opposite sign to their Standard Model counterparts and hence attract a factor of two, to first offset the Standard Model-derived term in the PSE, and then implement the actual correction. The third diagram of Fig. 17(i), on the other hand, has the same sign as its Standard Model counterpart and thus yields no net contribution to $m_{\ell_i}^2$. The net outcome from Z boson loops is a term with weight

$$-\frac{4f_Z\alpha m_{\ell_i}^2}{2\pi m_W^2} \quad (86)$$

where f_Z is as defined in Eq. (17). Overall, the weight of the weak boson corrections to the background photon interaction is seen to be

$$\frac{(5 - 4f_Z)\alpha m_{\ell_i}^2}{2\pi m_W^2}. \quad (87)$$

b. Background gluon interactions: This term is readily obtained as the calculation proceeds similarly to Sec. VB 4 a, and it is found to be right at the threshold of relevance at the precision employed the current paper.

As usual, start with the fermion interaction with a single off-diagonal background gluon channel and then use $GL(3, \mathbb{R})$ symmetry to multiply by nine for the contributions of the other eight gluons. For the gluon channels, the background gluons continue to couple to the fermion and not the looping W boson, so when evaluating the equivalents of Figs. 20(i)-(ii) there is no factor of $\frac{1}{2}$ for lost symmetry. The calculation is otherwise equivalent, for net W and Z corrections of

$$\frac{(25 - 12f_Z)\alpha m_{\ell_i}^2}{6\pi m_W^2}. \quad (88)$$

c. Background scalar boson interaction: These terms fall below the threshold of relevance, being smaller by a factor of $O(\alpha)$ than the unevaluated correction of $O(m_{\ell_i}^2/m_H^2)$.

The cumulative expression for charged lepton mass in-

incorporating weak boson corrections is therefore

$$\begin{aligned}
m_{\ell_i}^2 = & \frac{f^2}{2} \left[k_i^{(\ell)} \right]^4 \omega_0^2 N_0^8 S_{18,147} C_{\alpha, N_0} \\
& \times \left\{ \left[1 + \frac{90\alpha m_{\ell_i}^2}{\pi(m_c^*)^2} + \frac{(5-4f_Z)\alpha m_{\ell_i}^2}{2\pi m_W^2} \right] \right. \\
& + \frac{5m_{\ell_i}^2}{(m_c^*)^2} \left[1 + \frac{90\alpha m_{\ell_i}^2}{\pi(m_c^*)^2} + \frac{(25-12f_Z)\alpha m_{\ell_i}^2}{6\pi m_W^2} \right] \\
& + \frac{40m_{\ell_i}^2}{3m_{\mathbf{H}}^2 \left[k_i^{(\ell)} N_0 \right]^4} \left(1 - \frac{2\alpha}{3\pi} \right) \\
& \times \left[1 + O(N_0^{-1}) + O\left(\frac{m_{\ell_i}^2}{m_{\mathbf{H}}^2}\right) + O(\alpha^2) \right] \Bigg\} \\
& \times \left\{ 1 + O\left(\frac{\alpha}{N_0^2}\right) + O\left(\frac{\alpha^2}{N_0}\right) + O\left[\frac{\alpha m_{e_i}^2}{N_0(m_c^*)^2}\right] + \dots \right\}
\end{aligned} \tag{89}$$

5. 1-loop scalar corrections

The largest of these terms are the scalar loop corrections to the background photon interaction. These are of comparable magnitude to the photon loop corrections to the background scalar interaction. Leaving these terms unevaluated replaces the factor of $[1 - 2\alpha/(3\pi)]$ on the scalar interaction term with an unspecified correction of $[1 + O(\alpha)]$.

6. 2-loop EM corrections

By the same arguments as Sec. VB1, the massless $O(\alpha^2)$ corrections are identical for the background photon and gluon interactions and coincide with their Standard Model counterparts. The massless 2-loop EM corrections therefore yield at most a correction of $O(\alpha^2)$ to the scalar term, which is smaller than the $O(\alpha)$ term from Sec. VB5.

The next term which may differentially affect the photon and gluon terms, and which exhibits dependency on particle generation, is a two-loop massive contribution. All relevant masses are of comparable magnitude, $m_c^2 \sim m_W^2 \sim m_Z^2 \sim m_{\mathbf{H}}^2$, and gluon terms have thus far outweighed weak sector terms, therefore write this correction in terms of the gluon mass. It is also useful to pull all higher-order corrections out into the final term, giving the cumulative expression for charged lepton mass incorporating all loop corrections evaluated in this paper

as

$$\begin{aligned}
m_{\ell_i}^2 = & \frac{f^2}{2} \left[k_i^{(\ell)} \right]^4 \omega_0^2 N_0^8 S_{18,147} C_{\alpha, N_0} \\
& \times \left\{ \left[1 + \frac{90\alpha m_{\ell_i}^2}{\pi(m_c^*)^2} + \frac{(5-4f_Z)\alpha m_{\ell_i}^2}{2\pi m_W^2} \right] \right. \\
& + \frac{5m_{\ell_i}^2}{(m_c^*)^2} \left[1 + \frac{90\alpha m_{\ell_i}^2}{\pi(m_c^*)^2} + \frac{(25-12f_Z)\alpha m_{\ell_i}^2}{6\pi m_W^2} \right] \\
& + \frac{40m_{\ell_i}^2}{3m_{\mathbf{H}}^2 \left[k_i^{(\ell)} N_0 \right]^4} \Bigg\} \\
& \times \left(1 + O\left(\frac{\alpha}{N_0^2}\right) + O\left(\frac{\alpha^2}{N_0}\right) + O\left[\frac{\alpha m_{e_i}^2}{N_0(m_c^*)^2}\right] \right. \\
& + O\left[\frac{\alpha^2 m_{\ell_i}^2}{(m_c^*)^2}\right] + O\left\{\frac{\alpha m_{\ell_i}^2}{m_{\mathbf{H}}^2 \left[k_i^{(\ell)} N_0 \right]^4}\right\} \\
& \left. + O\left\{\frac{m_{\ell_i}^2}{m_{\mathbf{H}}^2 \left[k_i^{(\ell)} \right]^4 N_0^5}\right\} + O\left\{\frac{m_{\ell_i}^4}{m_{\mathbf{H}}^4 \left[k_i^{(\ell)} N_0 \right]^4}\right\} \right).
\end{aligned} \tag{90}$$

C. Corrections to the lepton mass angle

1. Origin of corrections

There remains one more substantial correction to evaluate. The leading-order contributions to the lepton mass vertices and the preon colour mixing matrix were evaluated in Sec. VA. Loop corrections to the mass vertices were evaluated in Sec. VB. It remains now to determine how these loop corrections impact the preon colour mixing matrix K_ℓ .

When this matrix was constructed in Sec. VA1 there was an implicit assumption that all eigenvectors experience equal couplings to the background fields. The eigenvalues of matrix K_ℓ then imparted different masses to the three eigenvectors, corresponding to the three members of a given fermion family. However, from Eq. (89) it is apparent that the higher-order corrections to the pseudovacuum coupling themselves depend on particle mass, leading to differential augmentation of the three eigenvectors (mass channels). As these eigenvectors correspond to different vectors in colour space, imparting different relative phases to the gluon couplings between the preon triplets, a change in the relative pseudovacuum couplings for the different eigenvectors will impact the colour mixing process. Conveniently, it proves possible to represent this modification by a correction to the value of θ_ℓ .

Recognising that the fermion masses vary between different particle families, it is necessary to specify the family for which the corrected value of θ_ℓ is being evaluated. This is done by replacing ℓ with a member of the particle family in question, e.g. e , μ , or τ for the electron family.

2. Preamble

To obtain a corrected expression for the electron mass angle at some energy scale \mathcal{E} , first recall that the eigenvectors $\{v_i | i \in \{1, 2, 3\}\}$ of K_ℓ (59–61) are independent of the value of θ_ℓ . For the electron family, matrix K_ℓ therefore always admits the decomposition

$$K_\ell = \sum_{i=1}^3 k_i^{(\ell)} v_i v_i^\dagger \quad (91)$$

where

$$v_1 v_1^\dagger = \frac{1}{3} \begin{pmatrix} 1 & 1 & 1 \\ 1 & 1 & 1 \\ 1 & 1 & 1 \end{pmatrix} \quad (92)$$

$$v_2 v_2^\dagger = \frac{1}{3} \begin{pmatrix} 1 & e^{\frac{2\pi i}{3}} & e^{-\frac{2\pi i}{3}} \\ e^{-\frac{2\pi i}{3}} & 1 & e^{\frac{2\pi i}{3}} \\ e^{\frac{2\pi i}{3}} & e^{-\frac{2\pi i}{3}} & 1 \end{pmatrix} \quad (93)$$

$$v_3 v_3^\dagger = \frac{1}{3} \begin{pmatrix} 1 & e^{-\frac{2\pi i}{3}} & e^{\frac{2\pi i}{3}} \\ e^{\frac{2\pi i}{3}} & 1 & e^{-\frac{2\pi i}{3}} \\ e^{-\frac{2\pi i}{3}} & e^{\frac{2\pi i}{3}} & 1 \end{pmatrix}. \quad (94)$$

Then note that the imaginary components of the off-diagonal matrix elements arise from components 2 and 3 only (93–94), with an increase in component 2 (corresponding, for charged leptons, to the muon) making a positive-signed contribution to the imaginary component in $[K_\ell]_{12}$, $[K_\ell]_{23}$, and $[K_\ell]_{31}$. Examining the vectors on the complex plane associated with $\exp(\theta_e) = \exp(-3\pi i/4)$ and a small correction proportional to $\exp(2\pi i/3)$, it is seen that the action of this correction is to increase the magnitude of θ_ℓ (making it more negative). Similarly, an isolated increase in component 3 (the tau) decreases the magnitude of θ_ℓ . Finally, an isolated increase in component 1 (the electron) affects only the real component of an entry such as $[K_\ell]_{12}$ and thus when $[K_\ell]_{12}$ is complex, once again affects the value of θ_ℓ . When θ_ℓ is no longer fixed to be $-3\pi/4$, it is labelled by the relevant particle family, e.g. θ_e , and it becomes necessary to specify K_ℓ as $K_\ell(\theta_\ell)$ for some family ℓ .

Next, recognise that it is convenient to write the mass interaction as a leading-order term derived from the background photon field (and associated with colour mixing matrix K_ℓ as derived Sec. V A 1) plus corrections. For the charged lepton masses, this corresponds to rewriting Eq. (89) as

$$m_{e_i}^2 = \frac{f^2}{2} [k_i^{(e)}]^4 \omega_0^2 N_0^8 S_{18,147} C_{\alpha, N_0} \times [1 + \Delta_e(m_{e_i})] [1 + \mathcal{O}_e(m_{e_i})] \quad (95)$$

$$= [m_{e_i}^{(0)}]^2 C_{\alpha, N_0} [1 + \Delta_e(m_{e_i})] [1 + \mathcal{O}_e(m_{e_i})] \quad (96)$$

$$\Delta_e(m_{e_i}) = \frac{90\alpha m_{e_i}^2}{\pi(m_c^*)^2} + \frac{(5 - 4f_Z)\alpha m_{e_i}^2}{2\pi m_W^2} \quad (97)$$

$$+ \frac{5m_{e_i}^2}{(m_c^*)^2} \left[1 + \frac{90\alpha m_{e_i}^2}{\pi(m_c^*)^2} + \frac{(25 - 12f_Z)\alpha m_{e_i}^2}{6\pi m_W^2} \right]$$

$$+ \frac{40m_{e_i}^2}{3m_{\mathbf{H}}^2 [k_i^{(e)} N_0]^4}$$

$$\mathcal{O}_e(m_{e_i}) = \mathcal{O}\left(\frac{\alpha}{N_0^2}\right) + \mathcal{O}\left(\frac{\alpha^2}{N_0}\right) + \mathcal{O}\left[\frac{\alpha m_{e_i}^2}{N_0(m_c^*)^2}\right]$$

$$+ \mathcal{O}\left[\frac{\alpha^2 m_{e_i}^2}{(m_c^*)^2}\right] + \mathcal{O}\left\{\frac{\alpha m_{e_i}^2}{m_{\mathbf{H}}^2 [k_i^{(e)} N_0]^4}\right\} \quad (98)$$

$$+ \mathcal{O}\left\{\frac{m_{e_i}^2}{m_{\mathbf{H}}^2 [k_i^{(e)}]^4 N_0^5}\right\} + \mathcal{O}\left\{\frac{m_{e_i}^4}{m_{\mathbf{H}}^4 [k_i^{(e)} N_0]^4}\right\}$$

where $\{e_1, e_2, e_3\} = \{e, \mu, \tau\}$ and the subscript e on Δ_e indicates the family $\{e, \mu, \tau\}$ rather than the electron in particular. As can be readily seen from Eq. (97), the amplitudes of these corrections to particle mass are dependent upon the squared lepton masses $m_{e_i}^2$, with the largest corrections being those associated with the tau. The charged lepton mixing matrix $K_e(\theta_e)$ is implicitly dependent on the same corrections, as changes to the particle mass ratios affect colour mixing, and hence the co-ordinate transformation required to restore colour neutrality. Allowing the corrections to augment mass and also to adjust $K_e(\theta_e)$ is not double-counting, as the mass correction *induces* the corresponding adjustment in the co-ordinate transformation implemented by $K_e(\theta_e)$. The co-ordinate transformation does, however, have an effect on the magnitude of the mass correction term, and this effect must be compensated for—see Sec. V C 5.

Note that Δ_e and \mathcal{O}_e are also dependent on $k_i^{(e)}$ which in turn is dependent on $K_e(\theta_e)$ which is dependent on θ_e which is dependent on Δ_e which is dependent on m_{e_i} . No attempt is made to express full dependencies of parameters save through the equations defining them, and going forward, notation such as $\Delta_e(m_{e_i})$ or $\Delta_e(\mathcal{E})$ is merely a heuristic to remind the reader of a parameter's dependency on some stated energy scale. Similarly, for $K_e(\theta_e)$, dependency on θ_e is shown to clearly distinguish the mass-dependent $K_e(\theta_e)$ from the mass-independent K_ℓ .

3. First-order correction to K_ℓ^4 from the tau channel

To understand how these corrections to lepton masses affect the matrices K_ℓ , consider the leading order term $[m_{e_i}^{(0)}]^2$ which arises from the set of nine diagrams described in the caption of Fig. 15, and may be thought of as the action of an operator $[\hat{m}^{(0)}]^2$ on the preon triplet comprising a sum over nine terms. The action of this operator on the colour space of the preon triplet breaks

colour neutrality, but this is then corrected by application term-by-term of four matrices (or operators) K_ℓ , heuristically K_ℓ^4 (with implicit action of each operator on the appropriate Hilbert space as per the appropriate diagram of Fig. 15), such that $K_\ell^4 [\hat{m}^{(0)}]^2$ as a whole leaves the colour of the preon triplet unchanged up to a sum over cycles $r \rightarrow g \rightarrow b \rightarrow r$.

As seen in Eq. (96), higher-order corrections enhance the action of $[\hat{m}^{(0)}]^2$ on eigenstate e_i by a factor of $[1 + \Delta_e(m_{e_i})]$. If colour neutrality is to be conserved, then for colour-changing diagrams [including those which would mix colours under some global $SU(3)_C$ transformation, such as interaction with the diagonal gluons of $SU(3)_C$] there must be an equivalent enhancement of the matrices K_ℓ ,

$$K_\ell \rightarrow K_e(\theta_e) \quad (99)$$

[where dependence on $\theta_e(\{m_{e_i} | i \in \{1, 2, 3\}\})$ is assumed but will subsequently be shown] such that the action of $[K_e(\theta_e)]^4$ on lepton e_i is equivalent to the action of

$$K_\ell^4 [1 + \Delta_e(m_{e_i})]. \quad (100)$$

As the largest such correction arises from the most massive particle, begin by considering e_3 , the tau. First note that introduction of a mass dependency for the matrices $K_e(\theta_e)$ implies that the bosons associated with the colour-neutrality-preserving co-ordinate transformation are no longer parameterless, and may therefore carry momentum in the higher-order diagrams. They must therefore be represented explicitly as per Fig. 21. By construction these bosons only interact at the boundary of the transformed co-ordinate patch, and are consequently both foreground and massless. Let the diagrams of Fig. 21(i)-(iii), having two co-ordinate transformation bosons, be termed “first order”, and for now ignore diagrams having four co-ordinate transformation bosons (“second order”) or more.

Regarding the two co-ordinate transformation bosons of Fig. 21(i)-(ii), their vertex factors are incorporated into the leading order matrix K_ℓ . Integration over their degrees of freedom then yields a factor per diagram of $(4\pi)^{-2}$ [not $(2\pi)^{-2}$, as they are not self-dual and thus their loop is less symmetric than that for the photon]. Note that Fig. 21(ii) counts as a loop diagram as there are implicit gluon-mediated couplings between the preonic constituents of the lepton, which are massless over the length-scale involved $[O(\mathcal{L}_0)]$ and complete closure of the loop.

Recognising that the leading term calculation does not perform any net colour mixing beyond the unmodified, constant factors of K_ℓ^4 , the resulting factor of $2 \cdot (4\pi)^{-2}$ does not appear in the leading term calculation. Its effect is seen only on the diagrams in $\Delta_e(m_\tau)$, where it represents variations in colour mixing relative to K_ℓ^4 , and multiplies any correction to K_ℓ^4 by a factor of $2 \cdot (4\pi)^{-2}$.

Next, recognise that the components of each matrix $K_e(\theta_e)$ which perform rotations on $SU(3)_C$ are composed

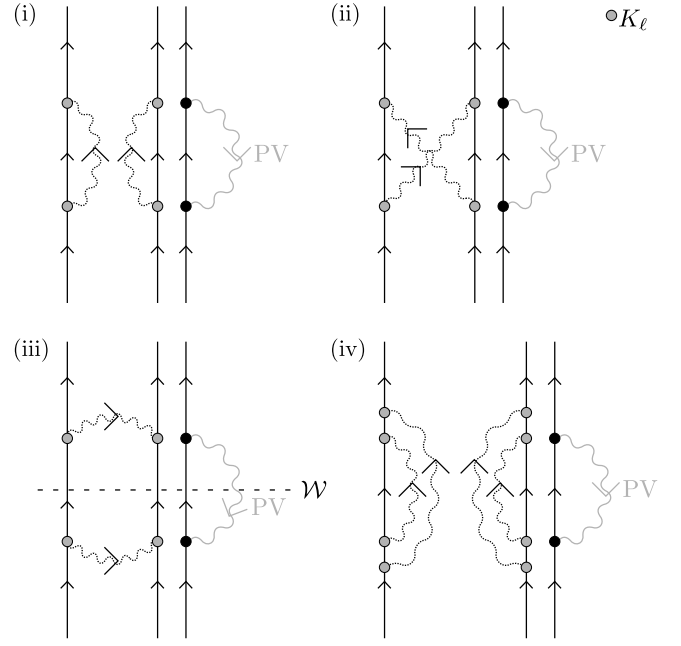


FIG. 21. When the matrices K_ℓ are replaced by $K_e(\theta_e)$, which depends on energy scale, this induces a pair of gauge bosons which may in principle connect the four matrices $K_e(\theta_e)$ in any of three ways [shown for Fig. 15(i) in diagrams (i)-(iii)]. In diagram (i), the bosons each connect to two matrices $K_e(\theta_e)$ on the same preon and thus enact a co-ordinate transformation followed by its inverse. In diagram (ii), where the bosons are crossed, there may be a permutation of the preon colour labels but overall colour neutrality is nevertheless conserved. Diagram (iii) contrasts with the other two in that the boson trajectories are orthogonal to the preon trajectories. For a worldsheet such as that shown (labelled \mathcal{W}), which is equidistant between the boson vertices and isochronous in the rest frame of the particle, the total number of oriented crossings for each of the bosons in diagram (iii) is zero regardless of the trajectory followed. This implies that these bosons do not describe a co-ordinate transformation extant at this worldsheet, and thus this diagram does not contribute to $K_e(\theta_e)$. Diagram (iv) is an example second-order diagram having four bosons arising from the co-ordinate transformation and spanning from the lower to the upper collection of matrices $K_e(\theta_e)$. This diagram represents the consecutive application of two (possibly different) transformations in $SU(3)_C$ to each preon.

from a weighted superposition of some set of representation matrices λ'_i [possibly, but not necessarily the rescaled Gell-Mann matrices λ_i in Eqs. (II:38–39)], of which there are eight. (The ninth basis element is associated with the N boson and the trivial representation, but does not change colour and is independent of θ_ℓ so is not yet of interest here.) An appropriate choice of basis permits every off-diagonal element in $K_e(\theta_e)$ to be associated with a single basis element {for example, in K_ℓ , entry $[K_\ell]_{12}$ is associated with $(\lambda_1 + \lambda_2)/\sqrt{2}$ }. A change to θ_e may correspond to a change in choice of representation matrices [e.g. to $\lambda_1 \cos \beta + \lambda_2 \sin \beta$ for some angle β] but this abil-

ity to construct a single basis element corresponding to a particular entry in $K_e(\theta_e)$ persists for any reasonably small perturbation around $\theta_e = -3\pi/4$.

Now consider a preon in Fig. 15(i) or (ii) which has two matrices $K_e(\theta_e)$ acting on it, and recognise that if the portion of $K_e(\theta_e)$ which performs colour transformations is decomposed into these eight components, then if a given component λ'_i acts on the preon in the lower position, then its conjugate must act in the upper position for the foreground preon colour to be left invariant overall [19]. The action of the *pair* of matrices $K_e(\theta_e)$ on this boson consequently admits decomposition into eight channels, enumerated by the family of orthogonal representation matrices λ'_i appearing at the lower matrix $K_e(\theta_e)$.

Next, consider the remaining two matrices $K_e(\theta_e)$ when these are not on the same preon. In this situation the representation matrices present will be conjugate up to a colour cycle $r \rightarrow g \rightarrow b \rightarrow r$ or its inverse. As the only colour-changing bosons in the pseudovacuum are gluons, and $SU(3)_C$ symmetry is preserved on the gluon sector and in the definition of the charged lepton, evaluation of any diagram where the entries from $K_e(\theta_e)$ are offset by a colour cycle is necessarily equivalent to evaluation of a diagram where they are not offset. It is therefore acceptable to evaluate entries in $K_e(\theta_e)$ under the assumption that all matrices $K_e(\theta_e)$ appear in conjugate pairs. In addition, in all diagrams all representation matrices are multiplied by their conjugate (whether independently or in conjunction with the representation matrices associated with the bosonic vertices) and thus the terms arising from all 64 channels contributing to the actions of the matrices $K_e(\theta_e)$ on the preon triplet are additive on the same (net trivial) charge sector, and therefore summed. By $SU(3)_C$ symmetry, each channel will contribute equally to the overall correction to the leading order diagram.

Now consider the single channel associated with a specific off-diagonal entry in at least one lower matrix $K_e(\theta_e)$. For definiteness, let this be $[K_e(\theta_e)]_{12}$. As there are, overall, 64 contributing channels, each channel must produce a net correction of $\Delta_e(m_\tau)/64$. However, the synthetic bosons multiply all correction diagrams by a factor of $2 \cdot (4\pi)^{-2}$ and thus $[K_e(\theta_e)]_{12}$ and $[K_e(\theta_e)]_{21}$ must satisfy

$$\begin{aligned} [K_e(\theta_e)]_{12}^2 [K_e(\theta_e)]_{21}^2 &= [K_\ell]_{12}^2 [K_\ell]_{21}^2 \left[1 + \frac{(4\pi)^2}{2 \cdot 64} \Delta_e(m_\tau) \right] \\ &= [K_\ell]_{12}^2 [K_\ell]_{21}^2 \left[1 + \frac{\pi^2}{8} \Delta_e(m_\tau) \right] \end{aligned} \quad (101)$$

$$\Rightarrow [K_e(\theta_e)]_{12} [K_e(\theta_e)]_{21} = [K_\ell]_{12} [K_\ell]_{21} \sqrt{1 + \frac{\pi^2}{8} \Delta_e(m_\tau)}. \quad (102)$$

Noting that $[K_\ell]_{12} = [K_\ell]_{21}^\dagger$, it is convenient to write

$$\delta_e(n) = \sqrt{1 + \frac{\pi^2 n}{8}} - 1 \quad (103)$$

$$[1 + \delta_e(n)] = [1 + i\sqrt{\delta_e(n)}][1 - i\sqrt{\delta_e(n)}] \quad (104)$$

and assign the corresponding off-diagonal entries of $K_e(\theta_e)$ to be

$$\begin{aligned} [K_e(\theta_e)]_{12} &= [K_\ell]_{12} [1 \pm i\sqrt{\delta_e[\Delta_e(m_\tau)]}] \\ [K_e(\theta_e)]_{21} &= [K_\ell]_{21} [1 \mp i\sqrt{\delta_e[\Delta_e(m_\tau)]}], \end{aligned} \quad (105)$$

preserving the hermiticity of $K_e(\theta_e)$.

By the factor of $\pm i$ on the correction term, this correction is orthogonal to the leading-order value of $[K_\ell]_{12}$. As this orthogonality is independent of the value of θ_e , this implies that for a non-infinitesimal correction, $[K_\ell]_{12} \sqrt{\delta_e[\Delta_e(m_\tau)]}$ is the length of an arc. The corresponding correction to θ_ℓ is

$$\theta_\ell \rightarrow \theta_\ell \pm \sqrt{\delta_e[\Delta_e(m_\tau)]}. \quad (106)$$

In the vicinity of $\theta_\ell = -3\pi/4$, this may be rewritten

$$\theta_\ell \rightarrow \theta_\ell \left\{ 1 \mp \frac{4\sqrt{\delta_e[\Delta_e(m_\tau)]}}{3\pi} \right\}. \quad (107)$$

As per the discussion under Eqs. (92–94), the tau correction is known to decrease the magnitude of θ_ℓ , giving

$$[K_e(\theta_e)]_{12} = \frac{e^{i\theta_e}}{\sqrt{2}} = [K_\ell]_{12} \left\{ 1 + i\sqrt{\delta_e[\Delta_e(m_\tau)]} + \dots \right\} \quad (108)$$

$$\theta_e = -\frac{3\pi}{4} \left\{ 1 - \frac{4\sqrt{\delta_e[\Delta_e(m_\tau)]}}{3\pi} \right\} \quad (109)$$

where the uncorrected value of θ_ℓ has been written explicitly as $-\frac{3\pi}{4}$.

4. Second-order correction to K_ℓ^4 from the tau channel

The first-order correction to K_ℓ^4 is applied to all diagrams which modify the colour mixing process, i.e. all diagrams contributing to Δ_e . For these diagrams, this correction is equivalent by construction to enacting the transformation

$$K_\ell^4 \rightarrow K_\ell^4 [1 + \Delta_e(m_\tau)], \quad (110)$$

resulting in a relative increase in these diagrams' contribution to particle mass equivalent to

$$\Delta_e(m_\tau) \rightarrow \Delta_e(m_\tau)[1 + \Delta_e(m_\tau)]. \quad (111)$$

Any species-dependent increase in mass affects colour mixing in precisely the way described above for correction $\Delta_e(m_\tau)$, regardless of whether this increase is diagrammatic (as in the first-order component) or gauge-dependent and derived from a change to θ_e (as here). This correction therefore attracts a further smaller correction to K_ℓ , enhancing the first-order correction calculated above. While this series may be continued indefinitely, it is convenient to truncate at second order for a precision of $\mathcal{O}[\Delta_e^2(m_\tau)]$, ensuring that the error in numerical calculations is dominated by the error in $\Delta_e(m_\tau)$ itself, and not in the evaluation of $\delta_e[\Delta_e(m_\tau)]$.

To implement the corresponding adjustment to $K_e(\theta_e)$, let the $\mathcal{O}[\Delta_e^2(m_\tau)]$ term be compensated by the second-order diagrams of which Fig. 21(iv) is a prototype. In these diagrams, a first-order correction [Fig. 21(i)-(ii)] is supplemented by a further, smaller correction.

For Figs. 21(i)-(ii) there is a symmetry factor of two corresponding to crossing or not crossing the bosons. For Fig. 21(iv),

- the inner pair may be crossed (factor of two),
- the outer pair may be crossed (factor of two),
- the inner and outer bosons on the left may be exchanged (factor of two), and
- the inner and outer bosons on the right may be exchanged (factor of two).

The factor of $2 \cdot (4\pi)^{-2}$ associated with the set of diagrams Figs. 21(i)-(ii) becomes a factor of $16 \cdot (4\pi)^{-4}$ for the set of diagrams derived from Fig. 21(iv). The expression for $[K_e(\theta_e)]_{12}^2 [K_e(\theta_e)]_{21}^2$ then becomes

$$\begin{aligned} & [K_e(\theta_e)]_{12}^2 [K_e(\theta_e)]_{21}^2 \\ &= [K_\ell]_{12}^2 [K_\ell]_{21}^2 \left[1 + \frac{(4\pi)^2}{2 \cdot 64} \Delta_e(m_\tau) + \frac{(4\pi)^4}{16 \cdot 64^2} \Delta_e^2(m_\tau) \right] \\ &= [K_\ell]_{12}^2 [K_\ell]_{21}^2 \left\{ 1 + \frac{\pi^2}{8} \Delta_e(m_\tau) \left[1 + \frac{\pi^2}{32} \Delta_e(m_\tau) \right] \right\} \end{aligned} \quad (112)$$

for a redefinition of $\delta_e(n)$ in Eq. (109) to

$$\delta_e(n) = \sqrt{1 + \frac{\pi^2 n}{8} \left(1 + \frac{\pi^2 n}{32} \right)} - 1. \quad (113)$$

The next order term extends $\delta_e(n)$ to

$$\delta_e(n) = \sqrt{1 + \frac{\pi^2 n}{8} \left[1 + \frac{\pi^2 n}{32} \left(1 + \frac{\pi^2 n}{72} \right) \right]} - 1 \quad (114)$$

but its effects are verified to fall below the threshold of relevance for the present paper when evaluated in Sec. VIC.

5. Reparameterisation of θ_e

The above transformations have maintained colour neutrality, but at the expense of introducing an additional multiplicative factor of $[1 + \Delta_e(m_\tau)]$ on all diagrams which affect the colour mixing process [including all diagrams in $\Delta_e(m_\tau)$, by virtue of matrices K_ℓ], as per Eq. (100). In effect this is equivalent to replacing any instance of $\Delta_e(m_\tau)$ with $\Delta_e(m_\tau) \cdot [1 + \Delta_e(m_\tau)]$. This replacement, in turn, induces further corrections to K_ℓ , which then induces further corrections to the effective value of $\Delta_e(m_\tau)$, and so forth. The largest correction to $\Delta_e(m_\tau)$ arising from this effect is of order $m_\tau^4/(m_c^*)^4$, which is large compared with $\mathcal{O}_e(m_\tau)$. It is therefore necessary to evaluate how this series in $\Delta_e(m_\tau)$ affects m_τ^2 , but this will be done indirectly.

First, note that convergence of the series in $\Delta_e(m_\tau)$ yields a unique value of m_τ^2 with associated unique values of $\theta_e(\Delta_e)$ and $\Delta_e(m_\tau)$, and is identified by consistency of equations in $\Delta_e(m_\tau)$ (97), $\theta_e(\Delta_e)$ (109), and $k_3^{(e)}$ (62) [which is now a function of $\theta_e(\Delta_e)$]:

$$m_\tau^2 = \frac{f^2}{2} \left[k_3^{(e)}(\theta_e) \right]^4 \omega_0^2 N_0^8 S_{18,147} C_{\alpha, N_0} \quad (115)$$

$$\begin{aligned} \Delta_e &= \frac{90\alpha m_\tau^2}{\pi(m_c^*)^2} + \frac{(5-4f_Z)\alpha m_\tau^2}{2\pi m_W^2} \\ &+ \frac{5m_\tau^2}{(m_c^*)^2} \left[1 + \frac{90\alpha m_\tau^2}{\pi(m_c^*)^2} + \frac{(25-12f_Z)\alpha m_\tau^2}{6\pi m_W^2} \right] \\ &+ \frac{40m_\tau^2}{3m_H^2 \left[k_3^{(e)} N_0 \right]^4} \end{aligned} \quad (116)$$

$$\theta_e = -\frac{3\pi}{4} \left\{ 1 - \frac{4\sqrt{\delta_e[\Delta_e(m_\tau)]}}{3\pi} \right\} \quad (109)$$

$$k_n^{(e)} = 1 + \sqrt{2} \cos \left[\theta_e - \frac{2\pi(n-1)}{3} \right]. \quad (117)$$

Given the value of m_τ and thus $\Delta_e(m_\tau)$ for which these equations are mutually consistent, now reparameterise by writing

$$\Delta_e(m_\tau) = \Delta'_e(m_\tau)[1 - \Delta'_e(m_\tau)] \quad (118)$$

such that prior to iterating, the tau mass equation is

$$\begin{aligned} m_\tau^2 &= \frac{f^2}{2} \left[k_i^{(e)}(\theta_e) \right]^4 \omega_0^2 N_0^8 S_{18,147} C_{\alpha, N_0} \\ &\times \{ [1 + \Delta'_e(m_\tau)][1 - \Delta'_e(m_\tau)] \} [1 + \mathcal{O}_e(m_\tau)]. \end{aligned} \quad (119)$$

On implementing the associated correction to θ_e as before, all occurrences of $\Delta_e(m_\tau)$ are incremented to $\Delta_e(m_\tau)[1 + \Delta_e(m_\tau)]$ and thus the factor of

$$\{ [1 + \Delta'_e(m_\tau)][1 - \Delta'_e(m_\tau)] \} \quad (120)$$

in m_τ^2 becomes

$$\begin{aligned} 1 + \Delta'_e(m_\tau)[1 - \Delta'_e(m_\tau)]\{1 + \Delta'_e(m_\tau)[1 - \Delta'_e(m_\tau)]\} \\ = 1 + \Delta'_e(m_\tau) + \mathcal{O}\{[\Delta'_e(m_\tau)]^3\}. \end{aligned} \quad (121)$$

Under this reparameterisation there is no $\mathcal{O}\{[\Delta'_e(m_\tau)]^2\}$ term in m_τ^2 .

But what, then, does $\theta_e(\Delta_e)$ look like when written in terms of Δ'_e ? Observe that $\theta_e(\Delta'_e)$ yields a correction to Δ_e in Eq. (115) of

$$\{1 + \Delta'_e(m_\tau)[1 - \Delta'_e(m_\tau)]\} \quad (120)$$

in place of $[1 + \Delta_e(m_\tau)]$, consistent with Eq. (118). However, this correction to Eq. (115) arises from the application of four $K_e(\theta_e)$ matrices as per Fig. 15, which may be thought of as two channels each containing two $K_e(\theta_e)$ matrices. In Fig. 15 this may nominally be identified as one channel per participating preon, though in practice an arbitrary basis may be chosen across these channels and this anyway undergoes mixing during propagation due to the preon binding couplings (not shown). Indeed, because of this mixing, Fig. 15 may likewise be considered to contain two such channels. In each case, the correction must be factorised across these two channels.

Within each of these channels are a further nine subchannels corresponding to the nine entries in $K_e(\theta_e)$ identified with the nine basis elements of $\text{GL}(3, \mathbb{R})$. In contrast, the calculation of θ_e is performed on a single channel of $\text{SU}(3)_C$, and thus on a single channel of $\text{GL}(3, \mathbb{R})$. It therefore follows that the calculation of θ_e must be performed with respect to only one ninth of the correction to $\Delta'_e(m_\tau)$, so as to deliver one ninth of the channel's total correction in each subchannel.

The net effect of both of these considerations is to define

$$\theta_e(\Delta'_e) = -\frac{3\pi}{4} \left(1 - \frac{4\sqrt{\delta_e\{r[\Delta'_e(m_\tau)]\}}}{3\pi} \right) \quad (122)$$

$$r(n) = n \cdot \sqrt{1 - \frac{n}{9}}. \quad (123)$$

which, taken in conjunction with Eq. (115) without requiring any higher-order terms, yields a particle mass accurate to a precision of $\mathcal{O}\{[\Delta_e(m_\tau)]^2\}$.

Dropping the primes, it follows that if $\theta_e(\Delta_e)$ is redefined as per Eq. (122) and *no* corrective terms are introduced on Eq. (115), the value of m_τ^2 thus obtained will be consistent to $\mathcal{O}\{[\Delta_e(m_\tau)]^2\}$ with those obtained from Eqs. (109,115–117) on iteration as described earlier. The next order of corrections may then be incorporated into

\mathcal{O}_e (98), and corresponds to $\mathcal{O}[m_{e_i}^6/(m_c^*)^6]$:

$$\begin{aligned} \mathcal{O}_e(m_{e_i}) = & \mathcal{O}\left(\frac{\alpha}{N_0^2}\right) + \mathcal{O}\left(\frac{\alpha^2}{N_0}\right) + \mathcal{O}\left[\frac{\alpha m_{e_i}^2}{N_0(m_c^*)^2}\right] \\ & + \mathcal{O}\left[\frac{\alpha^2 m_{e_i}^2}{(m_c^*)^2}\right] + \mathcal{O}\left\{\frac{\alpha m_{e_i}^2}{m_{\mathbf{H}}^2 [k_i^{(e)} N_0]^4}\right\} \\ & + \mathcal{O}\left[\frac{m_{e_i}^6}{(m_c^*)^6}\right] + \mathcal{O}\left\{\frac{m_{e_i}^2}{m_{\mathbf{H}}^2 [k_i^{(e)}]^4 N_0^5}\right\} \\ & + \mathcal{O}\left\{\frac{m_{e_i}^4}{m_{\mathbf{H}}^4 [k_i^{(e)} N_0]^4}\right\}. \end{aligned} \quad (124)$$

6. Corrections to $[K_e(\theta_e)]^4$ from the muon channel

In the above it has been assumed that $K_e(\theta_e)$ attracts corrections from the tau channel only, corresponding to projection of $K_e(\theta_e)$ onto its $v_3 v_3^\dagger$ component (94). However, the term $[1 + \Delta_e(m_{e_i})]$ in Eq. (96) corrects all masses m_{e_i} and thus also affects the $v_1 v_1^\dagger$ and $v_2 v_2^\dagger$ components.

Also note that a propagating fermion undergoes multiple scatterings off the background fields. These scatterings may impart energy to or take energy from the fermion. They are generally ignored as their average contributions vanish over length scales large compared with \mathcal{L}_0 , but at any instant they may impart energy to the fermion in the range $-\mathcal{E}_\Omega$ to $+\mathcal{E}_\Omega$. In conjunction with this, background field interactions may also transiently modify the relative phases and amplitudes of the fermion's three constituent preons.

In consequence, although in the low-energy (large probe) limit a fermion occupies a definite eigenstate of the net mass matrix, at any given interaction a fermion with energy small compared with \mathcal{E}_Ω (corresponding, close to the isotropy frame, to rest mass close to $\mathcal{E}_\Omega c^{-2}$) will, in general, be arbitrarily off-shell in a quasi-random superposition of eigenstates. Such a fermion therefore attracts corrections from all eigensectors of $K_e(\theta_e)$.

To evaluate the correction arising from the e_2 or muon channel, recognise from Eqs. (93–94) that the effect of this correction is in opposition to the tau correction, and increases the magnitude of θ_e . As its scale is seen from Eq. (97) to be small compared with the tau correction, and from the construction of Eq. (105) it is seen to act in direct opposition to the tau correction, its effects are conveniently represented at energy scale \mathcal{E} by subtracting the muon correction from the tau correction at the level of the interaction diagrams. This yields

$$\theta_e(\mathcal{E}) = -\frac{3\pi}{4} \left(1 - \frac{4\sqrt{\delta_e\{r[\Delta_e(m_\tau, \mathcal{E}) - \Delta_e(m_\mu, \mathcal{E})]\}}}{3\pi} \right) \quad (125)$$

where $\theta_e(\mathcal{E})$ is the effective value of θ_e experienced by a particle whose energy is \mathcal{E} (i.e. if at rest, a particle with

rest mass $\mathcal{E}c^{-2}$), and henceforth all instances of θ_e are acknowledged to depend, either explicitly or implicitly, on a particle's energy scale \mathcal{E} .

The correction from the e_1 or electron channel is smaller, but not negligible at the level of precision employed in this paper. However, introducing this correction results in an electron rest mass which runs with energy scale, including when the electron is in motion with respect to the isotropy frame. It is desirable that the electron rest mass behave as a fixed reference point which can be calibrated against experimental observation independent of electron velocity in the isotropy frame, allowing it to be consistent with observation and to be taken as one of the input parameters of the model. Therefore, before addressing the electron channel correction to $K_e(\theta_e)$, it is first necessary to revisit the local scaling symmetry discarded in Sec. III C 1 of Paper III.

7. Local scaling symmetry

As noted above, recognise that regardless of whether the mass is evaluated through the series in $\Delta_e(m_e)$, or whether θ_e is redefined to absorb the $[\Delta_e(m_e)]^2$ term in m_τ^2 , the value of θ_e necessarily runs with energy scale, and thus so too do the values of the colour mixing matrix eigenvalues $k_i^{(e)}$, and hence all lepton masses. This is undesirable if the model is to emulate the observable universe, in which electron rest mass is frame-independent. This issue with the model may be addressed by revisiting the discussion of local scaling symmetry.

In Sec. III C 1 of Paper III it was stated that global scaling symmetry was broken by the introduction of a pseudovacuum with definite energy scale \mathcal{E}_0 . However, an alternative perspective now proves more fruitful: On the introduction of any nonvanishing vacuum excitations, let the scaling degree of freedom associated with symmetry subgroup

$$\mathbf{1}_A \otimes \mathbf{1}_C \otimes \mathbb{R}^+ \quad (126)$$

be gauged such that on average, over regions of some length scale $O(\mathcal{L}_0)$, the electron mass is constant. Since the electron mass is a function of the background photon energy scale, this largely corresponds to requiring that the average energy scale of the pseudovacuum (\mathcal{E}_0) is constant, at least in the presence of first-generation particles close to rest in the isotropy frame of the pseudovacuum. The assumption of maximum entropy of the pseudovacuum then ensures that $\mathcal{L}_0 = \mathcal{E}_0^{-1}$, and that the net spacetime dilation factor is homogeneous and undetectable at probe scales large compared with \mathcal{L}_0 .

Relative to this fixed reference value of m_e^2 , computation of the lepton mass ratios then corresponds to computation of the ratios of the eigenvalues of the pseudovacuum mass coupling. Now that there are multiple energy scales involved, it is advisable to be more careful with notation. Noting that a lepton may be off-shell (or in

motion) and thus its energy scale \mathcal{E} may not coincide with $m_{e_i}c^2$, therefore write

$$m_{e_i}^2(\mathcal{E}) = \frac{f^2}{2} \left[k_i^{(e)}(\mathcal{E}) \right]^4 \omega_0^2 N_0^8 S_{18,147} C_{\alpha, N_0} \times [1 + \Delta_e(m_{e_i}, \mathcal{E})] [1 + \mathcal{O}_e(m_{e_i})] \quad (127)$$

$$\Delta_e(m_{e_i}, \mathcal{E}) = \frac{90\alpha m_{e_i}^2}{\pi [m_c^*(\mathcal{E})]^2} + \frac{(5 - 4f_Z)\alpha m_{e_i}^2}{2\pi m_W^2} \quad (128)$$

$$+ \frac{5m_{e_i}^2}{[m_c^*(\mathcal{E})]^2} \left[1 + \frac{90\alpha m_{e_i}^2}{\pi [m_c^*(\mathcal{E})]^2} + \frac{(25 - 12f_Z)\alpha m_{e_i}^2}{6\pi m_W^2} \right]$$

$$+ \frac{40m_{e_i}^2}{3m_H^2 \left[k_i^{(e)}(\mathcal{E}) N_0 \right]^4}$$

$$[m_c^*(\mathcal{E})]^2 = m_c^2 \left(1 - \frac{27}{10} \frac{\mathcal{E}^2}{m_c^2 c^4} \right) \quad (129)$$

$$\theta_e(\mathcal{E}) = -\frac{3\pi}{4} \left(1 - \frac{4\sqrt{\delta_e} \{ r[\Delta_e(m_\tau, \mathcal{E}) - \Delta_e(m_\mu, \mathcal{E})] \}}{3\pi} \right) \quad (130)$$

$$k_n^{(e)}(\mathcal{E}) = 1 + \sqrt{2} \cos \left[\theta_e(\mathcal{E}) - \frac{2\pi(n-1)}{3} \right]. \quad (131)$$

where previous occurrences of these parameters in Secs. V C 3–V C 5 are noted to implicitly be dependent on energy scale, e.g.

$$\Delta_e(m_\tau) \longrightarrow \Delta_e(m_\tau, m_\tau c^2) \quad (132)$$

for an on-shell tau close to rest in the isotropy frame.

Calculation of higher-generation masses then corresponds to identification of energy scales \mathcal{E}_{e_i} at which Eqs. (127–131) are simultaneously consistent for rest mass $m_{e_i}c^2 = \mathcal{E}_{e_i}$, taking into account the correction to $\theta_e(\mathcal{E})$ discussed in Sec. V C 5 and the running of all parameters with energy. Prior to gauging of the scaling symmetry (126), the electron rest mass satisfies

$$m_e^2 = \frac{f^2}{2} \left[k_1^{(e)}(\mathcal{E}) \right]^4 \omega_0^2 N_0^8 S_{18,147} C_{\alpha, N_0} \times [1 + \Delta_e(m_e, \mathcal{E}) + \dots] [1 + \mathcal{O}_e(m_e)] \quad (133)$$

and runs with energy, but fixing a gauge to hold m_e^2 constant then corresponds to a rescaling of ω_0 such that the product $[k_1^{(e)}]^4 \omega_0^2$ remains fixed. Denoting the scaling field $\kappa(\mathcal{E})$, the electron mass becomes

$$m_e^2 = \frac{f^2}{2} \left[k_1^{(e)}(\mathcal{E}) \right]^4 [\kappa(\mathcal{E}) \omega_0]^2 N_0^8 S_{18,147} C_{\alpha, N_0} \times [1 + \Delta_e(m_e, \mathcal{E}) + \dots] [1 + \mathcal{O}_e(m_e)]. \quad (134)$$

which is constant by definition of $\kappa(\mathcal{E})$. The general lepton mass at energy \mathcal{E} then becomes

$$m_{e_i}^2(\mathcal{E}) = \frac{f^2}{2} \left[k_i^{(e)}(\mathcal{E}) \right]^4 [\kappa(\mathcal{E}) \omega_0]^2 N_0^8 S_{18,147} C_{\alpha, N_0} \times [1 + \Delta_e(m_{e_i}, \mathcal{E}) + \dots] [1 + \mathcal{O}_e(m_{e_i})]. \quad (135)$$

Changes in energy scale modulate the ratio

$$\frac{k_i^{(e)}(\mathcal{E})}{k_1^{(e)}(\mathcal{E})} \quad (136)$$

and thus modulate $m_{e_i}^2/m_e^2$, while choice of gauge keeps m_e^2 unchanged. Valid ratios (136) directly yield consistency of Eqs. (128–131) and (135). For definiteness, let $\kappa(\mathcal{E}_e) = 1$.

The search for consistent ratios is much simplified by writing

$$\frac{m_{e_i}^2}{m_e^2} = \frac{\left[k_i^{(e)}(\mathcal{E}_{e_i})\right]^4 [1 + \Delta_e(m_{e_i}, \mathcal{E}_{e_i})]}{\left[k_1^{(e)}(\mathcal{E}_{e_i})\right]^4 [1 + \Delta_e(m_e, \mathcal{E}_{e_i})]}, \quad (137)$$

regarding which, note the following:

- Identification of a mass eigenstate corresponds to identification of an eigenvalue ratio *at a particular energy scale* which yields consistency of Eqs. (128–131) and (135). Thus the energy scale is \mathcal{E}_{e_i} in both the numerator and the denominator.
- The electron mass is a constant of the model, with $\kappa(\mathcal{E}_{e_i})$ offsetting the energy dependency of $k_1^{(e)}(\mathcal{E}_{e_i})$ and $\Delta_e(m_e, \mathcal{E}_{e_i})$ in Eq. (135).
- Conveniently, on evaluating numerator and denominator at a common energy scale, gauge parameter $\kappa(\mathcal{E}_{e_i})$ is identical in numerator and denominator and thus does not appear in Eq. (137).

8. Corrections to $[K_e(\theta_e)]^4$ from the electron channel

Having addressed frame and energy scale invariance of m_e^2 , the correction to $K_e(\theta_e)$ from the e_1 or electron channel may now be determined. This channel is seen from Eq. (92) to contribute purely to the real part of $[K_e(\theta_e)]_{12}$. For the imaginary part, all positive contributions to the imaginary portion of $[K_e(\theta_e)]_{12}$ arise from the muon channel and all negative contributions from the tau channel, enabling the relatively simple form of Eq. (125). In contrast, while the electron channel contributes to the real part of $[K_e(\theta_e)]_{12}$ the bulk of the real part arises instead from the muon and tau channels. (Indeed, for $\theta_e := -3\pi/4$ the entirety of the real part arises from the muon and tau channels, though the corrections from the tau and mu sectors already discussed ensure that this particular situation is avoided.)

Let the electron mass undergo a rescaling $m_e^2 \rightarrow m_e^2[1 + \Delta_e(m_e, \mathcal{E})]$, resulting in some rescaling $(1 + \varepsilon)$ of $k_1^{(e)}(\mathcal{E})$. As the real and imaginary components of $\exp(i\theta_e)$ are both negative, the increase in the real component of $[v_1 v_1^\dagger]_{12}$ associated with this correction will decrease the magnitude of θ_e . However, by choice of gauge

in Sec. VC7 the electron mass is one of the fixed input parameters to the model, and consequently this rescaling (and its associated effect on θ_e) must be offset by a decrease in magnitude of the associated energy scale \mathcal{E}_0 {and thus of $[m_e^{(0)}]^2$ } corresponding to multiplication by $(1 + \varepsilon)^{-1}$. If this value is pulled out as an independent factor, in the electron mass diagram it cancels with the $(1 + \varepsilon)$ arising from the electron mass rescaling, leaving m_e and $k_1^{(e)}(\mathcal{E})$ unchanged (and eliminating any need to evaluate colour effects from this sector). However, for the muon and the tau it may be seen as a rescaling of $k_2^{(e)}(\mathcal{E})$ or $k_3^{(e)}(\mathcal{E})$ respectively by a factor of $(1 + \varepsilon)^{-1}$. To elucidate the effect of this scaling factor on θ_e , restore colour neutrality by likewise holding the muon and tau masses fixed, corresponding to enacting a transformation

$$k_i^{(e)}(\mathcal{E}) \rightarrow k_i^{(e)}(\mathcal{E}) (1 + \varepsilon) \quad | \quad i \in \{2, 3\}. \quad (138)$$

The leading colour effect arising from this transformation is equivalent to a rescaling of $k_3^{(e)}(\mathcal{E})$ (which generates the leading correction to θ_e) by $(1 + \varepsilon)$ and is therefore associated with an *increase* in the magnitude of θ_e . The rescaling of the muon term is by the same factor. This multiplier is independent of the existing muon and tau corrections, having its origins on the real rather than the imaginary portion of $[K_e(\theta_e)]_{12}$, and therefore must be evaluated as a separate correction to $\theta_e := -3\pi/4$ rather than being conflated into a single term (as was possible for the muon and tau channels by their linearity on the imaginary component). In effect this correction acts on both the muon and the tau channel to yield

$$\theta_e(\mathcal{E}) = -\frac{3\pi}{4} \left(1 - \frac{4\sqrt{\delta_e}\{r[\Delta_e(m_\tau, \mathcal{E}) - \Delta_e(m_\mu, \mathcal{E})]\}}{3\pi} \right) \times \left(1 + \frac{4\sqrt{\delta_e}\{r[\Delta_e(m_e, \mathcal{E})]\}}{3\pi} \right). \quad (139)$$

This completes corrections to $\theta_e(\mathcal{E})$ at the level of precision employed in the present paper, with the form of $\theta_e(\mathcal{E})$ chosen to avoid the need for corrections to Eq. (127) at $\mathcal{O}\{\Delta_e(m_{e_i}, \mathcal{E})^2\}$.

VI. PREDICTIONS OF THE $\mathbb{C}^{\wedge 18}$ ANALOGUE MODEL

A. Mass relationships

As seen in the above exploration of the $\mathbb{C}^{\wedge 18}$ analogue model, the increased structure of the $\mathbb{C}^{\wedge 18}$ free field model as compared with the Standard Model provides for complex interrelationships between the particle masses. When these relationships are collected together, it transpires that it suffices to take three input parameters from

$$\alpha, m_e, m_\mu, m_\tau, m_W, m_Z, m_H \quad (140)$$

with the remaining four parameters then being derived quantities. It is, therefore, an obvious test of the $\mathbb{C}^{\wedge 18}$ model to evaluate these derived quantities. As seen in Sec. VIB, the calculated quantities are in such excellent agreement with observation that this goes beyond being

a test of the reasonableness of the $\mathbb{C}^{\wedge 18}$ analogue model, and becomes an application of the model.

To obtain these predictions, combine the mass equations for the various particle species developed above, and explicitly expand $S_{6,13}$ and $S_{18,147}$ to yield the relationships

$$\frac{m_{e_i}^2}{m_e^2} = \frac{[k_i^{(e)}(\mathcal{E}_{e_i})]^4 [1 + \Delta_e(m_{e_i}, \mathcal{E}_{e_i})]}{[k_1^{(e)}(\mathcal{E}_{e_i})]^4 [1 + \Delta_e(m_e, \mathcal{E}_{e_i})]} [1 + \mathcal{O}_e(m_{e_i}, \mathcal{E}_{e_i})] \quad \left| \quad e_i \in \{e, \mu, \tau\} \right. \quad (137)$$

$$\frac{m_W^2}{m_e^2} = 18N_0^4 \left(1 + \frac{2}{N_0}\right)^4 \left(1 + \frac{1}{N_0}\right)^4 \frac{\left[1 + \left(64 + \frac{3}{2\pi} - f_Z\right) \frac{\alpha}{2\pi}\right] \left\{1 + \frac{19}{18[k_1^{(e)}(\mathcal{E}_e) N_0]^4}\right\} \left(1 + \frac{3\alpha}{2\pi}\right)}{[1 + \Delta_e(m_e, \mathcal{E}_e)] \left[1 + \frac{3\alpha}{2\pi} \left(1 + \frac{8}{9N_0}\right)\right]} [1 + \mathcal{O}_b + \mathcal{O}_e(m_e, \mathcal{E}_e)] \quad (141)$$

$$\frac{m_W^2}{m_Z^2} = \frac{3 \left[1 + \left(64 + \frac{3}{2\pi} - f_Z\right) \frac{\alpha}{2\pi}\right] \left\{1 + \frac{19}{18[k_1^{(e)}(\mathcal{E}_e) N_0]^4}\right\}}{4 \left[1 + \left(\frac{401}{12} + \frac{3}{2\pi}\right) \frac{\alpha}{2\pi}\right] \left\{1 + \frac{23}{18[k_1^{(e)}(\mathcal{E}_e) N_0]^4}\right\}} (1 + \mathcal{O}_b) \quad \frac{m_W^2}{m_c^2} = \frac{1 + \frac{19}{18[k_1^{(e)}(\mathcal{E}_e) N_0]^4}}{1 + \frac{99}{18[k_1^{(e)}(\mathcal{E}_e) N_0]^4}} (1 + \mathcal{O}_b) \quad (142)$$

$$\frac{m_W^2}{m_H^2} = \frac{9 \left[1 + \left(64 + \frac{3}{2\pi} - f_Z\right) \frac{\alpha}{2\pi}\right] \left\{1 + \frac{19}{18[k_1^{(e)}(\mathcal{E}_e) N_0]^4}\right\}}{20 \left\{\left(1 - \frac{1}{9N_0}\right)^2 \left[1 + \frac{30\alpha}{9\pi} \left(1 + \frac{1}{9N_0}\right)\right] + \frac{1}{2\pi} \left[1 + \frac{30\alpha}{\pi} \left(1 - \frac{1}{9N_0}\right)\right]\right\} \left\{1 + \frac{7}{18[k_1^{(e)}(\mathcal{E}_e) N_0]^4}\right\}} (1 + \mathcal{O}_b) \quad (143)$$

$$\Delta_e(m_{e_i}, \mathcal{E}) = \frac{90\alpha m_{e_i}^2}{\pi [m_c^*(\mathcal{E})]^2} + \frac{(5 - 4f_Z)\alpha m_{e_i}^2}{2\pi m_W^2} + \frac{5m_{e_i}^2}{[m_c^*(\mathcal{E})]^2} \left[1 + \frac{90\alpha m_{e_i}^2}{\pi [m_c^*(\mathcal{E})]^2} + \frac{(25 - 12f_Z)\alpha m_{e_i}^2}{6\pi m_W^2}\right] + \frac{40m_{e_i}^2}{3m_H^2 [k_i^{(e)}(\mathcal{E}) N_0]^4} + \mathcal{O}_e(m_{e_i}, \mathcal{E}_{e_i}) \quad (128)$$

$$\theta_e(\mathcal{E}) = -\frac{3\pi}{4} \left(1 - \frac{4\sqrt{\delta_e\{r[\Delta_e(m_\tau, \mathcal{E}) - \Delta_e(m_\mu, \mathcal{E})]\}}}{3\pi}\right) \left(1 + \frac{4\sqrt{\delta_e\{r[\Delta_e(m_e, \mathcal{E})]\}}}{3\pi}\right) \quad (139)$$

$$f_Z = \frac{1}{3} \left(4 - 24 \frac{m_W^2}{m_Z^2} + 16 \frac{m_W^4}{m_Z^4}\right) \quad (26)$$

$$[m_c^*(\mathcal{E})]^2 = m_c^2 \left(1 - \frac{27}{10} \frac{\mathcal{E}^2}{m_c^2 c^4}\right) \quad (129)$$

$$\mathcal{E}_\ell = m_\ell c^2 \quad (144)$$

$$r(n) = n \cdot \sqrt{1 - \frac{n}{9}} \quad (123)$$

$$k_n^{(\ell)}(\mathcal{E}) = 1 + \sqrt{2} \cos \left[\theta_\ell(\mathcal{E}) - \frac{2\pi(n-1)}{3} \right] \quad (145)$$

$$\delta_e(n) = \sqrt{1 + \frac{\pi^2 n}{8} \left[1 + \frac{\pi^2 n}{32}\right]} - 1 + \mathcal{O}(n^3) \quad (146)$$

$$\mathcal{O}_b = \mathcal{O} \left\{ \frac{\alpha}{\pi} [k_1^{(e)}(\mathcal{E}_e) N_0]^{-4} \right\} + \mathcal{O} \left(\frac{\alpha^2}{\pi^2} \right) \quad (147)$$

$$\begin{aligned} \mathcal{O}_e(m_{e_i}, \mathcal{E}) = & \mathcal{O}\left(\frac{\alpha}{\pi N_0^2}\right) + \mathcal{O}\left(\frac{\alpha^2}{\pi^2 N_0}\right) + \mathcal{O}\left[\frac{\alpha m_{e_i}^2}{\pi N_0 [m_c^*(\mathcal{E})]^2}\right] + \mathcal{O}\left\{\frac{\alpha^2 m_{e_i}^2}{\pi^2 [m_c^*(\mathcal{E})]^2}\right\} + \mathcal{O}\left\{\frac{\alpha m_{e_i}^2}{\pi m_{\mathbf{H}}^2 [k_i^{(e)}(\mathcal{E}) N_0]^4}\right\} \\ & + \mathcal{O}\left\{\frac{m_{e_i}^6}{[m_c^*(\mathcal{E})]^6}\right\} + \mathcal{O}\left\{\frac{m_{e_i}^2}{m_{\mathbf{H}}^2 [k_i^{(e)}(\mathcal{E})]^4 N_0^5}\right\} + \mathcal{O}\left\{\frac{m_{e_i}^4}{m_{\mathbf{H}}^4 [k_i^{(e)}(\mathcal{E}) N_0]^4}\right\}. \end{aligned} \quad (148)$$

Note that $r(n)$ is taken to be exact by definition. The finite length of the series in n is associated with an error in the lepton masses, but this is incorporated into $\mathcal{O}_e(m_{e_i}, \mathcal{E}_i)$.

B. Results

Taking m_e , m_μ , and α as input parameters [20, 21],

$$m_e = 0.5109989461(31) \text{ MeV}/c^2 \quad (149)$$

$$m_\mu = 105.6583745(24) \text{ MeV}/c^2 \quad (150)$$

$$\alpha = 7.2973525693(11) \times 10^{-3}, \quad (151)$$

the relationships of Sec. VI A may be solved numerically to yield the results given in Table V. The calculated values obtained for fundamental constants m_W , m_Z , $m_{\mathbf{H}}$, and m_τ are all within $0.1 \sigma_{\text{exp}}$ of the experimental results. For a discussion of the numerical methods used to solve the equations of Sec. VI A, see Appendix C.

For purpose of comparing the scale of terms in $\mathcal{O}_e(m_{e_i}, \mathcal{E})$, it is noted that the value of $k_1^{(e)}(\mathcal{E}_e)$ evaluates as

$$k_1^{(e)}(\mathcal{E}_e) = 0.0403500 \dots \quad (152)$$

For purpose of considering the breakdown scale of the $\mathbb{C}^{\wedge 18}$ analogue model, in a gauge in which $\kappa(\mathcal{E}) = 1$ it follows that

$$\mathcal{E}_\Omega^2 = \frac{N_0^4 m_e^2}{2\alpha(N_0 - \frac{1}{2})^2 [k_1^{(e)}]^4} [1 + \mathcal{O}(\alpha)]. \quad (153)$$

This is evaluated more precisely in Appendix D and gives a UV cutoff of ± 6.2 TeV.

For completeness it is also interesting to note the value of f , which also evaluated in Appendix D and is found to satisfy

$$f^2 = \frac{2\alpha}{N_0^6 S_\alpha (1 + a_e)^2} \quad (154)$$

$$f = 1.669584(99) \times 10^{-8}. \quad (155)$$

C. Sources of numerical error

The relationships between the fundamental constants presented in Sec. VI A incorporate numerous truncations. These are listed in Table VI, with their impacts on the numerical results being presented in Table VII. In determining the error bars on the results of Table V, all sources of error have been assumed independent. No attempt has been made to quantify exactly how large the next-order corrections E1-E14 are; instead, a generous coefficient of ± 10 has been applied to each term. It is expected this will over-estimate the higher-order corrections.

VII. CONCLUSION TO PART VI

The $\mathbb{C}^{\wedge 18}$ analogue model has many elements in common both with the Standard Model of particle physics and with the observable universe. As it has only three tunable parameters, which must be set by reference to physical constants, the $\mathbb{C}^{\wedge 18}$ analogue model may readily be tested against observation.

In the present paper, calculation of higher-order terms in the mass relationships of the $\mathbb{C}^{\wedge 18}$ model permitted the values of four fundamental constants, the masses of

TABLE V. Calculated values of particle masses in the $\mathbb{C}^{\wedge 18}$ analogue model. Quantity m_c is the bare gluon mass, which is not observable at the confinement scale but enters some calculations in this paper as a collective property of momentum transfer in the colour sector. The notation σ_{exp} corresponds to the uncertainty in the observed values of the particle masses.

Parameter	Calculated value (GeV/ c^2)	Observed value (GeV/ c^2)	Discrepancy
m_τ	1.7768715(2) ^a	1.77686(12)	$0.1 \sigma_{\text{exp}}$
m_W	80.3784(24)	80.379(12)	$0.05 \sigma_{\text{exp}}$
m_Z	91.1875(37)	91.1876(21)	$0.04 \sigma_{\text{exp}}$
$m_{\mathbf{H}}$	125.2498(51)	125.25(17)	$0.001 \sigma_{\text{exp}}$
m_c	80.4280(10)	—	—

^a Limited by precision of numerical solver

the W boson, Z boson, Higgs boson, and tau particle, to be predicted with precision comparable to current experimental observation. The results were found to be in perfect agreement to the limits of experimental precision.

The conceptual underpinnings of the $\mathbb{C}^{\wedge 18}$ analogue model are radically different to those of the Standard Model, being a classical model on anticommuting coordinates which only emulates a quantum field theory on pseudo-Riemannian space–time in an appropriate regime. Nevertheless, this paper provides an extremely compelling case for the utility of this analogue model.

Other predictions of the $\mathbb{C}^{\wedge 18}$ model include a “neutral gluon” N_μ , which is a dark matter candidate with a mass of $80.4280(10) \text{ GeV}/c^2$, and a second and third generation of weak bosons, with the first being a W -analogue at approximately 17 TeV. In view of the model’s ability to successfully derive the masses of known particles to full experimental precision, perhaps these predictions should be taken seriously.

The model also exhibits two further particles, weakly-interacting right-handed weak bosons denoted G_μ and G_μ^\dagger . However, detection of these particles should not be anticipated as they are eliminated in the final paper of this series [9], in which the $\mathbb{C}^{\wedge 18}$ analogue model is also shown to reproduce gravitational metric consistent with General Relativity—again, in an appropriate regime.

Finally, it is exciting to ask: What *is* the domain of validity of the $\mathbb{C}^{\wedge 18}$ model? The existence of a finite ultraviolet cutoff at $\mathcal{E}_\Omega = 6.2 \text{ TeV}$ suggests that experi-

ments at the Large Hadron Collider have entered a regime where they may probe the limits of the model, but effects identified thus far are subtle, and discrimination between the $\mathbb{C}^{\wedge 18}$ analogue model and the Standard Model is challenging. Nevertheless, the identification of tests capable of discriminating between these two models is highly desirable, as with the elimination of the $G_\mu^{(\dagger)}$ bosons forthcoming in Ref. [9], the $\mathbb{C}^{\wedge 18}$ model has greater predictive capacity than the Standard Model, and as yet, no domains have been identified in which it is demonstrably inferior as a description of the observable universe. However, extensive further assessment is required to determine whether the $\mathbb{C}^{\wedge 18}$ model is capable of acting as a model of the observable universe in its own right, or simply an analogue model whose limitations of validity have not yet been fully determined.

VIII. INTRODUCTION TO PART VII

Introduced in Refs. [1–5, 22], the $\mathbb{C}^{\wedge 18}$ analogue model is a classical model on a manifold with anticommuting coordinates which is capable of supporting a quasiparticle spectrum analogous to the Standard Model. Manifold $\mathbb{C}^{\wedge 18}$ is taken to support an infinite number of scalar fields, and on mapping a subspace $M \subset \mathbb{C}^{\wedge 18}$ onto $\mathbb{R}^{1,3}$,

$$\mathcal{G}(M) \cong \mathbb{R}^{1,3}, \quad (156)$$

the product of these fields behaves (in appropriate limits) as a pseudovacuum. Solitonic excitations about the pseudovacuum state then behave as preonic quasiparticles from which the species of the Standard Model are constructed. These are necessarily supplemented by a weakly-interacting massive vector boson denoted N_μ , higher-generation counterparts to the weak sector bosons (starting with W_2 at $17 \text{ TeV}/c^2$), and an attenuated right-handed weak interaction mediated by a pair of bosons denoted G_μ and G_μ^\dagger .

An essential part of relating the $\mathbb{C}^{\wedge 18}$ analogue model to the Standard Model is the choice of a gauge on the local symmetry of the analogue model, described in Sec. III C 6 of Paper III. The local symmetries which are gauged are an emergent property of the model arising in the limit of low quasiparticle energy, and originate in the freedom to choose an arbitrary co-ordinate frame on manifold $\mathbb{C}^{\wedge 18}$. Of the gaugeable degrees of freedom described in Sec. III C 1 of Paper III, the vast majority are fixed in Papers III and VI on physically motivated grounds. The sole exception is the gauging of the $\mathbf{1}_A \otimes \mathbf{1}_C \otimes \text{SL}(2, \mathbb{C})$ subgroup associated with the space–time connections on $\mathcal{G}(M)$. These connections are fixed (up to a change of co-ordinates on a fixed manifold) by requiring, arbitrarily, that the target of mapping \mathcal{G} in Paper III be flat.

In the present paper it is seen that relaxation of this requirement, such that the target of mapping \mathcal{G} need only be locally Minkowski, permits a choice of gauge on

TABLE VI. List of sources of error in the results of Table V. Note that coefficients of \mathcal{O}_b are assumed to vary independently in each of the boson masses, and hence in each of the listed mass ratios.

Label	Description
E1	Term 1 of \mathcal{O}_b applied to m_c^2/m_W^2
E2	Term 2 of \mathcal{O}_b applied to m_c^2/m_W^2
E3	Term 1 of \mathcal{O}_b applied to m_W^2/m_Z^2
E4	Term 2 of \mathcal{O}_b applied to m_W^2/m_Z^2
E5	Term 1 of \mathcal{O}_b applied to m_W^2/m_H^2
E6	Term 2 of \mathcal{O}_b applied to m_W^2/m_H^2
E7	Term 1 of \mathcal{O}_e applied to $\Delta_e(m_{e_i}, \mathcal{E})$
E8	Term 2 of \mathcal{O}_e applied to $\Delta_e(m_{e_i}, \mathcal{E})$
E9	Term 3 of \mathcal{O}_e applied to $\Delta_e(m_{e_i}, \mathcal{E})$
E10	Term 4 of \mathcal{O}_e applied to $\Delta_e(m_{e_i}, \mathcal{E})$
E11	Term 5 of \mathcal{O}_e applied to $\Delta_e(m_{e_i}, \mathcal{E})$
E12	Term 6 of \mathcal{O}_e applied to $\Delta_e(m_{e_i}, \mathcal{E})$
E13	Term 7 of \mathcal{O}_e applied to $\Delta_e(m_{e_i}, \mathcal{E})$
E14	Term 8 of \mathcal{O}_e applied to $\Delta_e(m_{e_i}, \mathcal{E})$
E15	The next term in $\delta_e(n)$
E16	Uncertainty in α
E17	Uncertainty in m_e
E18	Uncertainty in m_μ

TABLE VII. Contributions of different sources of error to the results of Table V, expressed in units of energy, and relative to the experimental error. Labels are enumerated in Table VI. For purposes of summation, sources of error are assumed independent.

Label	Coefficient	Uncertainty in		Uncertainty in		Uncertainty in		Uncertainty in		Uncertainty in	
		τ mass ^a		Z mass		W mass		\mathbf{H} mass		c mass	
		eV/c ²	10 ⁻⁴ σ_{exp}	MeV/c ²	σ_{exp}	MeV/c ²	σ_{exp}	MeV/c ²	10 ⁻² σ_{exp}	MeV/c ²	
E1	± 10	5.4	0.45	0.29	0.14	0.26	0.02	0.40	0.24	0.00	
E2	± 10	7.4	0.61	2.46	1.17	2.16	0.18	3.37	1.98	0.01	
E3	± 10	7.1	0.59	0.29	0.14	0.00	0.00	0.00	0.00	0.00	
E4	± 10	8.9	0.74	2.46	1.17	0.00	0.00	0.01	0.00	0.00	
E5	± 10	8.5	0.71	0.00	0.00	0.00	0.00	0.40	0.24	0.00	
E6	± 10	9.2	0.77	0.00	0.00	0.00	0.00	3.38	1.99	0.00	
E7	± 10	0.0	0.00	0.00	0.00	0.00	0.00	0.00	0.00	0.00	
E8	± 10	9.7	0.81	0.00	0.00	0.00	0.00	0.00	0.00	0.00	
E9	± 10	61.5	5.13	1.06	0.50	0.93	0.08	1.46	0.86	0.93	
E10	± 10	24.9	2.08	0.47	0.23	0.42	0.03	0.65	0.38	0.42	
E11	± 10	9.0	0.75	0.02	0.01	0.02	0.00	0.03	0.02	0.02	
E12	± 10	3.5	0.29	0.02	0.01	0.02	0.00	0.03	0.02	0.02	
E13	± 10	11.2	0.94	0.05	0.03	0.05	0.00	0.07	0.04	0.05	
E14	± 10	8.3	0.69	0.00	0.00	0.00	0.00	0.00	0.00	0.00	
E15	1	8.4	0.70	0.01	0.01	0.01	0.00	0.02	0.01	0.01	
E16	± 1	0.1	0.01	0.00	0.00	0.00	0.00	0.00	0.00	0.00	
E17	± 1	34.1	2.84	0.00	0.00	0.00	0.00	0.00	0.00	0.00	
E18	± 1	40.9	3.41	0.00	0.00	0.00	0.00	0.00	0.00	0.00	
Total		89.8	7.49	3.69	1.76	2.41	0.20	5.07	2.98	1.02	

^a Values of uncertainty in the mass of the tau are at the limit of precision of the current numerical solver. They should be considered indicative rather than definitive.

$\mathbf{1}_A \otimes \mathbf{1}_C \otimes \text{SL}(2, \mathbb{C})$ which eliminates the $G_\mu^{(\dagger)}$ bosons (and also some other beyond-Standard-Model effects). Adopting this gauge uniquely fixes the geometry of $\mathcal{G}(M)$, and in the vicinity (but outside the Schwarzschild radius) of a nonrotating electrically neutral massive body this geometry is seen to correspond to the Schwarzschild metric. The Kerr metric for a rotating source is anticipated to follow in a similar regime from the usual classical arguments [23]. Further, the effective value of Newton's constant in this gravitational analogue is uniquely determined by the structure of the $\mathbb{C}^{\wedge 18}$ model and is found to be $G_N = 6.67427(240) \times 10^{-11} \text{ m}^3 \text{kg}^{-1} \text{s}^{-2}$, in excellent agreement with observation.

This is not the first attempt to calculate of the value of Newton's constant. Acknowledgement must be made of the efforts of Di Mario in a series of articles made available online from 2003 [24], whose equations reduce to the relationship

$$G_N = \frac{\alpha^2 \hbar^3 \omega_1^2}{4\pi c^3 m_e^4} [1 + \mathcal{O}(\alpha)]. \quad (157)$$

However, the parameter ω_1 in Eq. (157) is a unitful constant taking the value of exactly 1 s^{-1} , and the origin of this constant is never satisfactorily explained. This leaves the uncomfortable inference that the universe might have some special relationship with our arbitrarily-chosen unit

of time, and this equation must therefore be considered a remarkable coincidence. The present paper does not make any use of this factor ω_1 .

The structure of this paper is as follows: Section IX A recaps and references the conventions of notation and terminology employed in this paper. Section IX B then introduces a convenient relationship between Feynman diagrams and classical fields termed a *quantum/classical correspondence*. Sections X A and X B begin the mapping of beyond-Standard-Model effects to space-time curvature. The most ubiquitous interaction involving $G^{(\dagger)}$ bosons is identified as involving a spin-2 pair $G_\mu G_\nu^\dagger$, and elimination of this process (and other related beyond-Standard-Model processes) is compared with choosing a gauge in the low-energy regime. Calculation of the resulting metric is performed in Sec. X C, and is shown to be predictive of the value of Newton's constant. Section X D extends this treatment to include all sources of $G^{(\dagger)}$ bosons, including single-boson (spin-1) interactions. Numerical results are presented in Sec. XI A, with some discussion of implications in Sec. XI B, and the future of the $\mathbb{C}^{\wedge 18}$ model is discussed in Sec. XII.

IX. CONVENTIONS

A. Notation and terminology

This paper follows the same conventions as Refs. [1–5, 22], henceforth Papers I–VI respectively. As in previous papers, units are chosen such that $c = 1$, $\hbar = 2$. When equations and lemmas from Papers I–VI are referenced, they take the forms (I:1), (II:1), (II:A1), etc.

When referring to uncertainty in results, experimental uncertainties will be denoted σ_{exp} , and uncertainties in the theoretical calculation will be denoted σ_{th} .

In this paper, it is generally assumed that any particle under study is at rest or near-rest with respect to the isotropy frame of the pseudovacuum.

Regarding terminology around Feynman diagrams and symmetry factors:

- Where there exist multiple ways to connect up sources, vertices, and sinks to obtain equivalent diagrams up to interchange of non-distinguishable co-ordinates, the same term is obtained from the generator \mathcal{Z} in multiple different ways and thus the diagram acquires a multiplicative factor. This is referred to in the present paper series as a *symmetry factor*.
- Where integration over the parameters of a diagram (for example, over source/sink co-ordinates) yields the same diagram multiple times up to interchange of labels on these parameters, this represents a double- (or multiple-) counting of physical processes. It is then necessary to eliminate this multiple-counting by dividing by the appropriate symmetry factor. This is referred to in the present paper series as *diagrammatic redundancy* or *double- (multiple-) counting*.

B. Quantum/classical correspondence

In the limit of large particle numbers it is convenient to introduce a quantum/classical correspondence which permits classical field profiles to be obtained from the Feynman diagrams describing the processes taking place within these fields. As a specific example, consider the emission of a photon by an electron as shown in Fig. 22. Although a classical-regime A field is assumed to be made up of many, many virtual photons, these are all emitted in accordance with Fig. 22 and it is customary to associate features of this diagram with elements of the classical expression

$$A = \frac{Q}{|e|} \frac{\alpha}{r} \quad (158)$$

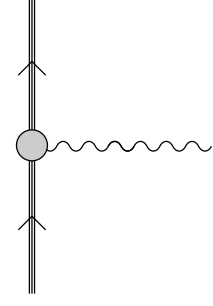


FIG. 22. Emission of a single photon by a single electron. The grey circle is the all-orders vertex incorporating loop corrections. The triple line represents the existence of a preonic substructure, consistent with Papers I–VI.

(in which only the source is associated with a factor of α) or with its symmetrised form

$$A = \frac{Q}{|e|} \frac{\sqrt{\alpha}}{r} \quad (159)$$

in which a factor of $\sqrt{\alpha}$ appears at both source and sink. To set up the quantum/classical correspondence used in the present paper:

- First, as is customary, associate the all-orders vertex in Fig. 22 with a factor of $\sqrt{\alpha}$, the classical electromagnetic field coupling. This is consistent with the quantum field theory treatment of Sec. III E 1 of Paper III, and in particular with Eq. (III:83). When a photon is exchanged between two charged particles, this coefficient is squared to yield α , and incorporates a factor of $1/(4\pi)$ which is associated with directionality of emission.
- Second, normalise the fermion fields such that the fermion line and associated operators (e.g. $\bar{e}_L \bar{\sigma}^\mu e_L$) may be identified as a number operator. This is to be understood in the sense that (for example) given a collection of fermions at rest, $\|\bar{e}_L \bar{\sigma}^\mu e_L\|$ counts the number of left-handed electrons per unit volume.
- Third, it is necessary to relate a single boson to a field profile. This is again a choice not just in the quantum/classical correspondence, but also in quantum field theory, and must reproduce the geometric factor of $1/r$ in Eq. (159). Thus the photon line emerging from the interaction vertex for a spherically symmetric point source, and hence the associated photon operator at that vertex, must be associated with a factor of r^{-1} . (It should be noted that this latter association applies only to radially propagating fields. In contrast, for example, the mean energy per photon of the background field is known to be $\omega_0 = \mathcal{E}_0/N_0$ everywhere.)

Having imposed this relationship between Feynman diagrams and classical fields, which is almost trivial in the

$\overline{\text{MS}}$ renormalisation scheme, it is now possible to use Feynman diagrams to calculate the profiles of classical fields in the presence of perturbing processes. The above three choices calibrate the electromagnetic 4-potential of a single electron against the emission diagram of Fig. 22, and application of the same calibration to the diagrams for other processes then permits determination of their effects on fields in the classical limit.

The remainder of this paper is essentially a calculation performed using the quantum/classical correspondence specified above, taking into account additional effects due to the presence of the pseudovacuum and the fundamental scalar field (FSF) symmetry factors.

X. $\mathbb{C}^{\wedge 18}$ WITH CURVED SPACE-TIME

A. Curvature and choice of gauge

As noted in the introduction, the choice of co-ordinate frame on the $\mathbf{1}_A \otimes \mathbf{1}_C \otimes \text{SL}(2, \mathbb{C})$ subgroup of $\text{GL}(18, \mathbb{C})$ is a freedom of the $\mathbb{C}^{\wedge 18}$ model. In choosing this frame the 4-volume form must be preserved under translations, as the scaling symmetry $\mathbf{1}_A \otimes \mathbf{1}_C \otimes \mathbb{R}^+$ is fixed in Sec. V C 7. Once a prescription has been described for choosing such a frame based on the field content of the model on $\mathbb{C}^{\wedge 18}$, the target of mapping \mathcal{G} must then be chosen to be able to support the associated metric, being the manifold on which the $\mathbb{C}^{\wedge 18}$ model emulates particle dynamics.

Recognising that all choices of gauge for local symmetries of the low-energy effective description of the $\mathbb{C}^{\wedge 18}$ model similarly correspond to choices of co-ordinate frame on $\mathbb{C}^{\wedge 18}$, it is natural to refer to this particular choice of co-ordinate frame in the same language, describing the degrees of freedom associated with this co-ordinate frame as gauge degrees of freedom, and the prescription for choosing the co-ordinate frame as being a choice of gauge.

B. Beyond-Standard-Model processes in the photon pair field

1. Origin of the photon pair field

The governing principle behind the choice of co-ordinate frame on $\text{SL}(2, \mathbb{C})$ is that it should eliminate as many beyond-Standard-Model effects as possible, including the $G^{(\dagger)}$ fields, and thus the right-handed weak interaction. As a first step, it is necessary to identify the most prevalent $G^{(\dagger)}$ -boson-mediated interactions appearing in the $\mathbb{C}^{\wedge 18}$ analogue model. These interactions take place within a photon pair field having no counterpart in the Standard Model.

As a prototype for fermionic matter, consider a collection of positrons and electrons with zero net spin and zero net charge (and see Sec. X B 3 for discussion of more general matter sources). Let this source emit a pair of

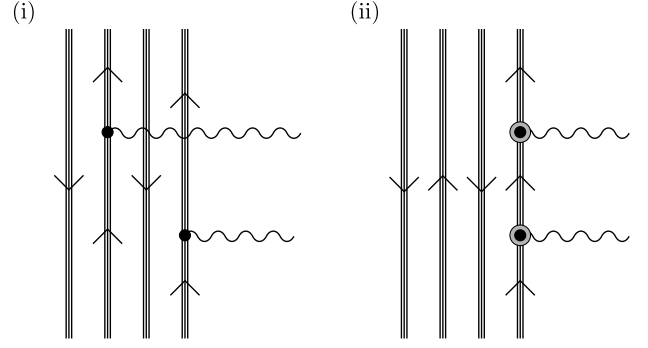


FIG. 23. Emission of a pair of photons, (i) with standard electromagnetic vertices, and (ii) with K -augmented vertices. In diagram (i), emission may be from any fermion or pair of fermions in the matter source. In diagram (ii), for the background interactions which give rise to the K matrices to be on average nonvanishing, emission of the pair must be from the same fermion.

photons as per Fig. 23(i), either with both being emitted from the same fermion, or with both being emitted from different fermions. There are precisely as many diagrams for emission of pairs from sources with charges of the same sign as there are for emissions of pairs from sources with different sign, and in the far field, being the regime in which all source elements may be treated as collocated, these diagrams cancel to yield no net photon pair field $A_\mu A_\nu$.

However, in the $\mathbb{C}^{\wedge 18}$ model there is a further emission channel to consider. In addition to the simple photon pair emission channel described above, if both sources are correlated and both vertices are within \mathcal{L}_0 of one another (with these conditions in practice implying that both emission vertices are on the same fermion) there is also a process of emission augmented by background colour field interactions.

In the mass calculations of Papers IV and VI it was convenient to separate the description of interactions with the background gluon fields into colourless boson couplings (implicitly exploiting symmetry of the C sector under colour mixing) and independent colour transformations (represented by K matrices), and then to write the effectively colourless gluon contributions to particle mass as small corrections to the photon contributions. This approach is once again useful here, although it is not the emission of the gluon pairs themselves which is important this time, since the gluons are (i) massive and (ii) confined. This time, it is the effects of these gluon interactions on preon colour (as represented by the K matrices) which are of interest, as these effects may be nonvanishing over length scales of up to $\mathcal{O}(\mathcal{L}_0)$. Physically these diagrams represent processes whereby preons scatter off background gluons one or more times to change colour, then scatter again to change back again, contemporaneous with the emission of a photon pair. The scattering process itself is absorbed into the normalisation of the fermion propagator, but the effects on preon colour pro-

vide physically distinguishable alternative channels for photon emission. The pair of background field scatterings must be correlated, and in matter of normal densities, this necessitates the involvement of the same fermion at each background interaction.

In principle these K matrices are associated with explicit gluon couplings as per Eq. (IV:25), but these explicit field couplings are subsumed into the fermion propagator as indicated in Fig. 4 of Paper IV, and hence into the fermion mass term. However, as per Sec. IIIB 2 of Paper IV, knowing that the application of K matrices is in 1:1 correspondence with A -sector interactions permits these matrices to be equivalently associated with the non-subsumed photon interaction vertices. Proper accounting for colour effects is then obtained if up to one set of K matrices is applied for every A -sector interaction (as discussed in Sec. IIIC of Paper IV), with the matrices being applied to the same fermion as participates in the A -sector interaction. (Applying the K matrices elsewhere has no effect on the emission process.) An example diagram for the resulting process is shown in Fig. 23(ii). As emission is constrained to always be of two photons from the same fermion, there is no cancellation of diagrams and a nonvanishing photon pair field is supported. In flat space-time, both the intensity of the foreground photon pair field $[A_\mu A_\nu]_{\text{fg}}$ and the number of pairs traversing unit area of a spherical shell scale as r^{-2} . This is a convenient feature of the photon pair field in the position basis, and provided all subsequent processes act equivalently on all photon pairs, it allows any relative (i.e. multiplicative) attrition of the field to be understood equivalently either in terms of a relative reduction in the field amplitude, or a relative reduction in the number of participating pairs.

2. Interactions of the photon pair field

Once a pair of foreground photons has been emitted by a matter source, that pair may propagate radially unchanged, or may undergo interactions. To understand these processes, it is helpful to study the behaviour of a photon pair on propagation across an infinitesimal interval $[r, r + dr)$. By requirement that the photon be capable of interacting, but that an infinitesimal interval be unsubdividable, each photon undergoes one interaction within such an interval. Free propagation is represented by treating the propagator term of the Lagrangian, $\frac{1}{2}A_\mu \Delta^{\mu\nu} A_\nu$, as a vertex. This is represented diagrammatically in Fig. 24.

In addition to the emission of foreground photon pair fields, a charged fermion necessarily also interacts with background photon pairs to yield the mass interactions discussed in Papers IV and VI. Figure 25(i) shows a pair of photons arising from the background field at a radius between r and $r + dr$ and propagating inward to interact with a fermion in the source. In general such diagrams make vanishingly small contributions to parti-

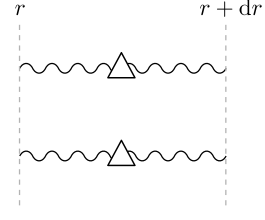


FIG. 24. Free propagation of a pair of photons across interval $[r, r + dr)$, with the propagator term of the Lagrangian represented as an interaction vertex Δ .

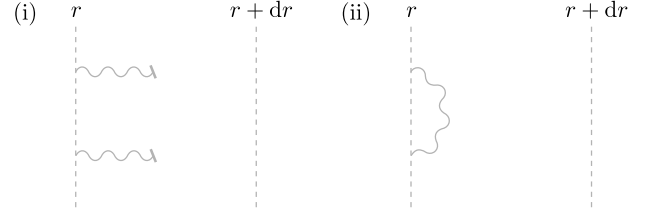


FIG. 25. (i) A pair of photons arising from the pseudovacuum in interval $[r, r + dr)$ propagates radially inward and interacts with a fermion in the matter source of the foreground photon pair field. The symbol \backslash denotes origin within the local pseudovacuum. (ii) The parent figure for diagram (i) reveals this to be the mean field expansion of a term in the Proper Self Energy (PSE) of the source fermion. Pseudovacuum photons are shown in grey.

cle mass for $r \gg \mathcal{L}_0$, but it must nevertheless be asked whether they contribute to the photon pair field at $r' < r$. This may be answered in the negative by considering emulation of foreground fields under the $\overline{\text{MS}}$ normalisation scheme, and recognising that Fig. 25(i) is the zeroth order term in the mean field expansion of Fig. 25(ii), which belongs to the Proper Self Energy (PSE) series of the source fermion. All such diagrams are accounted for in the renormalised foreground fermion propagator, and so may be discounted, as per Sec. III A of Paper IV.

It is next necessary to understand what further processes do take place within the propagating foreground photon pair field. A great many of these processes may be discounted for a wide variety of reasons, including the following:

- As in Fig. 25, any diagram which is itself part of the PSE series of the source fermion, or whose parent diagram is part of the PSE series of the source fermion, may be discounted as (regardless of r) it is accounted for in the propagator of the source fermion. Further examples include Figs. 26(i)-(ii), (iv), and (vii)-(viii).
- Any diagram for which the only possible parent diagrams are tadpole diagrams must also vanish. An example is given by Fig. 26(iii).
- Any diagram in which a $G^{(+)}$ boson couples to a background photon must have vanishing net

effect (whether singly or pairwise) when averaged over length scales greater than \mathcal{L}_0 . Otherwise background photons could generate $G^{(\dagger)}$ boson pairs, and these in turn would necessarily have background character, in violation of gauge choice (III:56). Examples include Figs. 26(i) and (v)-(x).

- Diagrams involving an odd number of fermion lines may be eliminated using a generalisation of Furry's theorem. If a diagram or set of diagrams remain invariant when left- and right-handed representations are interchanged, corresponding to reversal of all arrows on the diagram and replacing

$$\bar{\psi}\sigma^\mu\psi \rightarrow \psi\sigma^\mu\bar{\psi} = -\bar{\psi}\sigma^\mu\psi, \quad (160)$$

it follows that that set of diagrams must vanish. Examples include Figs. 26(ii) and (ix)-(x), with diagrams (ix)-(x) forming a set which map into one another on arrow reversal, and therefore collectively cancel.

- Any diagram which gives mass to the photon may be discounted by gauge choice (III:60) (with subsequent higher-order corrections as per Sec. III 1 of Paper V). Examples include Figs. 26(vii)-(viii).
- Any diagram in which pseudovacuum couplings explicitly give rise to mass for any of the constituent particles may also be ignored. Examples include Figs. 26(iii)-(iv), in which pseudovacuum photon coupling gives mass to the electron. [As with many of the examples in Fig. 26 these particular diagrams have multiple reasons to be ignored—the parent of diagram (iii) is a tadpole, and the parent of diagram (iv) belongs to the PSE expansion of the source fermion propagator.]

Regarding why diagrams containing mass interactions may be ignored, recognise that foreground species other than photons and $G^{(\dagger)}$ bosons may either acquire mass as a result of interaction with the background fields, placing them in any generation, or they may be ephemeral—generationless and massless—if they only exist over scales of $O(\mathcal{L}_0)$ or less in the isotropy frame. Both situations are in principle admissible in photon pair decay processes, and thus both massive and massless propagators must be taken into account when evaluating decay processes, unless otherwise constrained. Diagrams in which the foreground propagators are massive implicitly incorporate all diagrams in which pairs of background photon interactions behave as mass vertices as per Papers IV-VI, and thus these pseudovacuum interactions do not need to also be considered separately.

Now consider only diagrams not eliminated by the above considerations. In the large- r limit the most important diagrams in evaluation of the foreground pair

field are those with the least-negative exponent in the radial co-ordinate. As examples of candidate processes, consider the $G^{(\dagger)}$ -mediated diagrams shown in Fig. 27. The presence of a radially outbound photon indicates that these diagrams do not belong to the PSE of the source fermion propagator, and although neutrality of the matter source implies that the *average* value of the outbound foreground photon field must vanish, for any individual photon pair it may be non-zero. Furthermore, in contrast with Figs. 26(i) and (v)-(x), there is no gauge-induced requirement that this process have vanishing impact on the photon pair field as a whole. Indeed, if the source is examined fermion by fermion, these processes may be understood instead as making a fairly high-order contribution to the gyromagnetic anomaly of the electron.

Although shown as $G^{(\dagger)}$ bosons in Figs. 26-27, the circulating off-diagonal boson in these processes may in principle be any of W , G , or \mathbf{a}^{12} . The latter is functionally eliminated by extension of gauge choices (III:45) and (III:55) to all energy scales as described in Sec. III C 7 of Paper III, but the remaining processes—involving either G or W bosons—are potentially non-vanishing, and are all beyond-Standard-Model processes due to the presence of K -matrices in the emission vertices as per Fig. 23(ii).

Specialising first to the $G^{(\dagger)}$ bosons, the requirement that these bosons do not couple to the background photon field implies that all photons in Figs. 27(i)-(ii) are foreground, and thus the diagrams scale as r^{-3} . In contrast, although Fig. 27(iii) is of much higher order in the coupling constant $f = 1.669584(99) \times 10^{-8}$, it is seen in Sec. X C 1 to scale as r^{-1} and is thus of greater importance in the far field regime. Parent diagrams for Fig. 27(iii) prior to mean-field expansion are shown in Figs. 27(iv)-(v), noting that in order to affect the boson pair count in interval $[r, r + dr]$, only the initial decay of one member of the photon pair need take place within that interval; the rest of the diagram may be evaluated over any length scale. It is then convenient to evaluate the other photon of the pair by substituting the pseudovacuum term of the mean field theory expansion. Further, by overall neutrality of the matter source (which is made up of both electrons and positrons), the average onward-propagating photon field necessarily has net zero foreground component, and thus the average total photon field on the outbound leg *also* evaluates to the pseudovacuum field. Nevertheless, diagrams (iv) and (v) are distinguishable as it is possible to spatially discriminate between the mean-field term of a photon inbound from r and the nonvanishing component of a photon outbound to $r + dr$.

It may at first appear problematic that Fig. 27(iii) is being evaluated in a mean-field limit in which the outbound component of the foreground fields vanishes. However, recall that an inverse-square biphoton field mediates no net force transfer beyond that accounted for by its individual constituents, and it is therefore unnecessary for

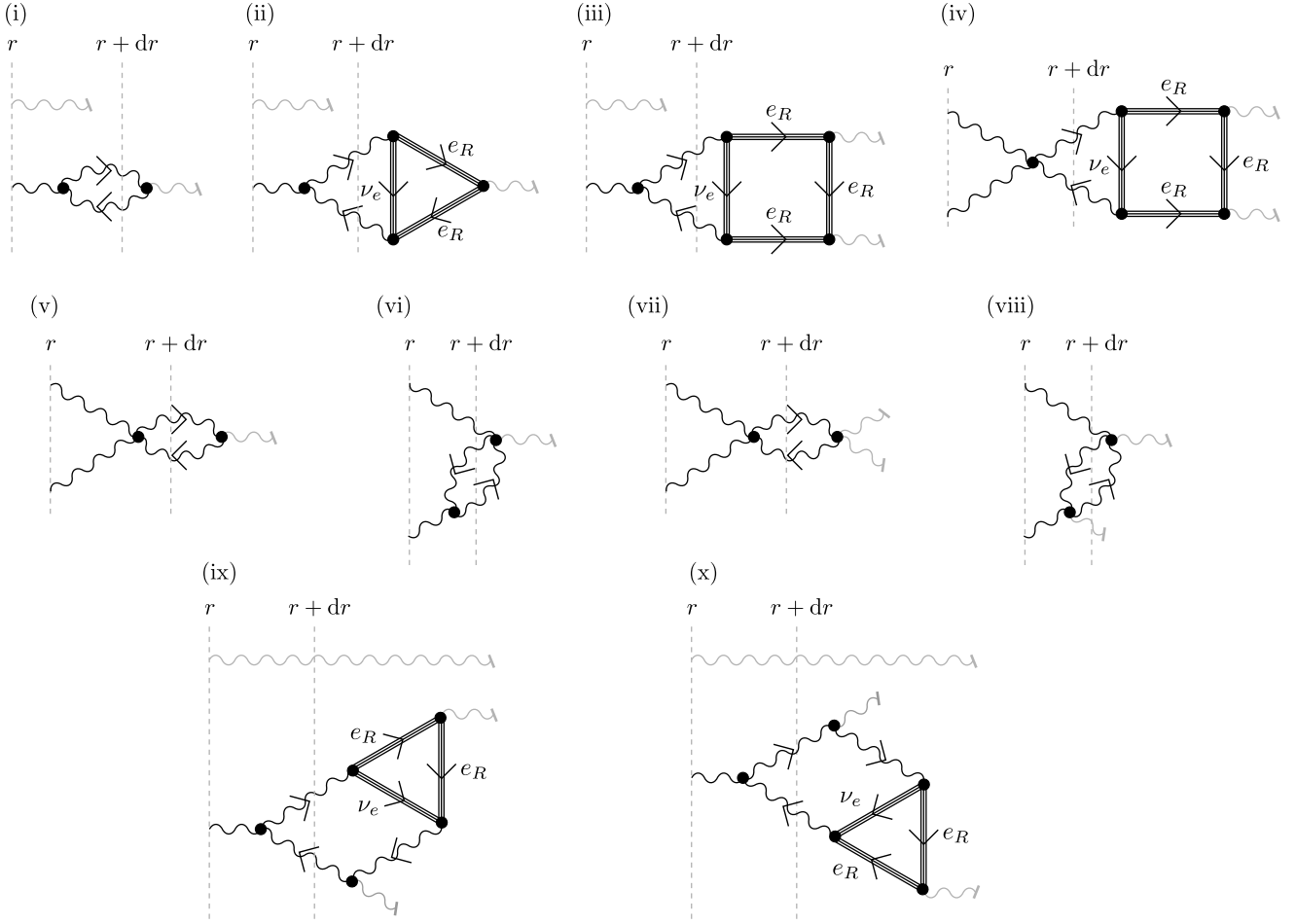


FIG. 26. Candidate diagrams for processes occurring within the photon pair field. Boson lines without an arrow represent photons, and boson lines with an arrow represent G bosons. Disruption of the pair occurs within interval $[r, r + dr)$. Species may be massive with generations, or if existing over time and distance short compared with \mathcal{L}_0 they may lack interactions with the pseudovacuum and be massless and without generation. Note that by Sec. III H 6 of Paper I, all interactions involving only background fields may be ignored. Consequently, background photons attract no vertex in interval $[r, r + dr)$. When the propagation term is treated as a vertex, it is necessarily included in this treatment.

an interaction which reduces the photon pair field to exhibit any net (average) transfer of momentum from this pair field to elsewhere. Further, in the present context (with a net electrically neutral source) the single-photon exchange process likewise mediates no force. Thus the radially outbound single-photon field carries an average foreground momentum of zero, and reduces to the background component on average in the mean-field limit. Consequently, although Fig. 27(iii) has no net outbound foreground particle species, it may nevertheless result in a reduction in the *number* of photon pairs.

Ironically, on mapping negative energy outbound pairs into positive energy inbound pairs, the resulting deviation from inverse-square decay does now result in an imbalance between the outward and inward photon pair pressures (with decay occurring more rapidly in the lower- r , higher-field regime), and may be anticipated to yield a net attractive force between neutral bodies not corresponding to any process in the Standard Model.

This effect is small, so there is no immediate need to engage in a perturbative calculation to evaluate second- and higher-order effects, and to present accuracy it suffices to adopt a co-ordinate frame on $\mathbb{C}^{\wedge 18}$ in which the photon pair number density obeys the expected inverse-square profile with respect to the connection on the $SL(2, \mathbb{C})$ subframe. The coupling of the photon to GG^\dagger pairs in Fig. 27(iii) is thus supplanted by an equivalent coupling to space-time curvature, which is by construction a true space-time curvature on the manifold which is the target of mapping \mathcal{G} .

As noted above, every diagram in Figs. 26-27 also has a counterpart in which the $G^{(\dagger)}$ bosons are replaced by $W^{(\dagger)}$ bosons. However:

- $G^{(\dagger)}$ bosons are massless over all length and timescales, whereas $W^{(\dagger)}$ bosons are massive over scales large compared with \mathcal{L}_0 , and
- there is no requirement that the $G^{(\dagger)}$ or $W^{(\dagger)}$ loop

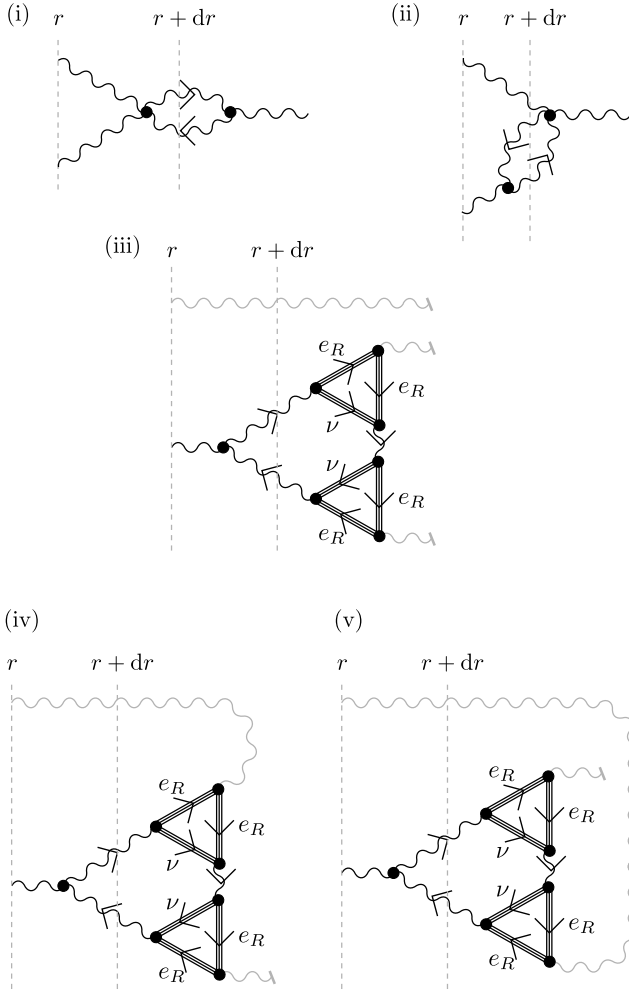


FIG. 27. Example diagrams not eliminated by the considerations of Sec. XB2. Bosons with no arrows are photons, and bosons with arrows are $G^{(\dagger)}$ bosons. Background bosons are shown in grey. Diagrams (i)-(ii) are $O(f^3)$ in vertex coefficients, but scale as r^{-3} so in the far field they are supplanted by diagram (iii), which is of $O(f^7)$ but is seen in Sec. XC1 to scale as r^{-1} . Diagrams (iv)-(v) are parent diagrams for diagram (iii), meaning that they yield it as the zeroth-order term of mean-field expansion about the pseudovacuum state for the indicated photons.

in these figures should be small compared with \mathcal{L}_0 . (This is discussed further in Sec. XC.) Thus behaviour in the low-energy regime is dominated by $\mathcal{L} > \mathcal{L}_0$ in which the W boson is massive but the G boson is not.

- The classical limit of the photon field around a point source may be understood as a superposition of positive and negative energy massless virtual photons. Thus massive W boson loop processes in the photon pair field are heavily disfavoured relative to massless G boson loops.

Taking all of this into account, now observe that electromagnetically neutral composite bodies are ubiquitous

on classical scales, and the K -augmented emission process of Fig. 23(ii) is thus likewise widespread. As a result, so are the $G^{(\dagger)}$ -mediated decay processes which take place throughout the supported photon pair fields. It is postulated that Fig. 27(iii) is the highest-weight beyond-Standard-Model diagram affecting the photon pair field in the large- r regime.

In regions where $G^{(\dagger)}$ -mediated photon pair decay is the dominant beyond-Standard-Model process, it then follows that space-time curvature in the large- r regime, and thus Newton's Constant, may be obtained from evaluation of Figs. 27(iv)-(v). This calculation is performed in Sec. XC.

3. Principle of equivalence

The above discussion has addressed photon pair emission from a prototype source comprising left- and right-handed electrons and positrons. However, for higher-generation leptons, mass is augmented by the K matrices and these appear identically in the fermion mass interaction and in the K -augmented photon pair emission process, with net result that all leptons support the beyond-Standard-Model processes in photon pair fields of Fig. 27 at a rate identically proportional to their mass. Anticipating Sec. XC3, in which these processes are mapped to space-time curvature, this equivalence of proportion implies the weak principle of equivalence for leptons (equivalence of gravitational and inertial mass).

The mass mechanism for quarks is identical to that for leptons. It may therefore be reasonably anticipated that quarks will also respect the weak principle of equivalence.

With baryons also being composite fermions, let it be assumed that the baryon mass mechanism is the natural extension of the quark mechanism, with inertial mass being determined by coupling to background boson fields and by the nine-preon/three-quark counterpart to operator \hat{K}_μ (IV:25). In addition to their preonic constituents, baryons also contain the gluons which bind them together—but then, so do leptons and quarks. Under the assumption that the confinement scale \mathcal{L}_ψ is much smaller than \mathcal{L}_0 , the gluons are not in general able to participate in any mass interactions over their individual lifetimes. They therefore behave as particles without inertial mass, and consequently without gravitational mass. The sole exception to this is the unconfined “neutral gluon” N_μ . However, this particle is not associated with the dimension-8 representation of $SU(3)_C$ and thus is not a participant in the preon or quark confinement interactions. With the gluons being essentially massless, any transient appearances of gluons within a baryon may simply be viewed as variety in the associations of the preon lines making up the baryon (including brief time-reversals in trajectory, and the appearance of temporary loops of characteristic scale less than \mathcal{L}_0 , which are thus normed to 1). The net preon composition, which interacts with the nine-preon analogue of \hat{K}_μ , remains unchanged. It is

therefore reasonable to anticipate that baryonic matter also respects the weak principle of equivalence.

Indeed, the only exception of any significant abundance is likely to be the neutral gluon, N_μ . This particle has an inertial mass of $80.4280(10) \text{ GeV}/c^2$ [22], but its coupling to the photon pair field (via the universal coupling mechanism of Sec. IV B 2 b) is smaller by a factor of $99/\{18[k_1^{(e)}(\mathcal{E}_e)N_0]^4\} = 1.52780(12) \times 10^{-3}$. If the N_μ boson exists in any significant quantity, it has substantial inertial mass (making it a Weakly Interacting Massive Particle or WIMP) and also supports a photon pair field (which is the prerequisite for the gravity-like interaction of the $\mathbb{C}^{\wedge 18}$ model). It is therefore a candidate for an interesting species of dark matter which breaks the weak principle of equivalence (equivalence of gravitational and inertial mass).

C. Evaluation of space-time curvature

This Section calculates the metric in the vicinity of a nonrotating electrically neutral body, including the value of Newton's Constant. Extension to incorporate conceptually important subleading effects is discussed in Sec. XD, though these processes are numerically irrelevant in the large- r regime at current numerical precision.

1. Leading-order photon pair decay profile

To evaluate the photon pair field decay profile as a function of radius, first note the following:

- As per Sec. XB 3, the photon pair field support is expected to scale identically with inertial mass for all fermionic species, so for convenience let any mass M be represented by the already-discussed prototypical chargeless, spinless neutral body made up entirely of electrons and positrons.
- Functionally the propagator term of the Lagrangian behaves as a two-particle vertex, structurally equivalent to the mass vertex but acting with the momentum operator k_μ in lieu of the rest mass operator (which takes the form $[m, 0, 0, 0]$ in the rest frame of the particle).
- On radial propagation the photon pair field supported by a mass M exhibits decay as r^{-2} , such that on propagation from r to $r + dr$ the photon pair field experiences a geometrically induced decrease according to the corresponding infinitesimal relationship

$$A_\mu A_\nu \longrightarrow A_\mu A_\nu \left(1 - \frac{2dr}{r}\right). \quad (161)$$

This is associated with Fig. 24.

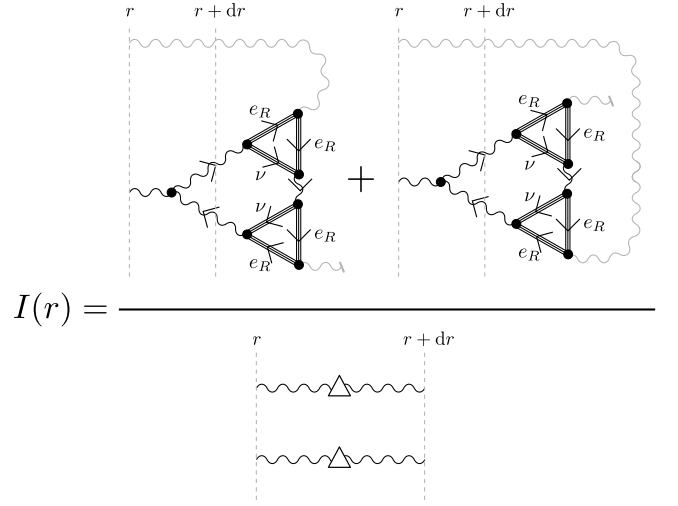


FIG. 28. Relative weight of diagrams associated with photon pair decay, normalised with respect to photon pair propagation. If the latter is associated with a relative decay of $-2dr/r$, then the former is associated with $-2I(r)dr/r$ where $I(r)$ is defined as above.

- Alternatively, the photon pair may undergo decay in accordance with Figs. 27(iv)-(v). Normalising these diagrams with respect to the radial propagation of Fig. 24 introduces the quantity $I(r)$, defined in Fig. 28. The pair propagation of Fig. 24 yields a relative decay of the pair field of $-2dr/r$, as in Eq. (161) above, so that associated with Figs. 27(iv)-(v) is weighted by a further factor of $I(r)$ to yield a contribution of $-2I(r)dr/r$.

- The net relative decay of the photon pair field on propagation from r to $r + dr$ is thus given by

$$A_\mu A_\nu \longrightarrow A_\mu A_\nu \left[1 - \frac{2dr}{r} - \frac{2I(r)dr}{r}\right]. \quad (162)$$

Evaluation of ratio $I(r)$ may be broken down into a series of stages. First, recognise that the behaviour under study is the radial decay of foreground photon pairs. Consider the denominator, and recognise:

- The multiplier of $[k_1^{(e)}(\mathcal{E})]^4$ on Fig. 23(ii) may be interpreted as a modifier to the vertex factor which changes the rate of foreground photon pair emission. Thus each photon line inbound or outbound in the denominator of Fig. 28 is associated with a factor of $[k_1^{(e)}(\mathcal{E})]^2$.
- Although the objects of study are foreground fields, over an interval of width dr the foreground and background fields are not clearly distinguishable. Although the number of photon pairs in the foreground field is clearly determined, the foreground

momentum is distributed across all preons with correlators consistent with photon pairs within this region. In the large- r regime the average momentum of a photon within a pair is that of the pseudovacuum, up to a small foreground perturbation. On-shell, the propagation operators thus evaluate as

$$\Delta^{\mu\nu} \rightarrow k^\mu k^\nu \rightarrow -\delta^{\mu\nu} \omega_0^2. \quad (163)$$

- To evaluate FSF symmetry factors:

- Recognise that the interval $[r, r + dr)$ is small compared with \mathcal{L}_0 and there are four foreground preons inbound (two from r and two from $r + dr$) and four preons outbound, each of which may be of type $a = 1$ or $a = 2$. Colour is summed over and net neutral across the foreground fields, so may be ignored. There are also N_0 inbound and N_0 outbound background preons for any given charge labelling.
- All inbound preons participate in equivalent interactions, so their associated FSFs are interchangeable. Likewise for all outbound preons.
- First assume all inbound foreground preons have the same A -charge; conservation of charge requires that the outbound charges be the same. The first photon line in the diagram may incorporate any one of the $N_0 + 4$ inbound preons (or more strictly, incorporates one specific inbound preon but this may be associated with any of $N_0 + 4$ eligible FSFs), and any one of the four $N_0 + 4$ outbound preons (ditto). Up to a normalisation factor, the corresponding sources/sinks are associated with a FSF symmetry factor of $(N_0 + 4)^2$. The second photon yields $(N_0 + 3)^2$, and so on. There are two choices of the A -charge involved ($a = 1$ and $a = 2$). This yields two configurations each with a factor of $[(N_0 + 4)(N_0 + 3)(N_0 + 2)(N_0 + 1)]^2$.
- Next, consider configurations where one inbound preon has a different charge to the others. There are eight such configurations, each yielding a factor of $[(N_0 + 3)(N_0 + 2)(N_0 + 1)]^2$.
- Finally, there are six configurations in which two inbound preons have charge $a = 1$ and two have charge $a = 2$, for a factor of $[(N_0 + 2)(N_0 + 1)]^4$.
- Normalisation with respect to background fields as per Sec. III H 6 of Paper I requires that for a single background photon field source/sink the FSF symmetry factor goes to 1. That is, in the absence of foreground fields the source/sink attracts a factor of N_0^2 and this is then divided by N_0^2 .

- As all photons in the above factors are foreground, the number of background FSFs available is constant at N_0 for every term, so

$$\begin{aligned} (N_0 + 4) &\rightarrow N_0^{-1}(N_0 + 4) \\ (N_0 + 3) &\rightarrow N_0^{-1}(N_0 + 3) \\ &\vdots \end{aligned} \quad (164)$$

- For each of these configurations, the same symmetry factors apply at the propagation operators (considered collectively) as at the sources/sinks (considered collectively), though without requiring the N_0^{-1} normalisation factor. Instead, Sec. III H 6 of Paper I is taken to imply that no vertex should be drawn which involves only background fields.
- The net FSF symmetry factor associated with the sources and sinks is thus

$$N_0^8 S_{\Delta\Delta} \quad (165)$$

where $S_{\Delta\Delta}$ is a correction of $O(1)$ given by

$$\begin{aligned} S_{\Delta\Delta} := & \{2[(N_0 + 4)(N_0 + 3)(N_0 + 2)(N_0 + 1)]^4 \\ & + 8[(N_0 + 3)(N_0 + 2)(N_0 + 1)]^4 \\ & + 6[(N_0 + 2)(N_0 + 1)]^8\} / (16N_0^{16}). \end{aligned} \quad (166)$$

- Following construction of the photons, their connection to the propagation vertices attracts a symmetry factor of sixteen:
 - The first photon (let this be a photon inbound from r) may be connected to any of the four connection points on the two propagation vertices: Factor 4.
 - The second photon at the same radius must be connected to one of the two connection points on the other propagation vertex: Factor 2.
 - The first of the remaining two photons may be connected to the remaining connection point on either of the propagation vertices: Factor 2.
 - The final photon has only one possible connection: Factor 1.
- The net factor associated with the denominator is thus

$$16 \left[k_1^{(e)}(\mathcal{E}) \right]^8 \omega_0^4 N_0^8 S_{\Delta\Delta}. \quad (167)$$

Now consider the numerator:

- Figures 27(iv)-(v) both evaluate to the same value, therefore specialise to Fig. 27(iv) and multiply by two.

- The lower photon in the pair inbound at r is required to be foreground as it interacts with the $G^{(\dagger)}$ fields. The upper photon may be foreground or background, and the contribution of the diagram will be dominated by the background terms at large r .
- The foreground photon decay vertex within interval $[r, r + dr)$ is associated with a factor of $f/\sqrt{2}$.
- The vertex (propagation or otherwise) within this interval which acts on the other member of the photon pair is not shown. Figure 27(iv) is dominated by contributions in which this member evaluates to the background term, and while a background photon may indeed undergo an interaction within interval $[r, r + dr)$, its effect on Fig. 27(iv) is normed away as per Sec. III H 6 of Paper I.
- Note that the vertex in Fig. 27(iv) in which this background photon does engage *may* be within interval $[r, r + dr)$ but is not required to be—the value of the diagram is independent of the radius at which this vertex is evaluated.
- Since only the lower photon inbound from r is foreground, only that photon attracts a factor of $[k_1^{(e)}(\mathcal{E})]^2$. In conjunction with the quantum/classical correlation of Sec. IX B, the net classical factor associated with the photon field of a single pair at the lower vertex is thus $[k_1^{(e)}(\mathcal{E})]^2/r$.
- There are M/m_e fermions capable of acting as sources of such a pair, so this factor is multiplied by M/m_e to yield $[k_1^{(e)}(\mathcal{E})]^2 M/(m_e r)$.
- A momentum operator $i\partial_\mu$ also acts at this vertex.
 - It may act on the photon field, the G field, or the G^\dagger field, with the weights of the latter two processes being half that of the former.
 - As previously discussed for the denominator term, the momentum associated with the foreground photon field is distributed across all photons within the local correlation region. On average the background contribution vanishes, but *instantaneously* the action of the derivative operator on the A_μ field at this vertex is given by $N_0^2 i\omega_0$, up to an arbitrary sign and a small perturbation representing the foreground field superimposed on the pseudovacuum. The factor of N_0^2 arises from the choice of FSF fields which may be acted on by the chiral derivative operators making up the background photon whose momentum is then evaluated.
 - There is a further factor of $\frac{1}{2}$ from the structure constants of $SU(3)_A$.

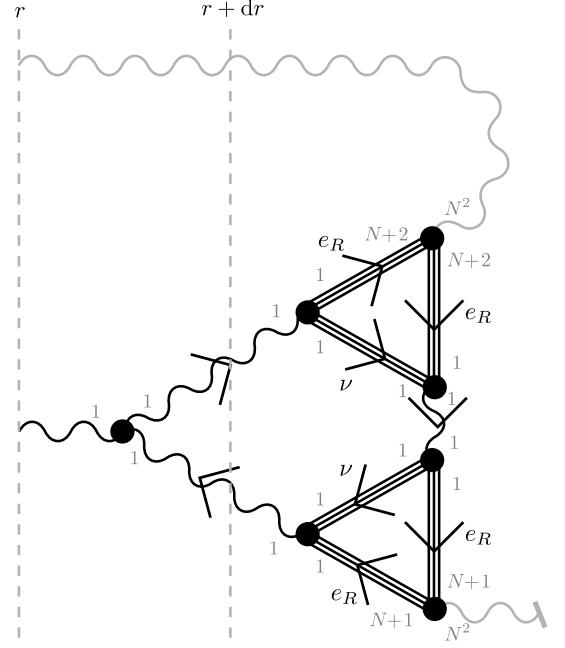


FIG. 29. FSF symmetry factors associated with Fig. 27(iv). Regarding the two vertices incorporating interactions with the background photon field, note that the fermion symmetry factors are of $O(N_0)$ and not $O(N_0^3)$ as only one preon per fermion triplet interacts with the boson. Also note that these vertices are within \mathcal{L}_0 of one another and thus the symmetry factors increment, yielding $(N_0 + 2)(N_0 + 1)$ on the interacting preons of the inbound electrons and the same again on the interacting preons of the outbound electrons, rather than $(N_0 + 1)(N_0 + 1)$ apiece.

- The terms in which the derivative operator acts on G and G^\dagger may be ignored as there are no background $G^{(\dagger)}$ fields and the contributions which these terms yield are thus negligible at large r .
- The subsequent completion of the decay process, which may take place outside interval $[r, r + dr)$, contains a further six vertices which yield a factor of $f^6/2$.
- Two of these vertices involve pseudovacuum photons. As this portion of the diagram is not constrained to take place within interval $[r, r + dr)$, in order to be non-vanishing these vertices must be within the same autocorrelation region of the pseudovacuum (i.e. within distance and time \mathcal{L}_0 of one another in the isotropy frame). Up to FSF symmetry factors, they therefore evaluate to $-\omega_0^2$.
- The FSF symmetry factors associated with the interaction vertices in Fig. 27(iv) are illustrated in Fig. 29.
- There is a symmetry factor of 2 associated with the interchangeability of the two fermion triangles within the G boson loop.

- Regarding particle masses in Fig. 27(iv):

- On-shell photons and $G^{(\dagger)}$ bosons are massless.
- The neutrino-family and electron-family particles may be massive or massless, with the latter being favoured over scales small compared with \mathcal{L}_0 . With the two background photon interactions being within a single autocorrelation region, the portion of the diagram connecting these two vertices may either incorporate a direct path which remains within the autocorrelation region and is therefore made up of massless particles, or it may be that for any path from one vertex to the other, one or more particles ventures outside of the autocorrelation region and thus (with the exception of the G boson) may be anticipated to acquire mass. To then return to the original autocorrelation region and connect with the other background vertex then involves a significantly off-shell trajectory. Thus interactions are anticipated to be dominated by conditions in which there exists at least one series of massless propagators connecting the two background photon interactions. Thus at least one of the electron lines in each triangle is massless.
- For Fig. 27(iv) it then follows directly that the closest diagrams to on-shell are those in which all fermions are massless. This is revisited for loop corrections in Sec. XC 2.

- Examining the fermion triangles, at each vertex the interaction is averaged over three preons equivalent up to colour. The result is numerically unchanged by replacing each with a single interaction multiplied by a factor of three.
- If this is done so as to bring each vertex onto the same preon within each loop, as per Fig. 30(i), then two of the preons within each loop are now free loops. In the massless regime, diagrammatic isotopy techniques (or equivalently, vacuum normalisation) give that such loops evaluate to 1. This leaves four superfluous FSFs at each vertex, but these are cancelled by the factors of $f = \langle \varphi \rangle^{-1}$ appearing in the definition of the fermion operators (III:28), so may also be removed for an average factor of 1.
- Up to differences in FSF symmetry factors, the remaining unevaluated preons in the fermion loop are then seen to be equivalent to G bosons, as per Fig. 30(ii), permitting reduction of the loop structure of Fig. 27(iv) to that of Fig. 30(iii). Note that this reduction is only valid up to a factor of $f^4(N_0 + 2)^2(N_0 + 1)^2N_0^4$ corresponding to vertices and FSF symmetry factors present in Fig. 27(iv) but not in Fig. 30(iii).

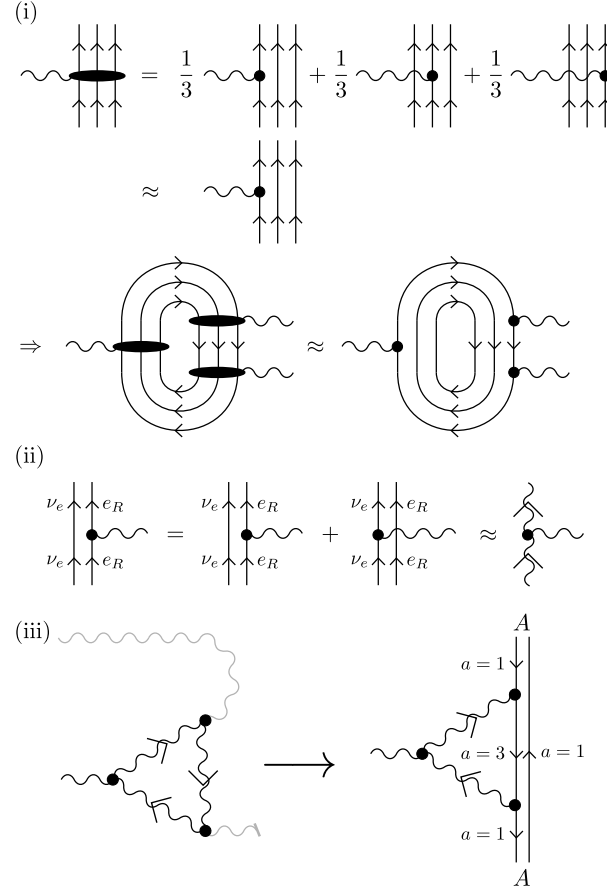


FIG. 30. (i) Interaction vertices involving fermions are averaged over three different internal configurations. However, it is numerically equivalent to replace these interactions with a single interaction weighted by a factor of three. In the fermion loops of Fig. 27(iv) this permits two fermion loops to be disconnected, and thus mapped to vacuum fluctuations and evaluated to yield factors of 1. (ii) The neutrino is associated with preons having $a = 3$. Since these preons have no electric charge, the interaction of the photon with the $a = 1$ preon is equivalent to the total interaction of the photon with the entire preon pair. Up to considerations of FSF symmetry factors, this preon pair is equivalent to a G boson. The loop structure of Fig. 27(iv) therefore reduces to a single G boson loop as shown in diagram (iii), up to a numerical factor of $f^4(N_0 + 2)^2(N_0 + 1)^2N_0^4$ corresponding to vertices and FSF factors present in Fig. 27(iv) but not in this diagram. If the preon decomposition of some of the bosons in diagram (iii) is made explicit, the resulting diagram may be understood as a loop correction to photon emission/absorption by a preon with $a = 1$. (The photon also contains terms with $a = 2$ but these do not couple to the $G^{(\dagger)}$ fields, and this is accounted for in the factor of $1/\sqrt{2}$ on the A/G coupling coefficient.) The loop boson is massless but chiral, and the loop thus evaluates to a factor of $(f^2/2)(1/4\pi)$ as per Appendices A-B, of which the vertex-related factor of $f^2/2$ has already been accounted for.

- Selecting out a specific subdiagram as per Fig. 30(iv) permits evaluation of the resulting G boson loop to yield a factor of $1/(4\pi)$.
- Finally, note that Fig. 27(iv) incorporates the completed exchange of a foreground photon between a source at radius r (as proxy for the original neutral source) and the AGG^\dagger vertex, which attracts a factor of S_α . This is independent of, and in addition to, the other FSF symmetry factors in Fig. 29.

Putting this all together permits evaluation of the mean value of the numerator of $I(r)$, up to a sign arising from the derivative operator in the AGG^\dagger vertex. The mean magnitude of the numerator is given by

$$\frac{Mf^7 \left[k_1^{(e)}(\mathcal{E}) \right]^2 \omega_0^3 N_0^6 (N_0 + 2)^2 (N_0 + 1)^2 S_\alpha}{4\sqrt{2}\pi m_e r}. \quad (168)$$

Curiously, the sign of this term is unimportant. The interactions of Fig. 27(iv)-(v) unambiguously destroy photon pairs, whereas the ambiguity of the sign merely ensures vanishing of any emitted species. For a neutral source this is already known. However, it is interesting to note that with a charged source, this summation over sign ensures that photon pair decay does not lead to any unexpected augmentation of the single-photon field.

The overall leading-order expression for $\langle |I(r)| \rangle$ is thus

$$\langle |I(r)| \rangle = \frac{Mf^7 N_0^2 S_G S_\alpha}{64\sqrt{2}\pi \left[k_1^{(e)}(\mathcal{E}) \right]^6 \omega_0 m_e r} \quad (169)$$

$$S_G := \frac{(N_0 + 2)^2 (N_0 + 1)^2}{N_0^4 S_{\Delta\Delta}}, \quad (170)$$

with the infinitesimal radial decay of the photon pair field taking the form

$$A_\mu A_\nu \longrightarrow A_\mu A_\nu \left(1 + \frac{2dr}{r} + \frac{2\langle |I(r)| \rangle dr}{r} \right). \quad (171)$$

2. Higher-order corrections

Two sources of higher-order corrections are evaluated in the present paper. These are the $O(\alpha)$ corrections to Fig. 27(iv)-(v), and the $O(N_0^{-1})$ corrections associated with introducing an additional boson. Following the approach of Sec. VB2, these latter corrections are evaluated as a multiplicative correction to the $O(\alpha)$ terms.

a. The $O(\alpha)$ corrections are given by Fig. 31, where the photon loops may be viewed as generating gyromagnetic anomaly-like corrections to the interactions with background fields and/or neutrino emission processes. The first step in evaluating these diagrams is to determine which loop vertices are within the same correlation region as the two interactions with the photons from the pseudovacuum. As observed in Sec. XC1, at least one of

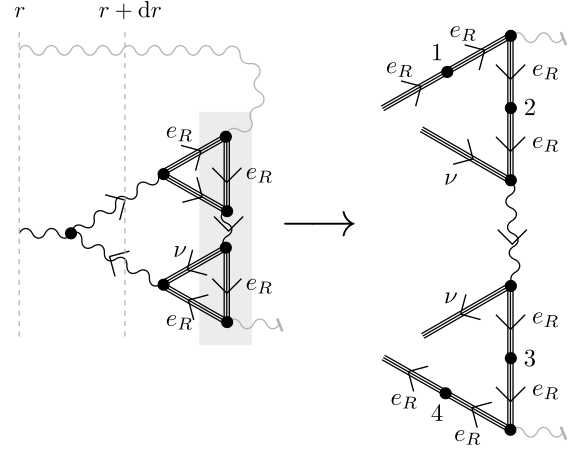


FIG. 31. Six diagrams give rise to $O(\alpha)$ corrections to each of Figs. 27(iv)-(v). Considering Fig. 27(iv) and magnifying the area of interest as shown, these corrections are constructed by pairwise connecting the points marked 1-4. Diagram (i) corresponds to connection of points 1 and 2, diagram (ii) to connection of 1 and 3, diagram (iii) to connection of 2 and 4, diagram (iv) to connection of 3 and 4, diagram (v) to connection of 2 and 3, and diagram (vi) to connection of 1 and 4. Equivalent diagrams existing for Fig. 27(v).

the electron-family lines associated with the pseudovacuum interaction must be massless. However, the other may be massive. Considering Fig. 31 diagram (i), one of the two ends of the loop correction photon is therefore on a massless electron within the correlation region, and the other connects to an electron which *may* be massive. For a loop correction of energy \mathcal{E}_ℓ , contributions are dominated by diagrams with loop vertex separation of $(2\mathcal{E}_\ell)^{-1}$ or less, as per Appendix A which may be substantially larger than \mathcal{L}_0 at low \mathcal{E}_ℓ . It is therefore favoured that at least one electron interacting with each loop fermion be massive.

There is no numerical advantage to having more than one electron line at each pseudovacuum interaction vertex in Fig. 27(iv) be massless, therefore assume only one at each vertex is massless, to maximise the number of massive electron lines available on which to construct photon loop corrections. Regardless of how these are chosen, the subsequent calculation works out equivalently. Therefore choose the massless electrons in Fig. 27(iv) to be those which interact with the loop boson in Fig. 31 diagram (v). Although these electron lines are only strictly required to be massless up to their next interaction vertex, and thus beyond the interaction with the loop correction photon they may hypothetically acquire mass, their massless segments form part of the short path between the pseudovacuum interaction vertices, and thus any loop correction vertices inserted onto these fermion lines may be understood as lying within the same correlation region as the pseudovacuum vertices.

Proceed now to evaluate Fig. 27(iv) with this choice of massless electron lines. As in Fig. 30 it is recognised that

with the neutrino being chargeless, couplings between the loop photon and an electron commute with couplings between the electron and a neutrino, up to any change in FSF symmetry factors. Thus, for example, the correction associated with Fig. 31 diagram (i) is numerically equivalent to that associated with Fig. 31 diagram (ii).

With only one end of the loop photon lying within the same local correlation region as the two pseudovacuum couplings, evaluation of Figs. 31 diagrams (i)-(iv) is without surprises and it follows immediately that each of is associated with a correction factor $\alpha/(2\pi)$, for a subtotal over these four diagrams of $2\alpha/\pi$. Similarly, both loop vertices in Fig. 31 diagram (vi) are outside the region and thus this diagram yields a further contribution of $\alpha/(2\pi)$. In contrast, however, both vertices of the loop correction in Fig. 31 diagram (v) are within the same correlation region as both pseudovacuum vertices. Following the approach described in Appendix B, this diagram yields a symmetry-augmented contribution with weight α/π . The total corrections due to photon loops to $O(\alpha)$ thus multiply Eq. (169) by a factor of

$$\left(1 + \frac{7\alpha}{2\pi}\right). \quad (172)$$

b. The $O(N_0^{-1})$ corrections to the $O(\alpha)$ corrections follow very similarly to those of Sec. VB2, with each loop vertex within the correlation region attracting a further factor of $[1 + 4/(3N_0)]$. There is one such vertex in each of Fig. 31 diagrams (i)-(iv), yielding

$$\frac{\alpha}{2\pi} \cdot \frac{4}{3N_0} \quad (173)$$

apiece, and there are two such vertices in Fig. 31 diagram (v), yielding

$$2 \cdot \frac{\alpha}{\pi} \cdot \frac{4}{3N_0}. \quad (174)$$

The total higher-order corrections to Eq. (169) are thus

$$\left[1 + \frac{7\alpha}{2\pi} + \frac{16\alpha}{3\pi N_0} + O\left(\frac{\alpha}{\pi N_0^2}\right) + O\left(\frac{\alpha^2}{\pi^2}\right)\right]. \quad (175)$$

3. Elimination of GG^\dagger pairs

To eliminate the formation of GG^\dagger pairs, it suffices to identify a choice of co-ordinate frame for which the radial profile of the photon pair field is returned to inverse-square. This replaces couplings between the AA and GG^\dagger fields with interactions between the photon pair field and space-time curvature. As the photon pair field has recovered an inverse-square profile, it becomes undetectable (as it no longer mediates any direct force transfer) and the resulting space-time curvature may be associated with the neutral body which acts as the source of the field. Under mapping \mathcal{G} from $M \subset \mathbb{C}^{\wedge 18}$ to a manifold

$\mathcal{G}(M)$ which is locally Minkowski, this is a true curvature on the target manifold, and the $SL(2, \mathbb{C})$ connection on $\mathbb{C}^{\wedge 18}$ maps to the space-time connection on $\mathcal{G}(M)$, appearing appropriately in the covariant derivative operator and thus acting on all (quasi)particles appearing on $\mathcal{G}(M)$.

Note that with the resultant AA field exhibiting inverse-square propagation, although the AA fields prior to gauging determine the curvature of the resulting space-time, after gauging they do not couple to it. Thus the implied graviton is massless.

To realise the requisite co-ordinate frame, and thus identify the target space-time of mapping $\mathcal{G}(M)$, recognise that the total decay process of Eq. (171) resembles that of Eq. (161) with the radial propagation interval rescaled as

$$dr \longrightarrow dr [1 + \langle |I(r)| \rangle]. \quad (176)$$

As this effect affects *only* radial propagation, it is akin to evaluating purely geometric propagation on the space-time whose metric is obtained from that of Minkowski space-time by substituting

$$dr^2 \longrightarrow dr^2 [1 + 2\langle |I(r)| \rangle]. \quad (177)$$

Recalling that the \mathbb{R}^+ component of the $GL(18, \mathbb{C})$ symmetry of the $\mathbb{C}^{\wedge 18}$ model was gauged in Sec. VC7, the volume form must be conserved, giving

$$dt^2 \longrightarrow dt^2 \{1 - 2\langle |I(r)| \rangle + O[\langle |I(r)| \rangle^2]\}. \quad (178)$$

and this serves to uniquely identify the target space-time as one which supports the Schwarzschild metric,

$$ds^2 = - \left(1 + \frac{2G_N M}{r}\right)^{-1} dt^2 + \left(1 + \frac{2G_N M}{r}\right) dr^2 + r^2 d\Omega, \quad (179)$$

with

$$G_N := \frac{f^7 N_0^2 S_G S_\alpha}{64\sqrt{2}\pi [k_1^{(e)}(\mathcal{E})]^6 \omega_0 m_e} \left(1 + \frac{7\alpha}{2\pi} + \frac{16\alpha}{3\pi N_0}\right) \times \left[1 + O\left(\frac{\alpha}{\pi N_0^2}\right) + O\left(\frac{\alpha^2}{\pi^2}\right)\right]. \quad (180)$$

Taking into account the definitions of N_0 , f , and ω_0 as per Eqs. (C5), (154), and (D4) this may be solved simultaneously with Eqs. (137–148) to yield

$$G_N = 6.67427(240) \times 10^{-11} \text{ m}^3 \text{ kg}^{-1} \text{ s}^{-2}, \quad (181)$$

with the central value differing from observation at the level of $0.18 \sigma_{\text{exp}}$.

4. Rotating source

Extension to a rotating source is not considered explicitly in terms of photon pair decay in this paper. However, noting that the argument deriving the Kerr metric is a classical one [23], requiring only the Schwarzschild metric and a rotating frame of reference, its extension to the $\mathbb{C}^{\wedge 18}$ model is expected to be immediate within the regime of validity of Eq. (179), this corresponding to the classical regime and a source sufficiently close to rest in the isotropy frame of the $\mathbb{C}^{\wedge 18}$ model, and excluding high-curvature regimes in which it would be necessary to also take into account corrections of higher order in r such as Figs. 27(i)-(ii), or in which the assumption that the foreground field is small is anticipated to break down.

D. Beyond the dominant process

1. Other spin-2 processes

The above discussion has centred around Fig. 27(iii) and its $O(\alpha)$ corrections. However, it extends directly to other beyond-Standard-Model spin-2 interactions, in which the relevant spin-2 boson field is mapped to a further correction to curvature such that the effect of the beyond-Standard-Model effect vanishes on the foreground field counterparts of the Standard Model and is replaced by the effect of a curved space-time.

Understanding how all spin-2 beyond-Standard-Model processes correct photon pair propagation in the flat-space gauge thus permits more precise calculation of the geometry of space-time in the curved-space (physical) gauge, with photon pair propagation then being purely geometric on that curved space-time in keeping with the expectations of the Standard Model (supplemented by dark processes involving boson N_μ).

The further extension to absorb beyond-Standard-Model spin-1 processes into the space-time curvature is discussed in Sec. XD 2.

2. The right weak interaction and other spin-1 effects

While the above process may readily be extended to eliminate all spin-2 beyond-Standard-Model processes, further detail is required regarding spin-1 processes such as the right-handed weak interaction. Processes such as

$$\nu_e \longrightarrow \bar{\nu}_R + G \quad (182)$$

may create single $G^{(\dagger)}$ bosons, which does not immediately admit a mapping to space-time curvature.

The solution is a technique previously encountered in Sec. IIIE 4 of Paper III and Sec. IIIB 2 of Paper IV in which a process serves as a point of reference for charge on a sector. In Sec. IIIB 2 of Paper IV, the identification of preon triplets in fermions as being the reference point

for colour neutrality induced an active co-ordinate transformation which gave rise to the K matrices. Similarly, now let it be a point of definition that all $G^{(\dagger)}$ bosons appear in GG^\dagger pairs. The only other comparable imposition of an active co-ordinate transformation on the A sector is the introduction of co-ordinate sleeves in Sec. IIIE 4 of Paper III, and the processes which give rise to these transformations are independent and may both be applied as required without conflict. Every G boson emission is thus accompanied by a G^\dagger boson emission, and the resulting pair may be immediately mapped to space-time curvature, completing elimination of all $G^{(\dagger)}$ bosons from the $\mathbb{C}^{\wedge 18}$ model.

It is tempting—but inappropriate—to attempt to also apply this process to the neutral N boson. In contrast with the $G^{(\dagger)}$ bosons, the N boson does not change the species of particles it interacts with, and it is also not a significant force mediator in its own right. Its largest physical effect is as a gravitational source. The $W^{(\dagger)}$ and $G^{(\dagger)}$ bosons do also gravitate, and thus there will be corrections of $O(99/\{18[k_1^{(e)}(\mathcal{E}_e)N_0]^4\})$ to the massive versions of Fig. 27(iii) arising via the universal coupling mechanism (Sec. IVB 2b), but for the N boson (which has a near-totally-eliminated coupling on the A sector) there is no significant leading-order effect to correct. Further, as a weakly-interacting species it is relatively stable, and thus the primary effect of its massive nature is anticipated to be as a gravitational source in its own right, not as a correction to its (negligible) effects on photon pair decay. A co-ordinate sleeve cannot be applied to such a process. For this reason, the N boson is assumed not to be mapped to space-time curvature, and is predicted to be discoverable with an inertial mass of $80.4280(10) \text{ GeV}/c^2$ and a gravitational mass of $240.466(18) m_e$.

XI. RESULTS

A. Value of Newton's constant

As noted in Sec. XC, elimination of the $G^{(\dagger)}$ bosons from the $\mathbb{C}^{\wedge 18}$ model induces the Schwarzschild metric

$$ds^2 = - \left(1 + \frac{2G_N M}{c^2 r} \right)^{-1} dt^2 + \left(1 + \frac{2G_N M}{c^2 r} \right) dr^2 + r^2 d\Omega \quad (179)$$

on the target manifold of mapping \mathcal{G} which acts on $M \subset \mathbb{C}^{\wedge 18}$. Further, the value of G_N is fixed to be

$$G_N := \frac{f^7 N_0^2 S_G S_\alpha}{64\sqrt{2}\pi [k_1^{(e)}(\mathcal{E})]^6 \omega_0 m_e} \left(1 + \frac{7\alpha}{2\pi} + \frac{16\alpha}{3\pi N_0} \right) \times \left[1 + O\left(\frac{\alpha}{\pi N_0^2}\right) + O\left(\frac{\alpha^2}{\pi^2}\right) \right]. \quad (180)$$

Substituting as per Eqs. (C5), (154), and (D4) and making factors of c and h explicit yields

$$G_N = \frac{\alpha^4 h c [1 + \Delta_e(m_e, \mathcal{E}_e)]^{\frac{1}{2}} (S_{18,147} C_{\alpha, N_0})^{\frac{1}{2}} S_G}{8\pi N_0^{18} [k_1^{(e)}(\mathcal{E})]^4 m_e^2 (1 + a_e)^8 S_\alpha^3} \times \left(1 + \frac{7\alpha}{2\pi} + \frac{16\alpha}{3\pi N_0}\right) \times \left[1 + \mathcal{O}_b + \mathcal{O}_e(m_e, \mathcal{E}_e) + \mathcal{O}\left(\frac{\alpha^2 m_e^2}{m_\mu^2}\right)\right] \quad (183)$$

$$S_{18,147} := N_0^{-12} (N_0 + 2)^6 (N_0 + 1)^6 \quad (D5)$$

$$C_{\alpha, N_0} := \frac{1 + \frac{3\alpha}{2\pi} \left(1 + \frac{8}{9N_0}\right)}{1 + \frac{3\alpha}{2\pi}} \quad (80)$$

$$S_\alpha := N_0^{-6} (N_0 + \frac{5}{4}) (N_0 + 1)^3 (N_0 + 2)^2 \quad (\text{III:84})$$

$$S_G := 16(N_0 + 2)^2 (N_0 + 1)^2 N_0^{12} \times \{2[(N_0 + 4)(N_0 + 3)(N_0 + 2)(N_0 + 1)]^4 + 8[(N_0 + 3)(N_0 + 2)(N_0 + 1)^2]^4 + 6[(N_0 + 2)(N_0 + 1)]^8\}^{-1} \quad (184)$$

where the above equations fully define G_N in terms of the parameterisation of Eqs. (137–148). Note that the error terms \mathcal{O}_b and $\mathcal{O}_e(m_e, \mathcal{E}_e)$ incorporate error terms E1–E15 of Paper VI, and also the error terms appearing in Eq. (180) in the present paper, which are designated E20 and E21 respectively. The remaining term $\mathcal{O}(\alpha^2 m_e^2 / m_\mu^2)$ corresponds to error term E19 in Appendix D, and need not in fact be written explicitly as it is small compared with term $\mathcal{O}(\alpha^2 / \pi^2)$ in \mathcal{O}_b . However, retaining it ensures that this term will not be overlooked when subsequent higher-order calculations reduce the magnitude of the error terms in \mathcal{O}_b .

Evaluating Eq. (183) simultaneously with Eqs. (137–148) yields

$$G_N = 6.67427(240) \times 10^{-11} \text{ m}^3 \text{ kg}^{-1} \text{ s}^{-2}. \quad (181)$$

The sources of uncertainty in this result include all those listed in Table VI, E19 from Appendix D, plus also those listed in Table VIII. Their magnitudes are tabulated in Table IX. As in Paper VI, rather than attempting to quantify the magnitudes of the higher-order corrections these have simply been given a generous coefficient with the intent that this should result in a substantial overestimate of the uncertainty in the resulting figure. The

TABLE VIII. List of supplementary sources of uncertainty in the calculation of G_N (183).

Label	Description
E20	$\mathcal{O}[\alpha / (\pi N_0^2)]$ term in Eq. (180)
E21	$\mathcal{O}(\alpha^2 / \pi^2)$ term in Eq. (180)

largest terms in the uncertainty results from contributions E2 and E4, which correspond to two-loop corrections to the boson mass diagrams.

The value of Newton's constant thus obtained is presently less precise than experimental results, but the central calculated value is nevertheless in agreement with observation at the level of $0.18 \sigma_{\text{exp}}$.

B. Qualitative implications

It is interesting to examine some key qualitative properties of the gravitational mechanism of the $\mathbb{C}^{\wedge 18}$ model. First, the extent to which the model truly realises a space-time curvature. The underlying $\mathbb{C}^{\wedge 18}$ manifold remains flat, but the emulated manifold with real co-ordinates, $\mathcal{G}(M)$, has a true curvature as reflected by metric (179). This is the same curvature as is exhibited by the $\text{SL}(2, \mathbb{C})$ subgroup of the physically motivated co-ordinate frame on $\mathbb{C}^{\wedge 18}$. In one sense it might therefore be argued that the underlying manifold is flat, with metric $\varepsilon^{\alpha\beta}$. In another, to the extent that there exists a space-time inhabited by the particles of the Standard

TABLE IX. Contributions of different sources of error to the value of G_N , expressed both in units of $\text{m}^3 \text{ kg}^{-1} \text{ s}^{-2}$ and relative to the experimental error. Labels are enumerated in Table VI, Table VIII, and Appendix D. For purposes of summation, sources of error are assumed independent.

Label	Coefficient	Uncertainty in G_N	
		$10^{-14} \text{ m}^3 \text{ kg}^{-1} \text{ s}^{-2}$	σ_{exp}
E1	± 10	0.19	1.26
E2	± 10	1.58	10.50
E3	± 10	0.19	1.26
E4	± 10	1.58	10.54
E5	± 10	0.00	0.00
E6	± 10	0.00	0.01
E7	± 10	0.02	0.12
E8	± 10	0.01	0.06
E9	± 10	0.68	4.54
E10	± 10	0.30	2.02
E11	± 10	0.01	0.10
E12	± 10	0.01	0.09
E13	± 10	0.03	0.23
E14	± 10	0.00	0.01
E15	1	0.01	0.06
E16	± 1	0.00	0.00
E17	± 1	0.00	0.01
E18	± 1	0.00	0.01
E19	± 10	0.00	0.00
E20	± 10	0.00	0.03
E21	± 10	0.36	2.38
Total		2.40	15.97

Model, this space–time is curved. This is conceptually not dissimilar to the widely-used technique of treating the metric or vierbein/vielbein as a field over a Minkowski space–time, with the particles inhabiting that space–time then coupling to the indices of the metric/vielbein rather than that of the Minkowski space–time itself. The only significant difference here is in the choice of underlying manifold (and hence the construction consequently required to generate emergent normalisable quasiparticles on that manifold).

Given this fairly robust footing for interpreting the $SL(2, \mathbb{C})$ co-ordinate frame in the physical gauge as a true curvature of the emergent space–time, at a minimum up to energy scales of $\mathcal{E}_\Omega \sim 6.2$ TeV and potentially beyond, the gravitational interaction of bosons is of particular interest. All species of boson in the $\mathbb{C}^{\wedge 18}$ model break the weak principle of equivalence, which may variously be stated as the bosons having different value(s) of Newton’s constant to the fermions, or the bosons having discrepancies between their gravitational and inertial masses. This is of particular significance given the existence of the neutral vector boson N_μ , which is colourless, and chargeless with respect to both electromagnetic and weak interactions, but is nevertheless capable of participating in gravitational interactions, albeit with an effective gravitational mass substantially smaller than its inertial mass. With an inertial mass of $80.4280(10)$ GeV/ c^2 [22] and a gravitational mass only $240.466(18) m_e$ (where m_e is the gravitational mass of the electron), it is a candidate for an unusual form of WIMP dark matter.

XII. CONCLUSION TO PART VII

This paper has provided a further demonstration of the predictive capability of the $\mathbb{C}^{\wedge 18}$ model, this time permitting calculation of the value of Newton’s constant from first principles. This comes in addition to the previous derivation of the masses of the tau particle and the W , Z , and Higgs bosons presented in Paper VI [22]. In both calculations, the only input parameters are the fine structure constant and the masses of the electron and muon, and the model is completely without any other tuning parameters.

The $\mathbb{C}^{\wedge 18}$ model was originally introduced as an analogue model, emulating the Standard Model within an appropriate energy regime. However, with elimination of the G and G^\dagger bosons, and the nonvanishing photon pair field rendered physically irrelevant, there are now no known points of tension remaining between the $\mathbb{C}^{\wedge 18}$ model and experimental observation. Of course, the $\mathbb{C}^{\wedge 18}$ model is much newer than the Standard Model and has not been subjected to anything like as exhaustive a search for incongruencies with physical reality.

Further testing of the $\mathbb{C}^{\wedge 18}$ model may comprise further detailed numerical predictions for parameters already observed, and also for parameters and particle species not yet observed, such as the mass of the sec-

ond generation W boson anticipated to appear at around 17 TeV/ c^2 (and, indeed, its heavy Z and Higgs boson companions at 19 TeV/ c^2 and 26 TeV/ c^2 respectively). The calculation of known parameters will allow further elucidation of the regime of validity of the model, while the calculation of as-yet-unknown physical parameters (such as the mass of the W_2 boson) will provide for direct experimental tests of its predictive power in previously unexplored domains.

It should be noted that the lack of any tuning parameters indicates that these predictions are already implicit in the model to arbitrarily high precision, and it is now merely necessary to perform the requisite calculations to obtain high-accuracy concrete numerical predictions.

Having come thus far, and calculated the value of so many fundamental constants, it is apposite to come full circle to the opening paragraphs of Paper I [1] and speculate whether *all* of physics is in fact the study of quasiparticles.

ACKNOWLEDGMENTS

This research was supported in part by the Perimeter Institute for Theoretical Physics. Research at the Perimeter Institute is supported by the Government of Canada through Industry Canada and by the Province of Ontario through the Ministry of Research and Innovation. The author thanks the Ontario Ministry of Research and Innovation Early Researcher Awards (ER09-06-073) for financial support. This project was supported in part through the Macquarie University Research Fellowship scheme. This research was supported in part by the ARC Centre of Excellence in Engineered Quantum Systems (EQuS), Project No. CE110001013.

Appendix A: Mass-related loop coefficients

In Sec. IV A 1 it was observed that the one-photon-loop correction to lepton magnetic moment is associated with a factor of

$$2\alpha \cdot \mathbf{f}\left(\frac{m_\ell^2}{m_A^2}\right) \cdot \frac{1}{4\pi} \quad (11)$$

while the one- W -loop correction is associated with [11]

$$-\frac{10\alpha}{3} [1 + O(\alpha)] \cdot \mathbf{f}\left(\frac{m_\ell^2}{m_W^2}\right) \cdot \frac{1}{4\pi} \quad (12)$$

where the mass dependency $\mathbf{f}(\cdot)$ evaluates as

$$\mathbf{f}\left(\frac{m_\ell^2}{m_b^2}\right) \longrightarrow \begin{cases} 1 & \text{if } m_b^2 = 0 \\ \frac{m_\ell^2}{4\pi m_b^2} & \text{if } m_b^2 \gg m_\ell^2. \end{cases} \quad (A1)$$

All bosons in these interactions are foreground fields.

In Sec. V A 2 a similar situation is encountered save that the loop bosons are background fields. That is, their values are evaluated as expansions around the mean field value, with terms beyond the first making negligible numerical contribution provided the foreground fields are small compared with \mathcal{E}_Ω (see Sec. III F of Paper I). Although not making significant contribution to the overall value of the diagram, these higher-order contributions are conceptually important, representing 4-momentum transferred to and then recovered from the background fields, analogous to the foreground loops associated with the corrections to the lepton magnetic moment.

There is, however, a critical difference in the value of $\mathbf{f}(\cdot)$ for massive foreground and background fields. For foreground fields, emission and reabsorption of a single particle forms a loop, and integration over this loop yields a factor of $(4\pi)^{-1}$. For background fields, the loop is lost and it is replaced by two randomly oriented interactions with photons from the pseudovacuum. It may be anticipated that some other factor will then replace $(4\pi)^{-1}$. The relative weights of these two distinct scenarios may be evaluated by considering the semiclassical emission and absorption process on \mathbb{C}^{18} from a geometric perspective.

First examining the massive foreground scenario, if the lepton is stationary prior to emitting the loop particle, and the emitted particle has nonzero spatial momentum, there exists a preferred direction from which to recover the loop particle. Barring external interference, preferred absorption is from the same direction that emission was towards. This yields a function in solid angle which approaches a delta function in the classical limit. Similarly, if the particle emitted is stationary in the rest frame of the lepton (this yielding a trajectory in some sense “closest to classical”, about which other trajectories form symmetric perturbations), then change frames such that both are in motion. The preferred direction of emission is along the future trajectory of the lepton, and the preferred direction for absorption is from the past trajectory of the lepton, again yielding a delta function in solid angle.

If, however, the two vertices represent interactions with the background field, then provided the foreground momentum superimposed upon this is sufficiently small, the returning boson at the inbound vertex is equally likely to come from any spatial orientation. The delta function is lost, and integration over solid angle yields a relative factor of 4π .

Finally, if the boson is massless, then regardless of whether it is foreground or background the same argument applies: There is no comoving choice of spatial momentum as the emitting leptons are all massive (even the neutrinos—to be shown in a future paper) and the emitted particle is lightlike. The closest-to-classical trajectory is therefore that in which the loop contracts down to a point. There is no delta function over solid angle.

The corresponding values of $\mathbf{f}(\cdot)$ are thus

$$\mathbf{f}\left(\frac{m_\ell^2}{m_b^2}\right) \rightarrow \begin{cases} 1 & \text{if } m_b^2 = 0 \\ \frac{m_\ell^2}{4\pi m_b^2} & \text{if } m_b^2 \gg m_\ell^2 \text{ and } b \text{ is } [b]_{\text{fg}} \\ \frac{m_\ell^2}{m_b^2} & \text{if } m_b^2 \gg m_\ell^2 \text{ and } b \text{ is } [b]_{\text{bg}}. \end{cases} \quad (\text{A2})$$

It is also worth elaborating on what it means for photon loops to be contracted “down to a point”. In the limit of any loop being sufficiently large, emission and absorption approach being equally likely to be in phase or antiphase, and the long-range contribution of the loop to the vertex correction vanishes. Over distances which are sub-wavelength, however, correlated emission and absorption dominate, yielding a systematic contribution to the loop correction. Recognising that interactions with the background field emulate quantum uncertainty, for a photon with energy below \mathcal{E}_Ω an interaction is functionally pointlike if it takes place over a distance of less than half a wavelength. Within the subset of all such contributions, other process considerations (such as the energy scale of the particles involved) will determine which dominate. If the dominant loop energy is small compared with \mathcal{E}_0 , then a loop contracted down “to a point” still spans a region large compared with the autocorrelation length of the pseudovacuum, \mathcal{L}_0 . This is seen to have relevance for the calculation of some symmetry factors for loop corrections in Ref. [9] and Appendix B.

Appendix B: Symmetry factors and photon loops

When evaluating $\mathcal{O}(\alpha)$ loop diagrams such as those shown in Fig. 17, it can be convenient to have a quick method of evaluating symmetry factors relative to the one-loop electromagnetic correction to the EM vertex of Fig. 32(i). To this end, consider diagram (i) as constituting an electron which, as it propagates, interacts with two correlated photons and one uncorrelated photon. The components of this interaction are shown in diagram (ii). The first interaction is with a correlated photon, with two to choose from. Next there is the interaction being corrected, which is with the uncorrelated photon, and the final interaction is with the photon correlated with the first photon, choice of one, for a relative factor of two.

This may be contrasted with diagram (ii) where the loop photon has been replaced by a W boson. The interactions of the loop correction are now with W and W^\dagger , so each attracts a factor of one, for an overall relative symmetry factor of one.

Next, consider diagram (iii). In this diagram, which corresponds to the third diagram of Fig. 17(i), the electron interacts with two pairs of correlated photons. However, these pairs are distinguishable by the characteristics of their correlations—for the background pair, these correlations vanish over length scales large compared with

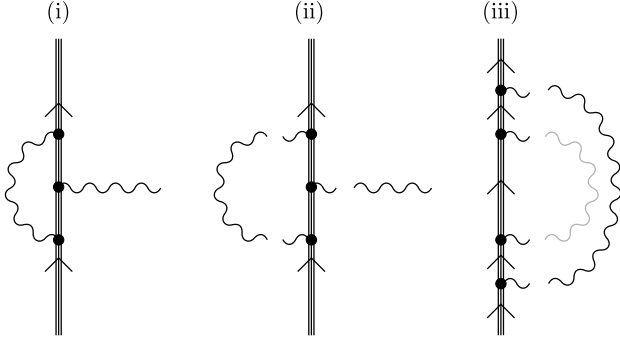


FIG. 32. Evaluation of symmetry factors of $O(\alpha)$ loop corrections. Background (pseudovacuum) photons are shown in grey. (i) The one-loop electromagnetic correction to the EM vertex. (ii) This diagram may be decomposed as a series of interactions between a propagating electron and a set of photons in its vicinity. The arc of the loop may be understood as a correlated photon pair. (iii) A similar decomposition of the third diagram of Fig. 17(iii).

\mathcal{L}_0 , whereas for the foreground pair they do not. The diagram being constructed mandates whether each interaction is with a foreground or background boson, and thus the first interaction is with one of the two correlated foreground photons for a symmetry factor of two. This is then followed by the pair of interactions being corrected, and finally by the interaction with the second boson of the correlated foreground pair. The symmetry factor associated with the loop is thus two, and like Fig. 18, the diagrams of Fig. 17(i) attract loop correction factors of $\alpha/(2\pi)$ apiece.

Although not encountered in this paper, an example will be seen in Ref. [9] in which the loop correction boson of Fig. 32(iii) is also constrained to exhibit rapidly vanishing contributions over length scales large compared with \mathcal{L}_0 . In this context the two correlated pairs of Fig. 32(iii) become indistinguishable and the first interaction attracts a symmetry factor of four as it may be with either constituent of either pair. The next two interactions comprise the process receiving the loop correction, and the final interaction attracts a symmetry factor of one, for a total symmetry factor of four. Such a loop thus attracts a factor of α/π rather than $\alpha/(2\pi)$. As discussed in Appendix A, however, most loop corrections do not exhibit such a constraint, and are dominated by terms which generate the symmetry factor of $\alpha/(2\pi)$ seen in the Standard Model.

It is also worth making an observation regarding the

sign of loop corrections, and the number of fermion lines present. A loop correction to a single photon emission process, such as Fig. 32(i), is positive when the loop incorporates an even number of fermion lines. In contrast, the one-photon loop in the PSE expansion of the electron propagator yields a positive correction when the number of fermion lines is odd. On closing the background photon loop to obtain the parent diagram (prior to mean field expansion), the relationship between diagram (iii) and the PSE is observed. Although diagram (iii) is not part of the fermion PSE of the Standard Model, as there are no pseudovacuum photons in the Standard Model, this diagram is nevertheless seen to be positive with an odd number of fermion lines.

Appendix C: Solving the particle mass relationships

To solve the particle mass relationships of Sec. VI A, proceed as follows:

Take α , m_e , and m_μ as input parameters. To set up the initial value of m_τ , take the uncorrected angle $\theta_\ell = -3\pi/4$, construct the uncorrected K_ℓ matrix as per Eq. (58), and diagonalise to obtain initial values for $k_i^{(e)}$, then write the initial value of m_τ as

$$[m_\tau]_0 = \frac{[k_3^{(e)}]^2}{[k_2^{(e)}]^2} m_\mu^2. \quad (C1)$$

Let the initial value of m_W be arbitrary and large, e.g. 10^4 GeV/ c^2 . Let initial values of m_e , m_H , and m_Z be computed from m_W using tree-level calculations. Determine an initial value for N_0 using Eq. (V:15).

Expand Eq. (137) for $i = 2$ (muon channel, energy scale \mathcal{E}_μ) and substitute m_W^2 for $(m_c^*)^2$ using the expressions for m_W^2/m_c^2 (142) and $[m_c^*(\mathcal{E})]^2$ (129). Rewrite as

$$f_{Wc}^\ell = \frac{1 + \frac{19}{18 [k_1^{(e)}(\mathcal{E}_e) N_0]^4}}{\left\{ 1 + \frac{99}{18 [k_1^{(e)}(\mathcal{E}_e) N_0]^4} \right\} \left(1 - \frac{27m_\ell^2}{10m_c^2} \right)} \quad (C2)$$

$$\tilde{f}_{Wc}^\ell = f_{Wc}^\ell \left\{ 1 + \frac{E1 \alpha}{\pi [k_1^{(e)}(\mathcal{E}_e) N_0]^4} + \frac{E2 \alpha^2}{\pi^2} \right\} \quad (C3)$$

$$\begin{aligned}
0 = & [m_W^4]_{n+1} \left\{ [k_1^{(e)}(\mathcal{E}_\mu)]^4 m_\mu^2 - [k_2^{(e)}(\mathcal{E}_\mu)]^4 m_e^2 \right\} \\
& + [m_W^2]_{n+1} m_e^2 m_\mu^2 \left\{ [k_1^{(e)}(\mathcal{E}_\mu)]^4 - [k_2^{(e)}(\mathcal{E}_\mu)]^4 \right\} \left[\frac{90\alpha + 5}{\pi} + \frac{(5 - 4f_Z)\alpha}{2\pi} + \frac{E9\alpha}{\pi N_0} + \frac{E10\alpha^2 f_{Wc}^\mu}{\pi^2} \right] \\
& + m_e^2 m_\mu^2 \left(\left\{ [k_1^{(e)}(\mathcal{E}_\mu)]^4 m_e^2 - [k_2^{(e)}(\mathcal{E}_\mu)]^4 m_\mu^2 \right\} \left[\frac{450\alpha (\tilde{f}_{Wc}^\mu)^2}{\pi} + \frac{5(25 - 12f_Z)\alpha \tilde{f}_{Wc}^\mu}{6\pi} \right] \right. \\
& \left. + \left\{ [k_1^{(e)}(\mathcal{E}_\mu)]^4 m_e^4 - [k_2^{(e)}(\mathcal{E}_\mu)]^4 m_\mu^4 \right\} \frac{E12 (f_{Wc}^\mu)^4}{[m_c^*(\mathcal{E}_\mu)]^2} \right) + \frac{E14 [m_W^4]_n m_e^2 m_\mu^2 (m_e^2 - m_\mu^2)}{(m_{\mathbf{H}} N_0)^4}, \tag{C4}
\end{aligned}$$

noting that terms in E7, E8, E11, and E13 vanish. It is convenient to leave $(m_c^*)^2$ unexpanded in the E12 term (and using the value of the gluon mass from the previous iteration), such that the equation as a whole is quadratic in m_W^2 . Similarly, more stable iteration is obtained if correction E14 is evaluated using last iteration's value of m_W^2 to yield a numeric term, rather than a coefficient on m_W^4 . Values on convergence are unaffected.

To update m_W^2 , iterate across trial values of θ_e in the

vicinity of $-3\pi/4$. Note that as per Sec. V C 2, the leading correction to θ_e (from the tau channel) makes it less negative so only values $\theta_e > -3\pi/4$ need be considered. For each value of θ_e , compute the associated eigenvalues of the K -matrix at energy scale \mathcal{E}_μ using Eq. (145), then solve Eq. (C4) for an updated value of m_W^2 . Use this to compute associated values of m_c^2 , $m_{\mathbf{H}}^2$, and m_Z^2 using the mass ratios of Eqs. (142–143), and N_0 using Eq. (141) rearranged to solve for N_0^4 ,

$$\begin{aligned}
[N_0^4]_{n+1} = & \frac{m_W^2 \left(1 + \frac{2}{[N_0]_n}\right)^4 \left(1 + \frac{1}{[N_0]_n}\right)^4 \left[1 + \frac{3\alpha}{2\pi} \left(1 + \frac{8}{9[N_0]_n}\right)\right] [1 + \Delta_e(m_e, \mathcal{E}_e)]}{18m_e^2 \left[1 + \left(64 + \frac{3}{2\pi} - f_Z\right) \frac{\alpha}{2\pi}\right] \left(1 + \frac{3\alpha}{2\pi}\right) \left(1 + \frac{19}{18\{k_1^{(e)}(\mathcal{E}_e)[N_0]_n\}^4}\right)} (1 + \mathcal{O}_N) \tag{C5} \\
\mathcal{O}_N := & \frac{E3\alpha}{\pi \{k_1^{(e)}(\mathcal{E}_e)[N_0]_n\}^4} + \frac{E4\alpha^2}{\pi^2} + \frac{E7\alpha}{\pi [N_0]_n^2} + \frac{E8\alpha^2}{\pi^2 [N_0]_n} + \left(\frac{E9\alpha}{\pi [N_0]_n} + \frac{E10\alpha^2}{\pi^2} \right) \frac{m_e^2}{[m_c^*(\mathcal{E}_e)]^2} \\
& + \frac{E11\alpha m_e^2}{\pi m_{\mathbf{H}}^2 \{k_1^{(e)}(\mathcal{E}_e)[N_0]_n\}^4} + \frac{E12 m_e^6}{[m_c^*(\mathcal{E}_e)]^6} + \frac{E13 m_e^2}{m_{\mathbf{H}}^2 [k_1^{(e)}(\mathcal{E}_e)]^4 [N_0]_n^5} + \frac{E14 m_e^4}{m_{\mathbf{H}}^4 \{k_1^{(e)}(\mathcal{E}_e)[N_0]_n\}^4} \tag{C6}
\end{aligned}$$

where $\Delta_e(m_e, \mathcal{E}_e)$ is evaluated from Eq. (128) without error terms as these are all accounted for explicitly in Eq. (C5). Using these updated values, then attempt to recover θ_e by evaluating Eq. (139). If the trial value is denoted θ_e^T and the recovered value is denoted θ_e^R , then each trial value of θ_e is assigned a score based on how well θ_e^R reproduces θ_e^T . Repeat and refine the trial values of θ_e until a best fit is obtained. Update the values of m_c^2 , $m_{\mathbf{H}}^2$, m_Z^2 , and N_0 accordingly.

Since the value of m_W^2 depends on m_c^2 , $m_{\mathbf{H}}^2$, and N_0 , and the values of m_c^2 , $m_{\mathbf{H}}^2$, and N_0 depend on m_W , it is advisable to iterate between updating m_W^2 and updating m_c^2 , $m_{\mathbf{H}}^2$, m_Z^2 , and N_0 until these parameters are satisfactorily converged. In practice, performing one further update to m_W^2 and one further update to m_c^2 , $m_{\mathbf{H}}^2$, m_Z^2 , and N_0 suffices.

Next, expand Eq. (137) for $i = 3$ (tau channel, energy scale \mathcal{E}_τ) and rewrite as

$$\begin{aligned}
0 = & [m_\tau^4]_{n+1} \left\{ \frac{450\alpha}{\pi[m_c^*(\mathcal{E}_\tau)]^4} + \frac{5(25-12f_Z)\alpha}{6\pi[m_c^*(\mathcal{E}_\tau)]^2 m_W^2} + \frac{\text{E14}}{m_{\mathbf{H}}^4 [k_3^{(e)}(\mathcal{E}_\tau) N_0]^4} \right\} \\
& + [m_\tau^2]_{n+1} \left(\frac{90\alpha}{\pi[m_c^*(\mathcal{E}_\tau)]^2} + \frac{(5-4f_Z)\alpha}{2\pi m_W^2} + \frac{5}{[m_c^*(\mathcal{E}_\tau)]^2} + \frac{40}{3m_{\mathbf{H}}^2 [k_3^{(e)}(\mathcal{E}_\tau) N_0]^4} - \frac{[k_1^{(e)}(\mathcal{E}_\tau)]^4 \Delta(m_e, \mathcal{E}_\tau)}{[k_3^{(e)}(\mathcal{E}_\tau)]^4 m_e^2} \right. \\
& \left. + \left(\frac{\text{E9}\alpha}{\pi N_0} + \frac{\text{E10}\alpha^2}{\pi^2} \right) \frac{\left\{ 1 - \left[\frac{k_1^{(e)}(\mathcal{E}_\tau)}{k_3^{(e)}(\mathcal{E}_\tau)} \right]^4 \right\}}{[m_c^*(\mathcal{E}_\tau)]^2} + \frac{\text{E12} \left\{ [m_\tau^4]_n - \left[\frac{k_1^{(e)}(\mathcal{E}_\tau)}{k_3^{(e)}(\mathcal{E}_\tau)} \right]^4 m_e^4 \right\}}{[m_c^*(\mathcal{E}_\tau)]^6} + \frac{\text{E14} m_e^2}{m_{\mathbf{H}}^4 [k_3^{(e)}(\mathcal{E}_\tau) N_0]^4} \right) \\
& + 1,
\end{aligned} \tag{C7}$$

which is a quadratic in $[m_\tau^2]_{n+1}$. Once again, terms in E7, E8, E11, and E13 vanish. Again, iterate over trial values of θ_e , denoted θ_e^T , this time solving for $[m_\tau^2]_{n+1}$ and again computing the recovered value θ_e^R using Eq. (139). Again refine and reiterate until the optimal value of θ_e is identified, this time with all other parameters held constant except m_τ^2 .

Repeatedly alternate between updating m_W^2 (and other boson masses and N_0) and m_τ^2 until convergence.

As a couple of practical notes:

- Close to $\theta_e = -3\pi/4$, $k_1^{(e)}(\theta_e)$ as obtained from Eq. (145) becomes very small and it may be preferable to write

$$[k_1^{(e)}(\theta_e)]^2 \approx \frac{m_e^2}{m_\mu^2} [k_2^{(e)}(\theta_e)]^2, \tag{C8}$$

this approximation being accurate to $\mathcal{O}[\alpha m_{e_i}^2/(m_c^*)^2]$. This approximation should not be employed close to convergence.

- On the first pass for updating m_W^2 , it is convenient to suppress terms in $[k_1^{(e)}(\theta_e) N_0]^4$. These can be incorporated from the second pass, once initial updates to m_W^2 and N_0 have been obtained.
- Negative solutions for m_W^2 or m_τ^2 may be discarded.
- More stable iteration for m_W^2 is obtained if correction E14 is evaluated using last iteration's value of m_W^2 to yield a fixed constant, rather than a coefficient on m_W^4 . Values on convergence are unaffected.
- The algorithm presented here is vulnerable to becoming trapped in pseudominima. These can be recognised by inspecting the value of $\|\theta_e^T - \theta_e^R\|$, which converges to far smaller values at a true minimum (always under 10^{-9} in the reference implementation). Pseudominima may be avoided by changing the sampling density over θ_e .

Octave code implementing the above algorithm may be found accompanying this paper. It has been tested in Octave 6.2.0 with symbolic package v2.9.0 under macOS 11.5.1 and Windows 10, and should also be compatible with MATLAB.

Appendix D: Evaluation of accessory results

Although not yet determined to be directly observable, it is also useful to evaluate the values of the model parameters N_0 , f , ω_0 , \mathcal{E}_0 , and \mathcal{E}_Ω . Allowing the coefficients E1-E18 to range as per Table VII and assuming that all error terms are independent, solving Eq. (C5) yields

$$N_0 = 191.9686(38). \tag{D1}$$

Rearranging Eq. (III:83) gives

$$f^2 = \frac{2\alpha}{N_0^6 S_\alpha (1 + a_e)^2} \tag{154}$$

where

$$S_\alpha := N_0^{-6} (N_0 + \frac{5}{4}) (N_0 + 1)^3 (N_0 + 2)^2. \tag{III:84}$$

Now note the equivalence of a_e in the Standard Model and in the $\mathbb{C}^{\wedge 18}$ model, valid at least up to the mass-independent terms of $\mathcal{O}(\alpha^2/\pi^2)$, and the existence of an uncertainty of $\mathcal{O}(\alpha^2/\pi^2)$ in the calculation of N_0 (C5). The magnitude of this uncertainty justifies the use of either the observed or the Standard Model value of a_e when evaluating Eq. (154)—if there is any error associated with doing so, it is below the threshold of relevance for the calculation. To minimise the number of measured parameters in the software, the reference implementation

takes

$$a_e = \frac{\alpha}{2\pi} + \left\{ \frac{197}{144} + \frac{\pi^2[1 - 6\ln(2)]}{12} + \frac{3\zeta(3)}{4} \right\} \frac{\alpha^2}{\pi^2} + \mathcal{O}\left(\frac{\alpha^2 m_e^2}{m_\mu^2}\right) \quad (\text{D2})$$

$$\approx \frac{\alpha}{2\pi} - 0.328478965579193 \frac{\alpha^2}{\pi^2} + \mathcal{O}\left(\frac{\alpha^2 m_e^2}{m_\mu^2}\right)$$

where the numeric coefficient on α^2/π^2 is as per Refs. [25–27], and the uncertainty term, designated E19, is evaluated as

$$\left| \frac{\text{E19 } \alpha^2 m_e^2}{\pi^2 m_\mu^2} \right| \quad \text{E19} = \pm 10 \quad (\text{D3})$$

in keeping with the approach employed for other unevaluated higher-order terms in the present paper. For a_e this is an extremely conservative approach, with the Standard Model value of E19 being approximately 0.022220 [27]. Directly evaluating the effect of each error term on the computed value of f yields

$$f = 1.669584(99) \times 10^{-8} \quad (\text{155})$$

where independence of sources of uncertainty E1-E19 has been assumed.

The value of ω_0 is given by rearranging Eq. (127) and substituting Eq. (154),

$$\omega_0 = \left\{ \frac{m_e^2 S_\alpha (1 + a_e)^2}{\alpha [k_1^{(e)}(\mathcal{E}_e)]^4 N_0^2 S_{18,147} C_{\alpha, N_0} [1 + \Delta_e(m_e, \mathcal{E}_e)]} \right\}^{\frac{1}{2}} \times [1 + \frac{1}{4}\mathcal{O}_N + \frac{1}{2}\mathcal{O}_e(m_e, \mathcal{E}_e)] \quad (\text{D4})$$

$$S_{18,147} := N_0^{-12} (N_0 + 2)^6 (N_0 + 1)^6 \quad (\text{D5})$$

$$C_{\alpha, N_0} := \frac{1 + \frac{3\alpha}{2\pi} \left(1 + \frac{8}{9N_0}\right)}{1 + \frac{3\alpha}{2\pi}}, \quad (\text{80})$$

where the definition of $S_{18,147}$ agrees with Eq. (IV:32), while

$$\mathcal{E}_0 := N_0 \omega_0 (1 - \frac{1}{4}\mathcal{O}_N) \quad (\text{D6})$$

$$\mathcal{E}_\Omega := \mathbf{n} N_0 (N_0 - \frac{1}{2}) \omega_0 \quad | \quad \mathbf{n} = 9 \quad (\text{V:23})$$

where the coefficients on \mathcal{O}_e and \mathcal{O}_N reflect rescalings of the range of the error coefficients E1-E18 relative to their original appearances in Eqs. (137–148). Once again allow the coefficients E1-E18 to range as per Table VII prior to this rescaling, and E19 as per Eq. (D3). The errors associated with each of E1-E19 are again evaluated directly, then combined under the assumption of independence.

Note that the terms in \mathcal{O}_N disappear on \mathcal{E}_0 . However, \mathcal{O}_e contains corrections of $\mathcal{O}[\alpha/(\pi N_0)]$ which are large enough to permit the use of Eq. (D2) for a_e in Eq. (D4) without discernible error.

On evaluation these equations yield

$$\omega_0 = 18.68278(36) \text{ MeV} \quad (\text{D7})$$

$$\mathcal{E}_0 = 3.5865081(18) \text{ GeV} \quad (\text{D8})$$

$$\mathcal{E}_\Omega = 6.18033(13) \text{ TeV}. \quad (\text{D9})$$

-
- [1] R. N. C. Pfeifer, I. Normalisable quasiparticles on a manifold with anticommuting co-ordinates (2021), draft available at <https://www.academia.edu/65931513>.
- [2] R. N. C. Pfeifer, II. Colour interactions and fermions from scalar fields on $\mathbb{C}^{\wedge 6}$ (2021), draft available at <https://www.academia.edu/65931513>.
- [3] R. N. C. Pfeifer, III. Standard Model particle spectrum from scalar fields on $\mathbb{C}^{\wedge 18}$ (2021), draft available at <https://www.academia.edu/65931513>.
- [4] R. N. C. Pfeifer, IV. Calculation of fermion masses on $\mathbb{C}^{\wedge 18}$ (2021), draft available at <https://www.academia.edu/65931513>.
- [5] R. N. C. Pfeifer, V. Calculation of boson masses on $\mathbb{C}^{\wedge 18}$ (2021), draft available at <https://www.academia.edu/65931513>.
- [6] J. D. Maynard, Acoustical analogs of condensed-matter problems, *Rev. Mod. Phys.* **73**, 401 (2001).
- [7] D. Dragoman and M. Dragoman, *Quantum-Classical Analogies*, The Frontiers Collection (Springer-Verlag, Berlin Heidelberg, 2004).
- [8] M. Lewenstein, A. Sanpera, V. Ahufinger, B. Damski,

- A. Sen(De), and U. Sen, Ultracold atomic gases in optical lattices: mimicking condensed matter physics and beyond, *Adv. Phys.* **56**, 243 (2007).
- [9] R. N. C. Pfeifer, VII. Curved spacetimes from $\mathbb{C}^{\wedge 18}$ (2021), draft available at <https://www.academia.edu/65931513>.
- [10] This averaging takes place with respect to the preons of Fig. 5(iv), which are a numerical convenience—it has no bearing on the sum over the six different loop positions available in Fig. 1(ii) or the three different pseudovacuum expansions apiece, and the calculation thus far is still only for a single one of these six diagrams and three expansions.
- [11] M. E. Peskin and D. V. Schroeder, *An Introduction to Quantum Field Theory* (Westview Press, 1995).
- [12] A. Kitaev, Anyons in an exactly solved model and beyond, *Ann. Phys.* **321**, 2 (2006).
- [13] P. H. Bonderson, *Non-Abelian Anyons and Interferometry*, *Ph.D. thesis*, California Institute of Technology (2007).
- [14] It is interesting that in the $\mathbb{C}^{\wedge 18}$ model, all on-shell so-

- lutions apply to the same underlying preon fields. Thus there exists one set of fields with multiple on-shell solutions, rather than multiple fields with one mass shell apiece. For simplicity all mass shells are treated as independent, which introduces negligible error for sufficiently distinct masses, but is quite readily apparent when different rearrangements of the same preons must be treated as loops constructed on independent foreground fields, as seen here.
- [15] Y. Koide, Quark and lepton mass matrices with a cyclic permutation invariant form, in *Proc. 30th Int. Conf. High-energy Phys., Osaka, Japan*, edited by C. S. Lim and T. Yamanaka (World Scientific, Singapore, 2001) [arXiv:hep-ph/0005137v1](https://arxiv.org/abs/hep-ph/0005137v1).
 - [16] R. Penrose, Applications of negative dimensional tensors, in *Combinatorial Mathematics and its Applications*, edited by D. J. A. Welsh (Academic Press, 1971) pp. 221–244.
 - [17] R. N. C. Pfeifer, P. Corboz, O. Buerschaper, M. Aguado, M. Troyer, and G. Vidal, Simulation of anyons with tensor network algorithms, *Phys. Rev. B* **82**, 115126 (2010).
 - [18] R. N. C. Pfeifer, *Simulation of Anyons Using Symmetric Tensor Network Algorithms*, Ph.D. thesis, The University of Queensland (2011), [arXiv:1202.1522v2](https://arxiv.org/abs/1202.1522v2).
 - [19] Note that if one diagram family as per Fig. 15 can be made to have no net effect on colour, then all paired background bosons have no net effect on colour. Further, as unpaired bosons (as well as being exceedingly rare) have on average no net effect on colour, these may also be grouped into clusters having zero net colour effect overall, and an analogous co-ordinate transformation performed such that their effect on colour vanishes instant-by-instant as well as on average, with the associated bosons vanishing over distances large compared with \mathcal{L}_0 . Thus no error is made in requiring that colour is left unchanged on a per-diagram basis. Also note that once the mechanism for corrections to θ_e is fully elucidated, the co-ordinate transformations arising from the unpaired bosons yield no systematic effect on θ_e and thus their effect may be ignored over macroscopic scales.
 - [20] P. A. Zyla *et al.*, Review of particle physics, *Prog. Theor. Exp. Phys.* **2020**, 083C01 (2020), and 2021 update, <http://pdg.lbl.gov/>.
 - [21] E. Tiesinga, P. J. Mohr, D. B. Newell, and B. N. Taylor, The 2018 CODATA Recommended Values of the Fundamental Physical Constants (2018), (Web Version 8.1). Database developed by J. Baker, M. Douma, and S. Kotochigova. Available at <http://physics.nist.gov/constants>, National Institute of Standards and Technology, Gaithersburg, MD 20899.
 - [22] R. N. C. Pfeifer, VI. Particle generations and masses on \mathbb{C}^{18} (2021), draft available at <https://www.academia.edu/65931513>.
 - [23] R. P. Kerr, Gravitational field of a spinning mass as an example of algebraically special metrics, *Phys. Rev. Lett.* **11**, 237 (1963).
 - [24] D. Di Mario, <http://digilander.libero.it/bubblegate/ephys.html>, *The Physics Deep*, retrieved 31st October 2007, hosting articles *Magnetic Anomaly in Black Hole Electrons* (2003), *Planck Permittivity and Electron Force* (2003), *Reality of the Planck Mass* (2003), *Electric Field as Variation of Gravity* (2005).
 - [25] A. Petermann, Fourth order magnetic moment of the electron, *Nuclear Physics* **5**, 677 (1958).
 - [26] C. M. Sommerfield, The magnetic moment of the electron, *Annals of Physics* **5**, 26 (1958).
 - [27] T. Aoyama, T. Kinoshita, and M. Nio, Theory of the anomalous magnetic moment of the electron, *Atoms* **7**, 28 (2019).

The relationships determined to date between particle masses in the $\mathbb{C}^{\wedge 18}$ model, and the expression for Newton's Constant, are:

$$\begin{aligned}
\frac{m_{e_i}^2}{m_e^2} &= \frac{\left[k_1^{(e)}(\mathcal{E}_{e_i}) \right]^4 [1 + \Delta_e(m_{e_i}, \mathcal{E}_{e_i})]}{\left[k_1^{(e)}(\mathcal{E}_{e_i}) \right]^4 [1 + \Delta_e(m_e, \mathcal{E}_{e_i})]} \left[1 + \mathcal{O}_e(m_{e_i}, \mathcal{E}_{e_i}) \right] \quad \left| \quad e_i \in \{e, \mu, \tau\} \right. \\
\frac{m_W^2}{m_e^2} &= 18N_0^4 \left(1 + \frac{2}{N_0} \right)^4 \left(1 + \frac{1}{N_0} \right)^4 \frac{\left[1 + \left(64 + \frac{3}{2\pi} - fz \right) \frac{\alpha}{2\pi} \right] \left\{ 1 + \frac{19}{18[k_1^{(e)}(\mathcal{E}_e) N_0]^4} \right\} \left(1 + \frac{3\alpha}{2\pi} \right)}{\left[1 + \Delta_e(m_e, \mathcal{E}_e) \right] \left[1 + \frac{3\alpha}{2\pi} \left(1 + \frac{8}{9N_0} \right) \right]} [1 + \mathcal{O}_b + \mathcal{O}_e(m_e, \mathcal{E}_e)] \\
\frac{m_W^2}{m_Z^2} &= \frac{3 \left[1 + \left(64 + \frac{3}{2\pi} - fz \right) \frac{\alpha}{2\pi} \right] \left\{ 1 + \frac{19}{18[k_1^{(e)}(\mathcal{E}_e) N_0]^4} \right\}}{4 \left[1 + \left(\frac{401}{12} + \frac{3}{2\pi} \right) \frac{\alpha}{2\pi} \right] \left\{ 1 + \frac{23}{18[k_1^{(e)}(\mathcal{E}_e) N_0]^4} \right\}} (1 + \mathcal{O}_b) \quad \frac{m_W^2}{m_e^2} = \frac{1 + \frac{19}{18[k_1^{(e)}(\mathcal{E}_e) N_0]^4}}{1 + \frac{99}{18[k_1^{(e)}(\mathcal{E}_e) N_0]^4}} (1 + \mathcal{O}_b) \\
\frac{m_W^2}{m_H^2} &= \frac{9 \left[1 + \left(64 + \frac{3}{2\pi} - fz \right) \frac{\alpha}{2\pi} \right] \left\{ 1 + \frac{19}{18[k_1^{(e)}(\mathcal{E}_e) N_0]^4} \right\}}{20 \left\{ \left(1 - \frac{1}{9N_0} \right)^2 \left[1 + \frac{30\alpha}{9\pi} \left(1 + \frac{1}{9N_0} \right) \right] + \frac{1}{2\pi} \left[1 + \frac{30\alpha}{\pi} \left(1 - \frac{1}{9N_0} \right) \right] \right\} \left\{ 1 + \frac{7}{18[k_1^{(e)}(\mathcal{E}_e) N_0]^4} \right\}} (1 + \mathcal{O}_b) \\
\Delta_e(m_{e_i}, \mathcal{E}) &= \frac{90\alpha m_{e_i}^2}{\pi [m_c^*(\mathcal{E})]^2} + \frac{(5 - 4fz)\alpha m_{e_i}^2}{2\pi m_W^2} + \frac{5m_{e_i}^2}{[m_c^*(\mathcal{E})]^2} \left[1 + \frac{90\alpha m_{e_i}^2}{\pi [m_c^*(\mathcal{E})]^2} + \frac{(25 - 12fz)\alpha m_{e_i}^2}{6\pi m_W^2} \right] + \frac{40m_{e_i}^2}{3m_H^2 [k_i^{(e)}(\mathcal{E}) N_0]^4} \\
&\quad + \mathcal{O}_e(m_{e_i}, \mathcal{E}_{e_i}) \\
\theta_e(\mathcal{E}) &= -\frac{3\pi}{4} \left(1 - \frac{4\sqrt{\delta_e \{ r[\Delta_e(m_\tau, \mathcal{E}) - \Delta_e(m_\mu, \mathcal{E})] \}}}{3\pi} \right) \left(1 + \frac{4\sqrt{\delta_e \{ r[\Delta_e(m_e, \mathcal{E})] \}}}{3\pi} \right) \quad r(n) = n \cdot \sqrt{1 - \frac{n}{9}} \\
fz &= \frac{1}{3} \left(4 - 24 \frac{m_W^2}{m_Z^2} + 16 \frac{m_W^4}{m_Z^4} \right) \quad \delta_e(n) = \sqrt{1 + \frac{\pi^2 n}{8} \left[1 + \frac{\pi^2 n}{32} \right]} - 1 + \mathcal{O}(n^3) \\
[m_c^*(\mathcal{E})]^2 &= m_c^2 \left(1 - \frac{27}{10} \frac{\mathcal{E}^2}{m_c^2 c^4} \right) \quad k_n^{(\ell)}(\mathcal{E}) = 1 + \sqrt{2} \cos \left[\theta_\ell(\mathcal{E}) - \frac{2\pi(n-1)}{3} \right] \quad \mathcal{E}_\ell = m_\ell c^2 \\
G_N &= \frac{2\alpha^4 h c [1 + \Delta_e(m_e, \mathcal{E}_e)]^{\frac{1}{2}} \left(1 + \frac{3\alpha}{2\pi} + \frac{4\alpha}{3\pi N_0} \right)^{\frac{1}{2}} \left(1 + \frac{7\alpha}{2\pi} + \frac{16\alpha}{3\pi N_0} \right)}{\pi [k_1^{(e)}(\mathcal{E})]^4 m_e^2 \left(1 + \frac{\alpha}{2\pi} + \left\{ \frac{197}{144} + \frac{\pi^2 [1-6\ln(2)]}{12} + \frac{3\zeta(3)}{4} \frac{\alpha^2}{\pi^2} \right\}^8 \left(1 + \frac{3\alpha}{2\pi} \right)^{\frac{1}{2}} \right)} \left[1 + \mathcal{O}_b + \mathcal{O}_e(m_e, \mathcal{E}_e) + \mathcal{O} \left(\frac{\alpha^2 m_e^2}{\pi^2 m_\mu^2} \right) \right] \\
&\quad \times \frac{N_0^6}{\{ 2[(N_0 + 4)(N_0 + 3)]^4 + [8(N_0 + 3)^4 + 6(N_0 + 2)^4](N_0 + 1)^4 \} [(N_0 + 2)(N_0 + 1)^2]^4 (N_0 + \frac{5}{4})^3 (N_0 + 2)} \\
\mathcal{O}_e(m_{e_i}, \mathcal{E}) &= \mathcal{O} \left(\frac{\alpha}{\pi N_0^2} \right) + \mathcal{O} \left(\frac{\alpha^2}{\pi^2 N_0} \right) + \mathcal{O} \left[\frac{\alpha m_{e_i}^2}{\pi N_0 [m_c^*(\mathcal{E})]^2} \right] + \mathcal{O} \left\{ \frac{\alpha^2 m_{e_i}^2}{\pi^2 [m_c^*(\mathcal{E})]^2} \right\} + \mathcal{O} \left\{ \frac{\alpha m_{e_i}^2}{\pi m_H^2 [k_i^{(e)}(\mathcal{E}) N_0]^4} \right\} + \mathcal{O} \left\{ \frac{m_{e_i}^6}{[m_c^*(\mathcal{E})]^6} \right\} \\
&\quad + \mathcal{O} \left\{ \frac{m_{e_i}^2}{m_H^2 [k_i^{(e)}(\mathcal{E})]^4 N_0^5} \right\} + \mathcal{O} \left\{ \frac{m_{e_i}^4}{m_H^4 [k_i^{(e)}(\mathcal{E}) N_0]^4} \right\} \quad \mathcal{O}_b = \mathcal{O} \left\{ \frac{\alpha}{\pi} [k_1^{(e)}(\mathcal{E}_e) N_0]^{-4} \right\} + \mathcal{O} \left(\frac{\alpha^2}{\pi^2} \right).
\end{aligned}$$

Taking $\alpha = 7.2973525693(11) \times 10^{-3}$, $m_e = 0.5109989461(31) \text{ MeV}/c^2$, and $m_\mu = 105.6583745(24) \text{ MeV}/c^2$, these relationships may be solved to yield:

Parameter	Calculated value	Observed value	Discrepancy (experimental σ)
$m_\tau \text{ (MeV}/c^2)$	1776.8715(2) ^a	1776.86(12)	0.1
$m_W \text{ (GeV}/c^2)$	80.3784(24)	80.379(12)	0.05
$m_Z \text{ (GeV}/c^2)$	91.1875(37)	91.1876(21)	0.04
$m_H \text{ (GeV}/c^2)$	125.2498(51)	125.25(17)	0.001
$G_N \text{ (} 10^{-11} \text{ m}^3 \text{kg}^{-1} \text{s}^{-2})$	6.67427(240)	6.67430(15)	0.18

^a Limited by precision of numerical solver